Dynamic Wetting, Self-assembly, and Coalescence of Droplets in Microchannels.

A Dissertation
by
Bibin Mathew Jose

to
The Graduate School
in Partial Fulfillment of the Requirements
for the Degree of
Doctor of Philosophy
in
Mechanical Engineering
Stony Brook University

May 2015

Stony Brook University
Department of Mechanical Engineering

Bibin Mathew Jose

We, the dissertation committee for the above candidate for the
Doctor of Philosophy degree, hereby recommend
acceptance of this dissertation.

Thomas Cubaud
Dissertation Advisor
Mechanical Engineering

Carlos Colosqui
Committee Chair
Mechanical Engineering

Harold Walker
Committee Member
Mechanical & Civil Engineering

David Hwang
Committee Member
Mechanical Engineering

Molly Gentleman
Outside Member
Materials Science & Engineering

This dissertation is accepted by the Graduate School

Charles Taber

Dean of the Graduate School

Abstract of the Dissertation

Dynamic Wetting, Self-assembly, and Coalescence of Droplets in Microchannels.

by

Bibin Mathew Jose

Doctor of Philosophy

in

Mechanical Engineering

Stony Brook University

2015

In this thesis, we experimentally examine the evolution of partially wetting droplets in square microchannels, and the dynamic self-assembly and coalescence of droplets in a slit microchamber. In confined small-scale flows, variations and irregularities of the flow geometry introduce high degree of complexities for predicting and modeling the droplet interactions with each other and with walls during the multiphase transport. Construction of robust microgeometries along with precise control of the fluid interfaces using microfluidic techniques are used in conjunction with high-speed imaging to study the temporal evolution of two-phase flows. Immiscible two-phase flows mainly show two types of interactions: (1) the liquid-liquid interface can interact with the solid walls and (2) the liquid-liquid interfaces can interact with each other. A variety of wetting transitions are observed when the liquid-liquid interfaces are confined by the solid walls. Some of the dynamic wetting transitions in two-phase immiscible flows include dewetting of the lubricating film, stick-slip motion of contact line and the possibility of the dewetting line to align with the flow direction. We show that natural wetting properties of the fluid pair can be a useful parameter to classify the dynamic wetting transitions as well as the interfacial morphologies in microchannels. The relevant parameters to control the dynamic wetting transitions of the two-phase flow are presented with phase diagrams. To study the interactions of liquid-liquid interfaces, we examine the dynamic self-assembly of droplets in a diverging/converging slit microchamber. Focusing on the limit of dilute emulsions, formation and stability of self-assembled structures of droplets in the microchamber is investigated. We demonstrate that hydrodynamic coupling and coalescence of droplets in a simple extensional geometry can be controlled by adjusting the injection capillary number as well as the aspect ratio of the incoming droplet train.

To my parents and my sister.

Contents

List of Tables

List of Tables

Acknowledgments

During the past five years in Stony Brook, I had the opportunity to meet and work with many interesting human beings. First and foremost, I express my sincere gratitude to my advisor, Professor Thomas Cubaud for his support, encouragement, and guidance during the course of my PhD program. Furthermore, I thank Stony Brook University for providing me this opportunity. This work is supported by the grants from national science foundation and I acknowledge their continuing financial support for our research. I also acknowledge the members of my dissertation committee for their suggestions and the careful reading of manuscript.

My family has been the biggest source of emotional comfort and I thank my parents and my sister for their love and kindness. Again, I want to thank my friends Vishnu and Mark for their company. Lastly, but not the least, I thank Riya for the interesting conversations.

The author hereby certifies that the use of any copyrighted material in the manuscript beyond brief excerpts is with the permission of the copyright owner, and will save and hold harmless University Microfilms from any damage that may arise from such copyright violations.

1. Introduction

1.1. Microfluidics

Microfluidics is a technology used to process and handle small volumes of fluids by manipulating flow at micrometric scale [1]. Microfluidic technology offers the potential to miniaturize and optimize complex laboratory procedures as well as the development of low cost practical devices [2]. The advantages include the ability to work with smaller reagent volumes, shorter reaction times, and the possibility of parallel operation [3]. Microfluidics also promises enormous potential for the advancement of chemical or biological research [4, 5]. Some of the applications of microfluidics in biotechnology include the development of point-of-care diagnostic devices, genomics, sequencing and high-throughput screening [6]. Although microfluidics is used to design and conduct complex biological and chemical experiments, the lack of high levels of integration remains a major challenge [7-9]. Some of the bold attempts of integration include using a microfluidic network with valves and chambers to mimic the functionalities of an integrated chip [10] and the use of a microchemostat for the long term monitoring of bacteria [11]. Nevertheless, microfluidic platforms can be used to test the well-established theories in fluid mechanics and also to uncover new phenomena at microscopic level [12, 13].

1.2. Droplets in microfluidics

In microfluidic platforms, droplets are a convenient way to transport liquids and particles in a controlled manner [14]. The main advantage of droplet microfluidics is the ability to generate monodisperse droplets with very high degree of precision. Monodispersity of the microfluidic droplets can be exploited to synthesize materials with tailored structural properties with narrow size distribution [15-18]. Typically, droplet volumes vary from 10^{-10} to 10^{-5} L with very low consumption of reagents [19]. In droplet microfluidics, droplets used to compartmentalize chemical reactions and apply to a large number of experiments where each droplet contains the reagents necessary for the particular reaction [20]. Such techniques are extended to encapsulate cells or living organisms where the local environment inside droplet can be modified and controlled efficiently [21, 22]. Indeed, droplets can also be used to mix two components. At small scale, mixing across laminar streams happen purely by diffusion [23] and chaotic advection inside droplets can be effectively employed to reduce mixing times [24]. Often fusion of droplets is also used for precise mixing of the components [25-28]. Recently, Zeng *et al*. [29] have demonstrated that small volume of droplets can be effectively used for screening hundreds of protein crystallization conditions. One of the most promising applications of droplet microfluidics is the RainDrop™ Digital PCR System by Raindance Technologies [30].

In typical droplets microfluidic platforms, residence times vary between seconds to minutes that might not be suitable for many lengthy experiments such as incubation of cells and in vitro expression of proteins [31-33]. For increased residence time, methods have been developed for the passive storage of droplets in a continuous stream [34, 35]. Droplet sorting is also widely employed in microfluidic devices to separate droplets encapsulated with ‘species of interest’ from the rest [31, 36-38]. Some of the detection and sorting techniques integrated into the microfluidic chips include the use of surface acoustic waves [39], temperature control [40, 41], and electric field [42]. There have been a multitude of applications that utilize the high surface to volume ratios of two-phase flow to enhance heat and mass transfer across liquid interfaces [43, 44]. Since droplet based microfluidics relies mainly on the control of fluid interfaces, stability of fluid interfaces and their interactions with solid walls are of great importance. Usually this is achieved by the addition of surfactants which facilitate the stability of interfaces by lowering interfacial tension [45].

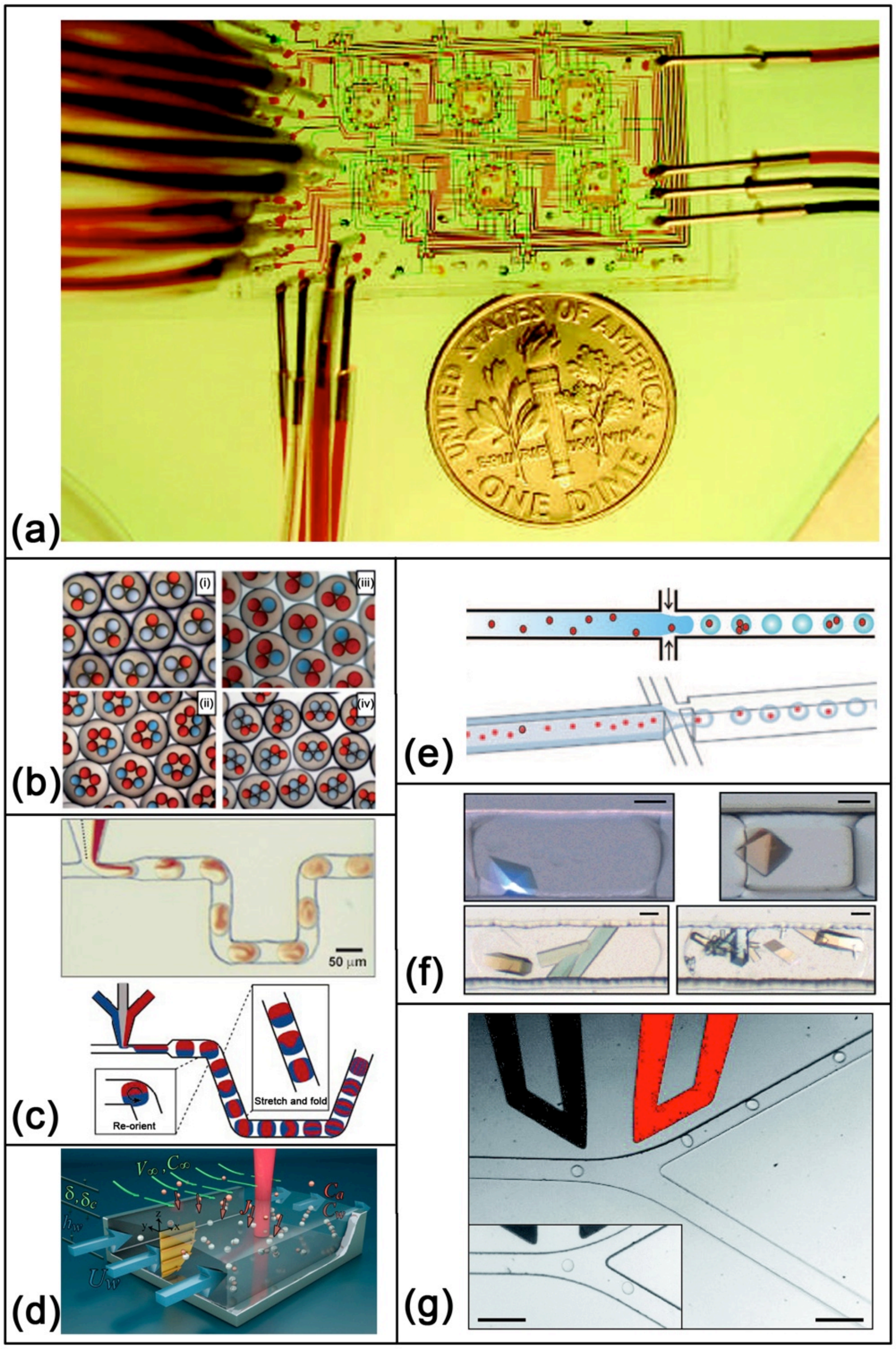

Figure 1.1 (a) Microfluidic device: A microfluidic chemostat to study the growth of microbial populations [11]. (b) Formation of double emulsion with four different types of inner drops [16]. (c) Chaotic advection of droplets moving through a microchannel [24]. (d) Free surface microfluidic chip for real time trace vapor detection [46] (e) Encapsulation of particles into droplets [21]. (f) Protein crystals obtained inside droplets on a microfluidic chip [29]. (g) Sorting droplets using electric field [42].

1.3. Modeling porous media using microfluidics

Understanding immiscible flow through highly opaque porous media is a challenging problem due to the lack of direct visualization of the fluid flow [47]. A major advantage of microfluidic micro-models include the possibility to directly examine flow through fluidic networks [48]. Several studies have employed microfluidic chips to study different physical models of porous media for energy applications [49], carbon sequestration in saline aquifers [50], and conventional oil recovery[51]. Typical porous medium consists of a complex solid matrix composed of a random network of interconnected pores through which fluid can flow [52]. A modeling strategy consists of approximating the pore geometry within two parallel plates and examining Hele-Shaw flows [53]. The connecting throats between the pores can be modeled with polygonal capillaries while the pores can be modeled using a two-dimensional slit-type microchannel. In such microfluidic models, drainage [54] and imbibition [55] process during fluid displacement in porous media, can be examined in detail and correlations can be made between fluid flow and wetting properties [56].

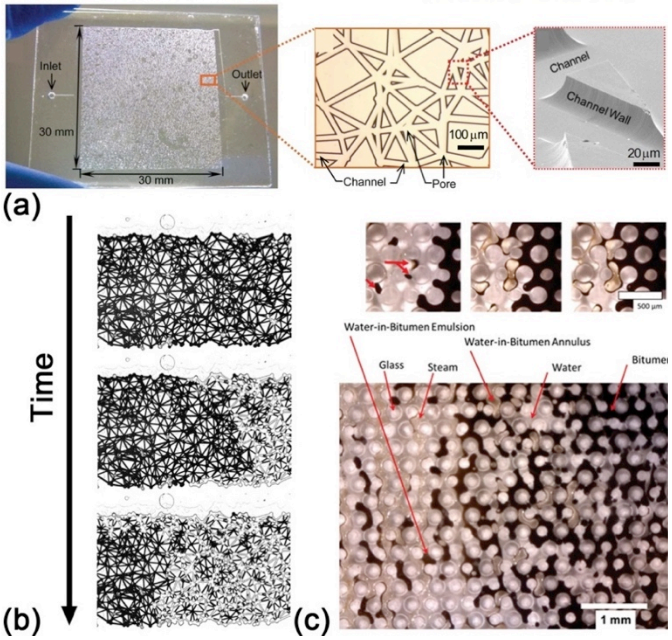

Figure 1.2 (a) Photograph of microfluidic chip showing the microfluidic network on a glass chip mimicking the properties of the native porous media [50]. (b) Images obtained during the drainage of wetting phase (shown in dark color) from a non-wetting phase (light color) in a microfluidic chip [51]. (c) Steam assisted gravity drainage on a chip. Red arrow indicates flow of water into bitumen phase [48].

1.4. Microfluidics and fluid mechanics

Microscale multiphase flows in basic plane and compact geometries have recently been examined using microfluidic devices [57-65] especially for droplet flows [66]. From the perspective of fluid dynamics, the most important characteristic of microfluidics is the laminar flow given by low Reynolds number. The Reynolds number *Re* for a flow is given by the ratio of inertial to viscous forces. With low Reynolds number *Re*, fluid transport in micron-sized channels is dominated by viscous dissipation and the effects of inertia are weak [67]. Given the significance of viscous forces, precise handling of highly viscous fluids can be even more challenging. Another aspect of micro flows is the significance of surface phenomena such as wetting due to the prominence of surface forces at micro scale [68]. Applications have been developed to exploit this large surface to volume ratio for the detection of airborne molecules [46]. In short, control of the fluid flow at micro scale opens new avenues and requires a detailed understanding of the interaction between surface forces.

1.5. Wetting: statics and dynamics

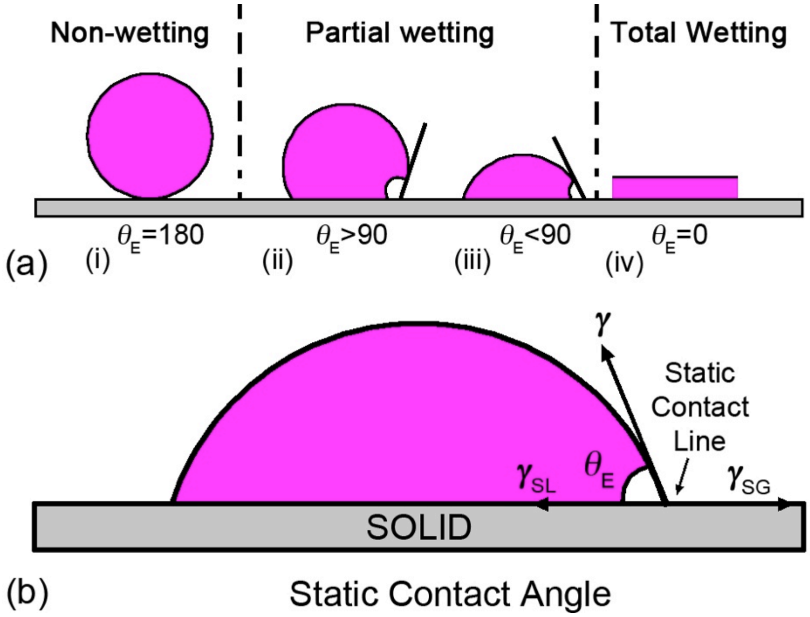

Figure 1.3 Static configurations of a liquid on a solid substrate (a) (*i*) non-wetting (*ii*) partially non-wetting (*iii*) partially wetting and (*iv*) totally wetting. (b) Balance of forces for a partially wetting droplet at the contact line.

Wetting properties of solids are essentially determined by the static contact angle θ_E made by the fluid interface at equilibrium [69-71]. A liquid droplet deposited on a flat solid surface shows three different equilibrium regimes as (*i*) non-wetting, (*ii*-*iii*) partial wetting, and (*iv*) total wetting. In the non-wetting regime ($\theta_E = \pi$), the deposited droplet is spherical with negligible contact area [Figure 1.3(a)*i*]. For total wetting ($\theta_E = 0$), the liquid completely spreads on the surface leading to the formation of a thin film [Figure 1.3(a)*iv*]. In contrast, the liquid does not fully spread in the partial wetting regime resulting in a contact line. Two configurations can be found in the partial wetting regime namely "partially non-wetting or hydrophobic" ($\theta_E > \pi/2$) and "partially wetting or hydrophilic" ($\theta_E < \pi/2$). Balancing the forces in equilibrium on a rigid solid surface at the contact line gives the static contact angle θ_E [Figure 1.3(b)]. The relation describing the static contact angle is commonly known as Young's relation [72].

$$\gamma \cos \theta_E = \gamma_{SG} - \gamma_{SL} \qquad (1.1)$$

where γ is the is the interfacial tension between the liquid and gas, γ_{SG} is the interfacial tension between solid and gas and γ_{SL} is the interfacial tension between solid and liquid.

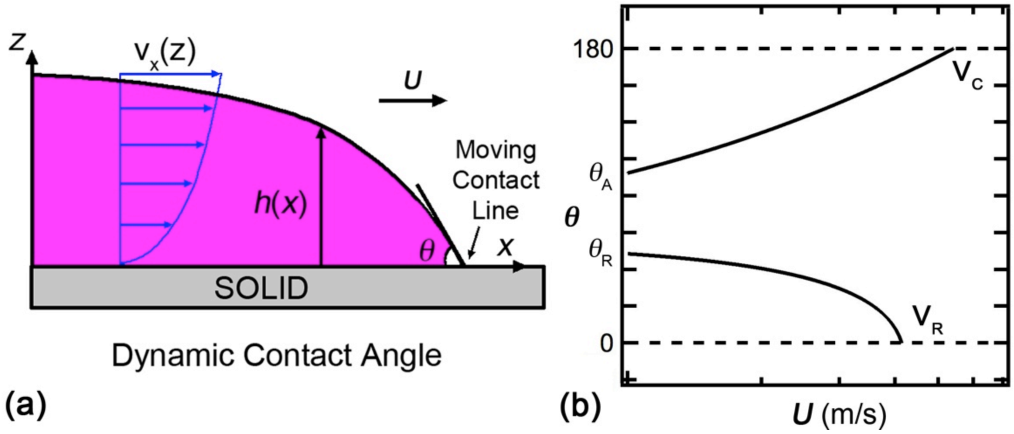

Figure 1.4 Dynamic contact angle: (a) Schematic of liquid wedge advancing on a solid with a moving contact line. (b) Schematic representation of the velocity dependence on contact angle θ showing advancing θ_A and receding limits θ_R.

For a moving contact line, the dynamic contact angle θ is different from the static contact angle θ_E [Figure 1.3(c)] [73]. To develop an expression for the dynamic contact angle θ as a function of velocity, Cox and Voinov considered the two-dimensional motion of a liquid wedge advancing on a solid [Figure 1.4(a)] where the profile of liquid wedge is given by [74, 75],

$$h = h(x). \qquad (1.2)$$

For low Reynolds number *Re*, spreading of a viscous fluid forms a dynamic angle θ at the solid boundary. Making use of lubrication approximation, the liquid wedge can be treated as a nearly flat film, with a quadratic velocity profile is given by [70]

$$\mathbf{v} = v_x(z) = \frac{3U}{2h^2} z\left(2h - z\right) \qquad (1.3)$$

where U is average velocity in the wedge $U = \frac{1}{h}\int_0^h v_x(z)\,\mathrm{d}z$.

Since $Re \ll 1$, the convective terms in the Navier Stokes equation can be neglected and the fluid motion is described by Stokes equation [74, 75]

$$\nabla p = \eta \nabla^2 \mathbf{v}\,, \quad \nabla.\mathbf{v} = 0 \qquad (1.4)$$

where p is the pressure and $\mathbf{v}$ is velocity. Again, for length scales smaller than capillary length scale, gravity effects can be neglected and the pressure is expressed in terms of curvature κ according to Young-Laplace law [76, 77],

$$p = \gamma\kappa = -\gamma \frac{\partial^2 h}{\partial x^2}\,. \qquad (1.5)$$

In the hydrodynamic model, viscous contribution is calculated by considering only the viscous dissipation of the contact line and is given by [77],

$$\eta \nabla^2 \mathbf{v} = \eta \frac{\partial^2 v_x(z)}{\partial z^2} = -3\frac{\eta U}{h^2} . \tag{1.6}$$

Substituting (1.5) and (1.6) into (1.4) [77]

$$\frac{\partial^3 h}{\partial x^3} = 3\frac{\eta U}{\gamma h^2} \tag{1.7}$$

After integration, an expression for the dynamic contact angle is given by [74, 75, 78]

$$\theta^3 = \theta_\mathrm{E}^3 + 9\frac{\eta U}{\gamma}\ln\left(\frac{h}{h_m}\right) \quad \text{for} \quad \theta < \frac{3\pi}{4} . \tag{1.8}$$

If the cut-off scale h_m goes to zero, the term $\ln(h/h_\mathrm{m})$ would diverge [79]. This singularity at the contact line is removed by defining a microscopic cut-off length h_m above which it is possible to use the hydrodynamic description of the fluid. A detailed analysis of the integration of equation (1.7) is given by Cox and Voinov [74, 75]. Finally, an expression for the dynamic contact angle θ is obtained as a function of contact line velocity U [80]. In Eqn. (1.8), U is chosen as the absolute value of the velocity and the sign changes for the receding branch of the equation [81].

Most real surfaces are hysteretic and the static contact angle can adopt any intermediate value θ_E between the advancing and the receding limits given by $\theta_\mathrm{A} \geq \theta_\mathrm{E} \geq \theta_\mathrm{R}$ [82, 83]. When the wetting line is made to advance, θ becomes greater than θ_A, and when the contact line is made to recede θ becomes less than θ_R [84, 85]. The contact angle hysteresis is usually attributed to surface heterogeneities causing the system to adopt different metastable configurations [86]. Now, consider two immiscible liquids $L1$ and $L2$ in contact with a solid surface, where $L1$ is displacing $L2$. The immiscible displacement of two liquids is described by advancing of $L1$ and receding of $L2$. Although the validity of the Eqn. (1.8) is limited to $\theta < 3\pi/4$, the relationship of contact angle and contact line speed still holds for the entire range of $0 \sim \pi$ upon interchanging the role of liquids, *i.e.* $U = -U$ and $\theta = (\pi - \theta)$ [74].

1.6. Dynamic wetting transitions

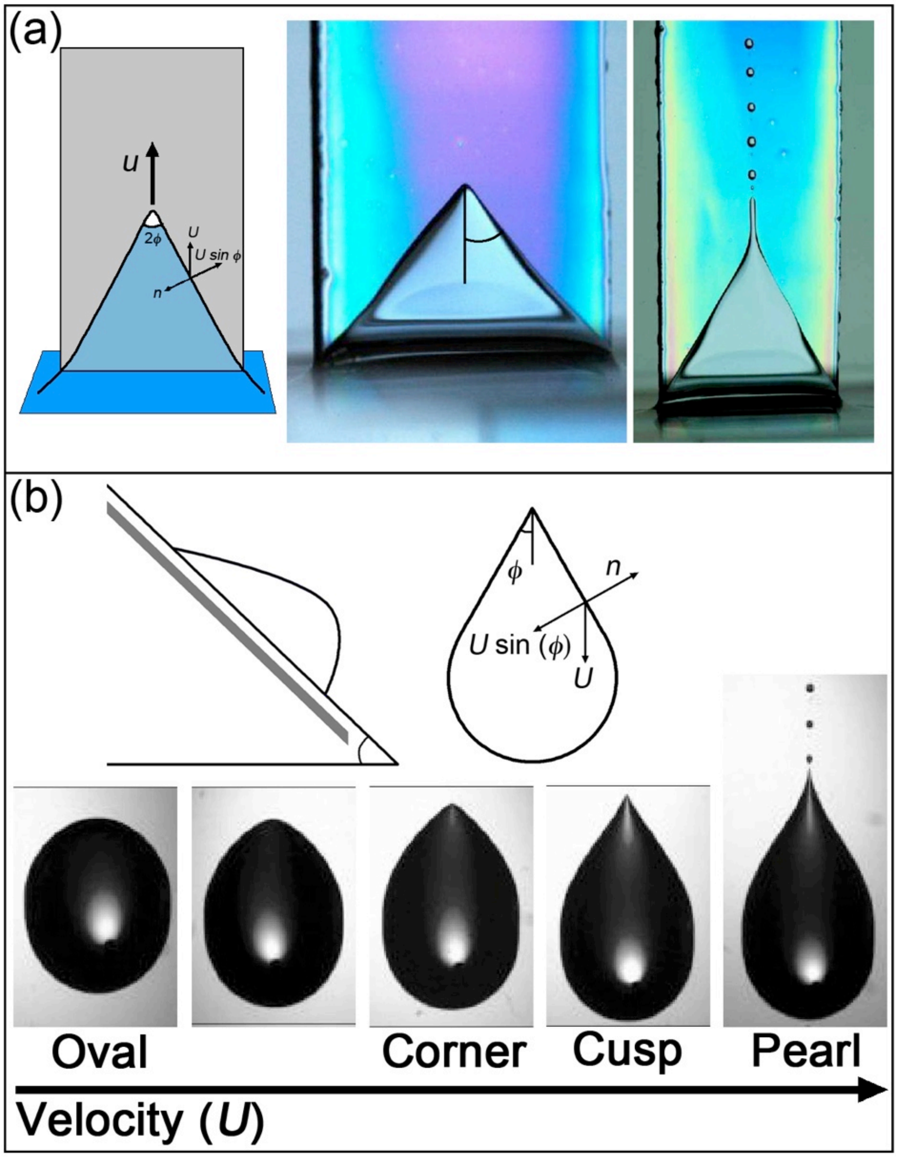

Figure 1.5 Changing morphologies of receding contact line. (a) A sawtooth-like wetting line is formed when a solid plate is withdrawn from a liquid [87]. (b) Inclined contact line on the rear of the droplet as it runs down a plane. Droplets show different regimes such as Oval, Corner, Cusp and Pearl as the velocity increases [88, 89].

An intriguing phenomenon on approaching limiting values for velocities is the possibility of contact lines to align with the flow direction. Since the dynamic contact angle varies between 0° and 180°, we obtain two limiting velocities as V_R and V_C [Figure 1.5(b)]. Advancing critical velocity V_C represents the maximum velocity with which the contact line can advance as $\theta \rightarrow 180^\circ$. Similarly, the maximum dewetting velocity V_R represents the maximum velocity with which a liquid can recede from a solid as $\theta \rightarrow 0$. Forcing velocities larger than the advancing and receding limits on the contact line would result in a variety of wetting transitions [80, 90-93]. For example, in the case of a solid withdrawing from a liquid with a velocity $U > V_R$, the dewetting line inclines at an angle ϕ reducing the velocity component normal to the contact line so that $U \sin(\phi) < V_R$ [94]. With sawtooth-like configuration contact line aligns with flow direction [Figure 1.5(a)] ensuring the component of velocity normal to the contact line $U \sin(\phi)$ do not exceed maximum dewetting velocity V_R [94]. This was first demonstrated by Blake and Ruschak [95] when a solid plate is withdrawn from a liquid with $U > V_R$. A similar transition occurs when a droplet runs down an inclined plane [Figure 1.5(b)] where the receding contact line on the rear of droplet adopts different shapes such as oval, corner, cusp and pearl depending on the velocity [88, 89]. These transitions result from the minimization of the normal component of dewetting velocity.

1.7. Coalescence of droplets

Drop coalescence occur at many different contexts such as emulsion stability[96, 97], sintering process[98], food production [99, 100] and multiphase flows [101]. Coalescence is the process by which two droplets come together and merge by the action of capillary forces. Coalescence between two liquid drops starts by the thinning and breakage of the thin film between the drops establishing a liquid bridge and its subsequent growth by displacing the outer fluid as it evolves. The most common approach to bring together coalescing droplets is to control the flow of the carrier fluid [102, 103]. Often, one instance of coalescence is followed by an avalanche as a result of locally induced extensional flow [103, 104]. Recent studies using microfluidic chips to study coalescence have demonstrated that coalescence of droplets happens as they separate rather than during collision [103, 105, 106]. Other experimental investigations of coalescence involves usage of high-speed photography in different configurations such as coalescing pendent and sessile droplets [107] and by merging of two droplets on a flat surface [108, 109].

Theoretical studies and simulations have shown that evolution of liquid bridge has two regimes namely a viscous regime [110] followed by an inviscid regime [111]. This regime characterization is based on a viscous length scale given by $l_v = \eta/\gamma\rho$. Scaling laws show that the radius of liquid bridge grows as $r_b \sim t^{1/2}$ in inviscid regime while it grows at lower rate $r_b \sim t\ln(t)$ in viscous regime. For typical fluids like water ($l_v = 140Å$) and mercury ($l_v = 4Å$) these length scales are too small to observe the viscous regime [112]. The existence of viscous regime has been experimentally confirmed by decreasing the surface tension by orders of magnitude using a colloid polymer mixture [113] and also by coalescing oil droplets in a carrier fluid [114, 115]. The inviscid scaling law for the inertial regime was verified by Wu *et al.* [116].

1.8. Two phase flow in microgeometries

Understanding the hydrodynamics of simple two-phase flows is fundamental to engineer multiphase flows in more complex microchannel networks. Such flows can be found in multifunctional microfluidic devices, ground water hydrology [117, 118], oil recovery [119-122], water-oil filtration [123-125], and fuel cells [126]. Typically, two-phase flow in microchannels is generated by focusing a droplet phase in a stream of external phase[127]. Droplets are produced periodically in microchannels by the pinching action of external phase on droplet phase [128]. Unlike droplet pinch-off in the context of free surface flows where inertial forces are non-negligible [129], droplet formation in micro-channel involves the interplay between surface tension and viscosity [58]. In these conditions, key non-dimensional number to quantify the visco-capillary balance is the capillary number *Ca* given by [70],

$$Ca = \frac{Viscous\ force}{Capillary\ force} = \frac{\eta U}{\gamma} \qquad (1.9)$$

Usually, the viscosity η in the capillary number is taken to be the largest of the viscosities between two phases. Although this is the normal practice, the viscous effect has to be quantified as a combination of the two viscosities when two phases of comparable viscosities are used. After formation, droplets transverse through the microchannel lubricated by external phase. Often this lubricating thin film breaks down resulting in a three phase contact line highly altering flow morphology.

In general, the flow combination of two immiscible fluids in microgeometries introduces three different types of interactions which can be classified as (a) Either of the phases totally wet the microgeometry (total wetting) while the second phase is always lubricated (b) The fluid-fluid interface can form a contact line on the solid (partial wetting) and (c) The fluid-fluid interfaces can come together and merge (coalescence). Although these interactions are straightforward, the confinement of capillary surfaces leads to non-trivial influence on flow dynamics. Added to the complexity are the hysteretic nature [130] and effect of viscosity on the contact line motion [131], the possibility of wetting lines to align with the flow direction to form saw-teeth like shapes [88], marangorni effects caused by surfactant [45] and dewetting of thin films on surface heterogeneities [132]. The aim of this thesis is to explore these interactions in detail under different flow conditions and microgeometries in forced micro flows. Specially, we investigate the influence of the viscosity of the two immiscible phases on droplet dynamics and coalescence in microchannels. To further our current understanding of confined multiphase flows, we make use of microfluidics and present a comprehensive study on the individual as well as the collective behavior of droplets in microchannels.

2. Droplet spreading and the dynamics of contact line.

Spreading of liquid droplets on solid surfaces are of key importance in many applications and can be observed in many instances such as oil recovery [133, 134], deposition of pesticides on plant leaves [135], drainage of water from highways [136] and inkjet printing [137-139]. Most of the experimental studies on droplet spreading are conducted in air neglecting the viscous contributions of external phase. These studies have shown that droplet spreading is governed by different physical mechanisms at various timescales [140]. The inertia-capillary balance (inertial regime) dominates the initial dynamics and the later stage of spreading (viscous regime) is the result of visco-capillary balance. While the earlier works have studied the influence of wettability on the time dynamics of the droplet spreading [141, 142], we focus on the viscous contributions in droplet spreading. We show that viscous contributions cannot be neglected in the inertial regime when the spreading happens in an external phase.

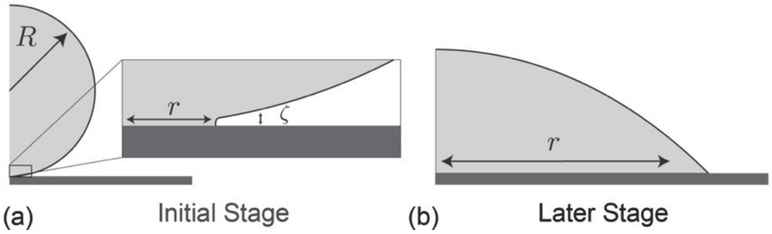

Figure 2.1 Schematics representing early and final stages of droplet spreading. The length scale ζ determines the curvature and thus the driving force[141].

During the initial stages of spreading, the system is far from equilibrium and the point at which droplet makes initial contact with solid represents a singularity. After the initial contact, the spreading diameter grows minimizing the total energy of the system until reaching a minimal energy equilibrium state. During the early times, dynamics of droplet spreading is dominated by inertia and driven by the curvature ζ in the narrow gap between drop and solid substrate. In these studies, the kinetic energy is balanced by the interfacial stress $\rho(\mathrm{d}r/\mathrm{d}t)^2 \sim \gamma R/r^2$ assuming that curvature ζ scales as $\zeta \sim R/r^2$ [143, 144]. Here, r is the spreading radius, γ is the interfacial tension and R is the initial drop radius. The final scaling resulting from the balance of inertia and capillary forces neglecting viscous contributions of the outer fluid is given by $r \sim t^{1/2}$ [142]. In all these formulations, the scaling of curvature ζ with the spreading radius r essentially determines the exponent for time t. Courbin *et al.* have proposed a more generalized scaling law [140, 145] as $r \sim t^{2/(\beta + 2)}$ with the value of β given by the scaling for curvature ζ. For droplet spreading on various partially wetting surfaces, there is an additional dependency for the exponent α in the scaling $r \sim t^{\alpha}$ based on the wettability of substrate and this has been modeled as $\alpha = (F(\theta_E) + \cos\theta_E)^{1/2}$ [142]. Briefly, the exponent α is determined by the curvature as well as the wettability of substrate. In the series of experiments presented here, we isolate the viscous contributions by considering droplets of similar size on an identical solid substrate.

During the later stage of spreading, drop assumes a nearly spherical cap and the balance of viscous and capillary forces dictates the evolution of spreading radius. This balance gives Cox-Voinov law, relating dynamic contact angle to capillary number $\theta^3 \sim Ca$ [74, 75]. Over long term for perfectly wetting fluid, the spherical cap approximation combined with contact line dynamics leads to Tanner's law as $r/R \sim (\gamma t/\eta R)^{1/10}$ [146-148]. However, this law holds only when the droplet evolves slowly and can be approximated to a spherical cap [149, 150].

To better understand the natural spreading process and the influence of a viscous outer fluid, we design an immersed droplet spreading/retraction experiment with fluid pairs of similar interfacial tension. This allows us to experimentally classify the role of viscosity of both fluid phases on contact line dynamics. Droplet is deposited on to a solid substrate immersed in a bath of the external phase to generate a dynamic three-phase contact line. The advancing contact line is studied when the droplet spreads on the glass slide while a deposited droplet is sucked up from the glass slide to examine the motion of the receding interface. Specifically, we are interested in the influence of viscosity of external and droplet phase on contact line motion. In this chapter we describe the experimental setup followed by the analysis of the data from the experiments.

2.1. Experimental setup and fluid properties

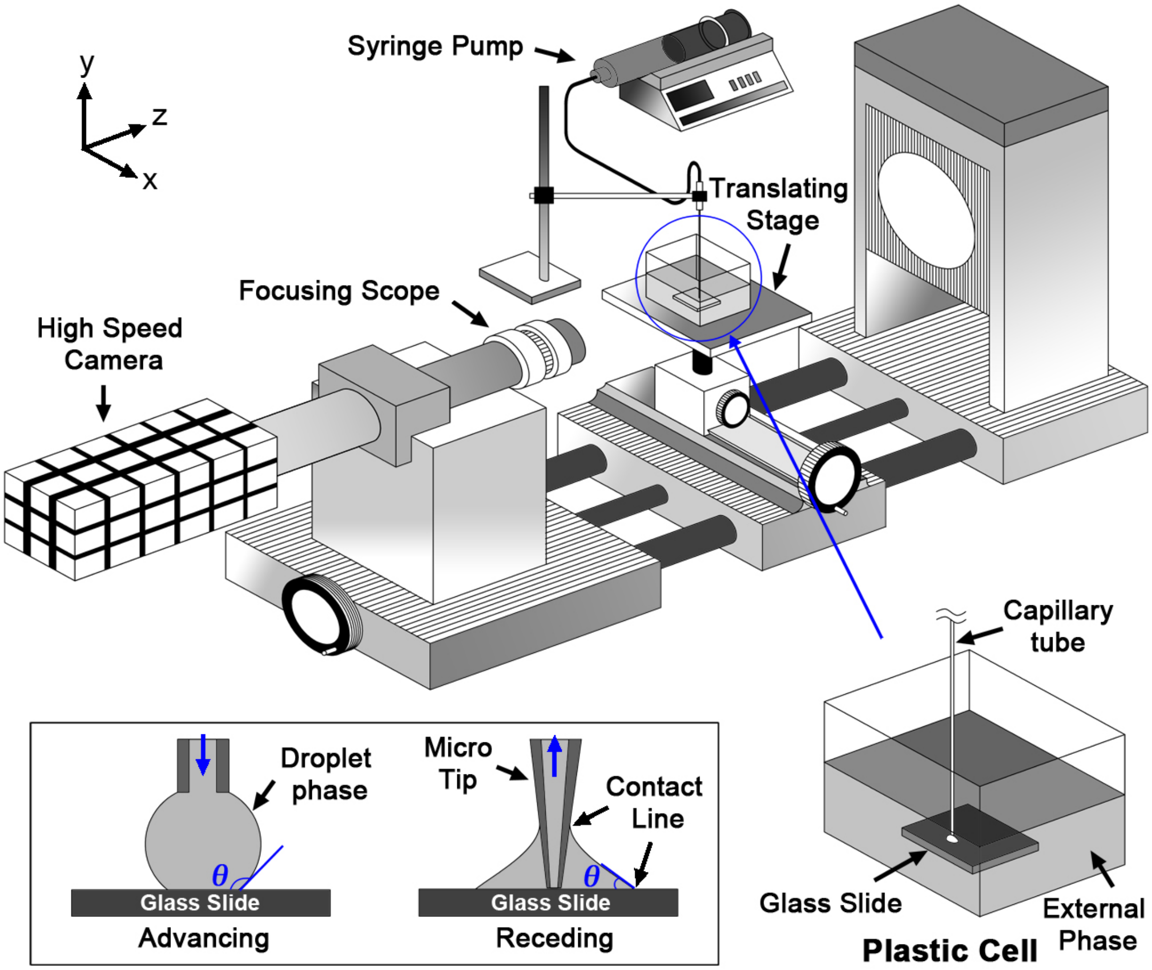

Figure 2.2 Schematic of experimental setup. Inset: The capillary tip used for droplet deposition (advancing) and droplet retraction (receding). Blue arrow shows the direction of fluid flow.

To visualize the immersed droplet spreading/retraction experiments, a high-speed camera (*AOS Technologies AG – XPRI*) is mounted on a goniometer (*Dataphysics – OCA 15plus*). The experimental images are acquired using the high-speed camera with a triggering mechanism and a data acquisition program from the manufacturer (*AOS imaging studio*). The frame rate (from 50 to 4000 frames per second) for each acquisition is adjusted to suite the time scale of the recorded experiment and the spatial resolution is about 10μm. Adjusting the focusing scope and translating stage the region of interest is brought to the field of view. A borosilicate glass slide (*McMaster Carr*) is placed inside the glass cell filled with external phase. Before transferring to the plastic cell, glass slide is baked at 400˚ C for one hour in the oven and brought back to room temperature inside the oven. The deposition and retraction of droplet phase is carefully regulated using a gas tight syringe (*Hamilton*) and a syringe pump (*New era pump systems*) connected to a capillary tube (*Sutter instrument company*) through polymer tubing (*Upchurch scientific*). For the suction of droplet phase, the tip of capillary tube is tapered to form a micro-tip using a flaming pipette puller (*Sutter instrument company*). To retract droplet phase from the glass slide, the capillary tube is carefully introduced inside droplet by slowly raising translating stage in positive y direction. The capillary penetrates droplet to form a contact line. By using a micro-tip, it is ensured that the contact angle θ of the fluid-fluid interface on the glass slide is unaffected by the contact line on the micro tip.

2.1.1. Fluid Properties

The droplet phase consists of water (*Sigma-Aldrich*), water-glycerol (*Sigma-Aldrich*) mixtures and PDMS oils (*Gelest*), and the external phase is either air or PDMS oil. No surfactants were used in the system. Each fluid pair is given a name and fluid pairs are categorized into three namely 1) WS: droplet phase – water, external phase – PDMS oil, 2) GS: droplet phase – water-glycerol mixture, external phase – PDMS oil and 3) A: droplet phase – PDMS oil, external phase – air. The ratio of the water-glycerol mixture is adjusted to vary the viscosity of the droplet phase while the PDMS oils of varying viscosities and air is used for the external phase. The viscosity of the droplet phase is given as η_1 and external phase as η_2 with a viscosity ratio between them as $\chi = \eta_1/\eta_2$. The interfacial tension between the fluids is given by γ_{12}. The interfacial tension is measured by double capillary rise method [Appendix A] and verified with tensiometer measurements (*Attension Sigma 700*).

Fluid pair	Fluid group	Droplet phase	η_1 (cP)	External phase	η_2 (cP)	Symbol	γ_{12} (mN/m)	θ_{Am} (Deg)
W-1cS	WS	Water	1	PDMS	0.8	○	40.7	65
W-5cS		-	-	-	4.6	□	42.7	65
W-20cS		-	-	-	19	△	42.7	88
W-50cS		-	-	-	48	▽	42.7	89
W-100cS		-	-	-	96.6	◁	42.7	98
W-200cS		-	-	-	193.6	▷	42.7	100
W-500cS		-	-	-	485.5	✧	42.7	113
W-1000cS		-	-	-	971	◊	42.7	121
W-10000cS		-	-	-	9740	◇	42.7	137
G92-20cS	GS	G92	1275	PDMS	19	△	29.3	73
G92-100cS*		-	-	-	96.6	◁	29.3	81
G92-5cS		-	36	-	4.6	□	29.3	53
G80-5cS		G80	272	-	-	□	29.7	41
G99-5cS		G99	1275	-	-	□	29.7	31
G80-1000cS		G80	36	-	971	◊	29.7	107
G92-1000cS		G92	272	-	-	◊	29.3	120
G99-1000cS		G99	1275	-	-	◊	27.7	131
1cS-A	A†	1cS	0.8	Air	0.02	●	17.4	0
10cS-A		10cS	9.4	-	-	◢	20.1	0
100cS-A		100cS	96.6	-	-	◀	20.9	1
1000cS-A		1000cS	971	-	-	◆	21.2	2
IA		Isopropanol	2.9	-	-	⬟	20.5	11

Table 2-1 Fluid pairs, properties and codes used in the experiment. $\theta_{Am} = \theta(V)$ is the measured advancing contact angle at velocity $V = 10\mu$m/s. * G92 means the liquid is made of 92% glycerol and 8% water by volume. PDMS oils are labeled based on the kinematic viscosity. Fluid pairs are labeled as a combination of droplet phase and the external phase. Droplet phase is denoted first followed by the external phase separated by a hyphen. For example the fluid pair G92-100cS means droplet phase is G92 and PDMS oil of ν = 100cS is the external phase. Symbol for each fluid pair is chosen based on the external phase while the color of the symbol is chosen based on the droplet phase: W (black), G80 (green), G92 (blue), G99 (red). † Spreading experiments in air (A) were performed on untreated glass.

2.2. Initial dynamics of droplet on glass slide

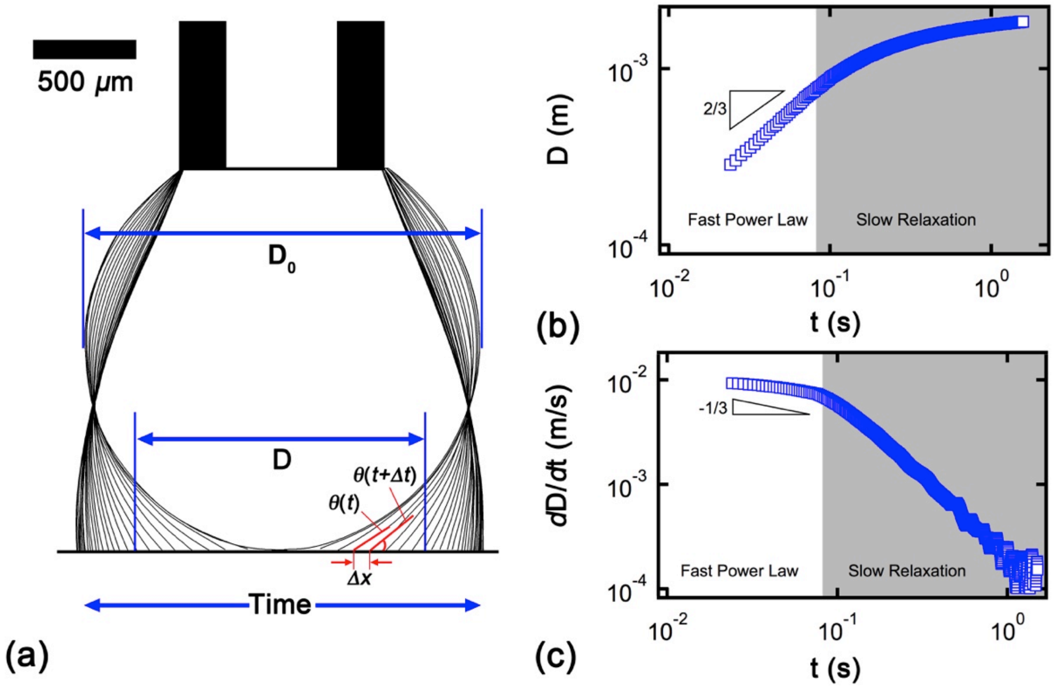

Figure 2.3 (a) Superimposed contours of a spreading droplet on glass slide. D_0 is the initial diameter of the droplet before spreading. (b) Evolution of droplet diameter D on the glass slide as a function of time t. (c) Rate of change of spreading diameter dD/dt with time t. Fluid pair: G92-5cS.

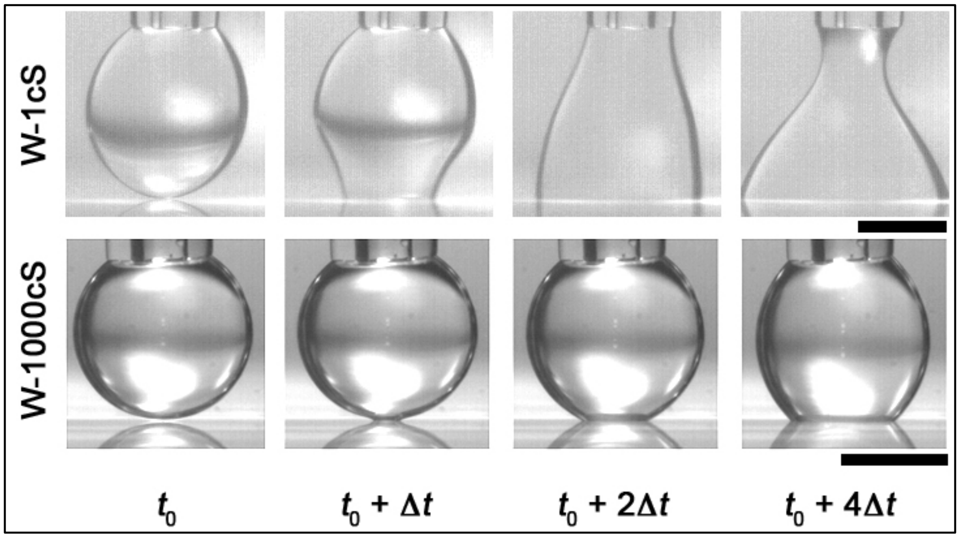

Figure 2.4 Time series of short-term evolution of spreading diameter with $\Delta t = 2.5 \times 10^{-3}$s for W-1cS and $\Delta t = 5 \times 10^{-1}$s for W-1000cS. Scale bar is 1mm.

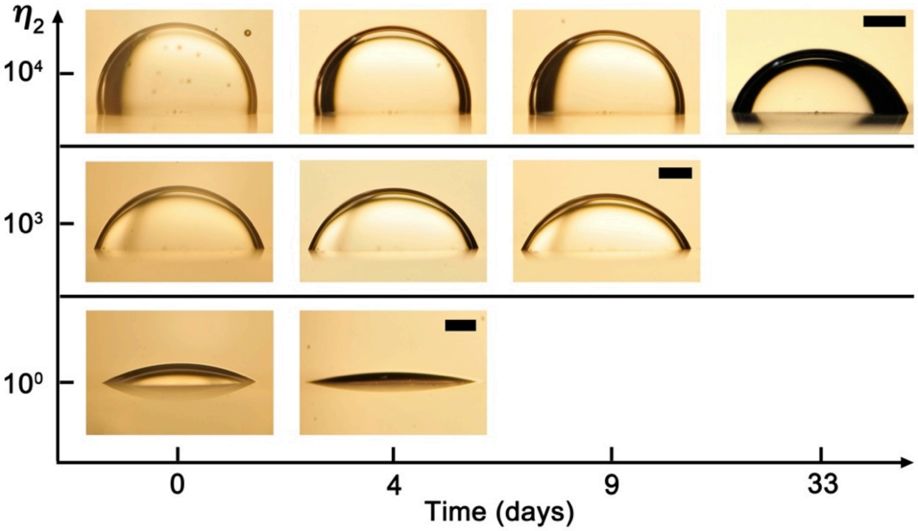

Figure 2.5 Long term evolution of spreading diameter. Water droplet in PDMS oils. Scale bar is 1 mm. Capillary tube is removed after deposition.

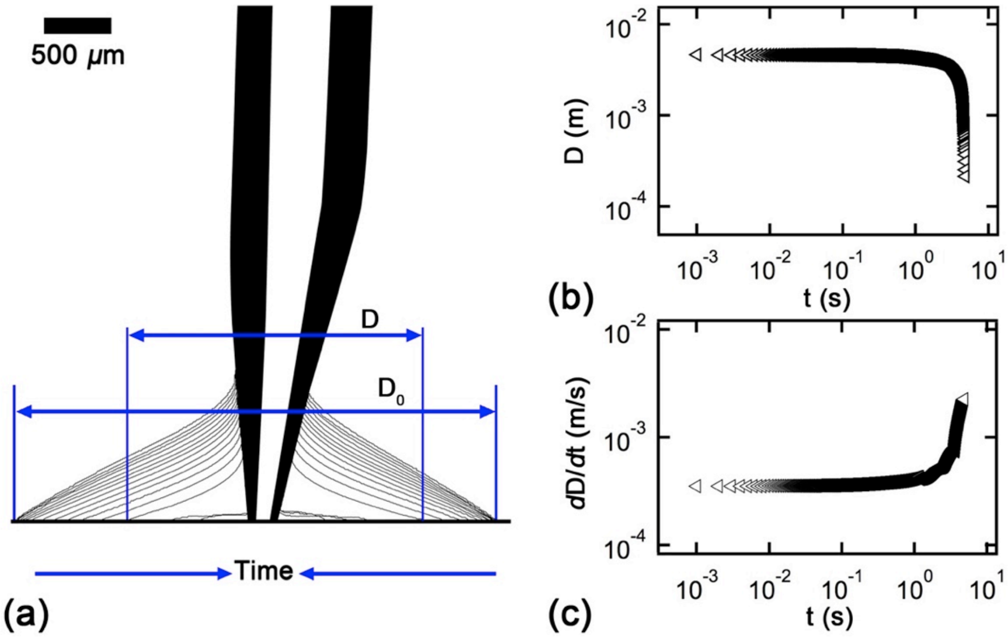

Figure 2.6 (a) Superimposed contours of a retracting droplet on glass slide. D_0 is the initial diameter of the droplet deposited on glass. (b) Evolution of droplet diameter D on the glass slide as a function of time t. (c) Derivative of the spreading diameter dD/dt with time t. Fluid pair: W-100cS.

To determine the natural spreading dynamics, the droplet phase is deposited on a borosilicate glass when immersed in an external phase. The focusing scope is slightly tilted (< 5˚) with respect to the translating stage to obtain the reflection of the droplet image on the glass. The elevation between light source and the translating stage is adjusted in such a way that light is internally reflected inside the glass. This technique allows a clear visualization of droplet and reflected image as the droplet approaches glass slide. Droplets are slowly generated at the tip of the capillary tube by regulating the flow rate from the syringe pump. The shape of the droplet corresponds to a spherical cap of diameter D_0 which is below the capillary length $[\gamma_{12}/(\Delta\rho g)]^{1/2}$. The value of D_0 is kept between 0.8 and 2 mm and the influence of size of the droplet on droplet spreading is not explored in this set of experiments. Keeping the droplet attached to the tip of the capillary is beneficial in manipulating droplet in the viscous matrix while carefully regulating the curvature of spreading droplet. Droplet makes contact with the glass slide after the rupture of thin film of external phase between the glass slide and droplet. For highly viscous system, we observed a longer time for the spreading to initiate. The time required for the initial contact with solid may vary between $\sim 10^{-4}$ to $\sim 10^{3}$ seconds depending on the viscosity of the external phase. As the droplet spreads on the glass slide, a circular contact line is formed, moving radially outward from the center of the droplet.

The evolution of the contact line diameter D of the spreading droplet is extracted from the spatiotemporal diagram is used to generate the curves in Figure 2.3(b-c). As the droplet spreads, the contact line velocity decreases slowly reaching zero $V \rightarrow 0$. Evolution of spreading diameter D showed two regimes namely a fast power law regime in the beginning followed by a slow relaxation regime. We name this regime "power law" regime rather than "inertial" as the viscous contributions cannot be neglected and the spreading is no longer a simplified balance between inertial and capillary forces. In the fast power law regime, droplet diameter scales with time with a constant exponent as $D \sim t^{2/3}$. The exponent continuously decreases on crossing over to slow relaxation regime. A similar crossover to a slow relaxation regime was observed for colloidal particles suspending at fluid interfaces [151, 152]. The cross over is marked by sudden drop in power law scaling which is steadily observed when plotting the derivative $\mathrm{d}D/\mathrm{d}t$ with time [Figure 2.3(c)]. At longer time scales in the slow logarithmic regime, the derivative $\mathrm{d}D/\mathrm{d}t$ fluctuates indicating discreet jumps of contact line. The relaxation time can take up to 30 days in the case of highly damped viscous system such as W-10000cS [Figure 2.6].

The motion of the receding interface is studied by drawing the liquid out from a droplet deposited on a glass slide in a bath of PDMS oil. Since the receding contact angle θ_R of the fluid pair has to be large enough (> 30˚) to materialize the retraction of droplet only fluid group WS was used to conduct droplet retraction experiments. The contact line starts from rest with an initial contact line of diameter D_0 and the diameter D decreases as the fluid inside the droplet drains out [Figure 2.6(b-c)]. The retraction of droplet is achieved by imposing a constant withdrawal rate on the syringe pumps, setting the velocity for contact line. The velocity increases in time as the droplet shrinks and the contact line move radially inwards towards the tip of the capillary. The retraction of droplet on a solid surface is a forced wetting transition when compared to spreading of droplet determined by the natural properties of fluids. During droplet retraction, the balance of viscous and capillary forces dominates the initial dynamics. We noticed a reduction in the initial velocity with increasing viscosity of the external phase.

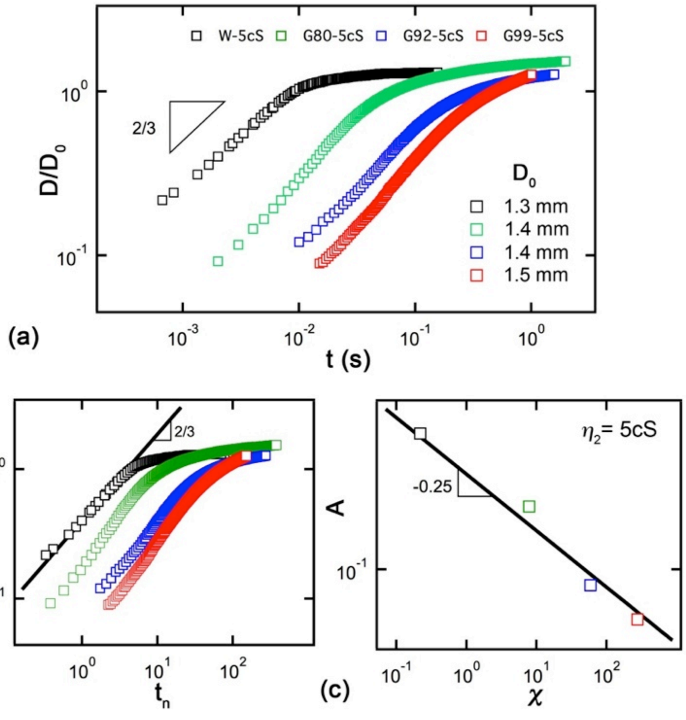

Figure 2.7 Evolution of normalized spreading diameter with varying viscosities of droplet phase η_1 in an external phase of 5cS PDMS oil. (a) Normalized spreading diameter $D_n = D/D_0$ with time t and (b) with non-dimensionalized time $t_n = t/\tau$ with $\tau = (\Delta\rho D_0^3/\gamma_{12})^{1/2}$. Solid line: $D_n = At_n$ with $A = 0.4$. (c) Coefficient A is plotted with viscosity ratio χ. Solid Line: $A = 0.35\chi^{-0.25}$.

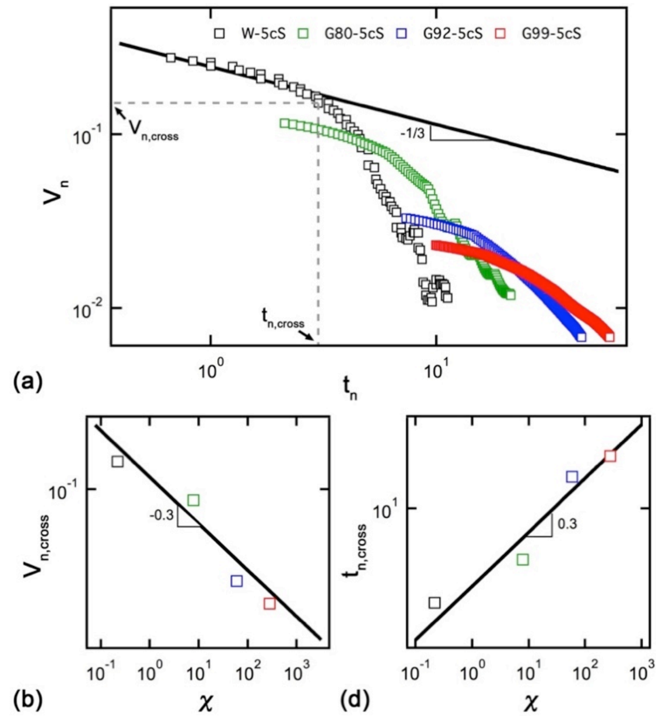

Figure 2.8 (a) Evolution of rate of change of normalized spreading diameter V_n with t_n for varying viscosities of droplet phase η_1 in an external phase of 5cS PDMS oil. Solid Line: $V_n = 0.25t_n^{-1/3}$. (b) Cross over velocity $V_{n,cross}$ with viscosity ratio χ. Solid Line: $V_{n,cross} = 0.12\chi^{-0.3}$. (c) Cross over time $t_{n,cross}$ with viscosity ratio χ. Solid Line: $t_{n,cross} = 3.7\chi^{0.3}$.

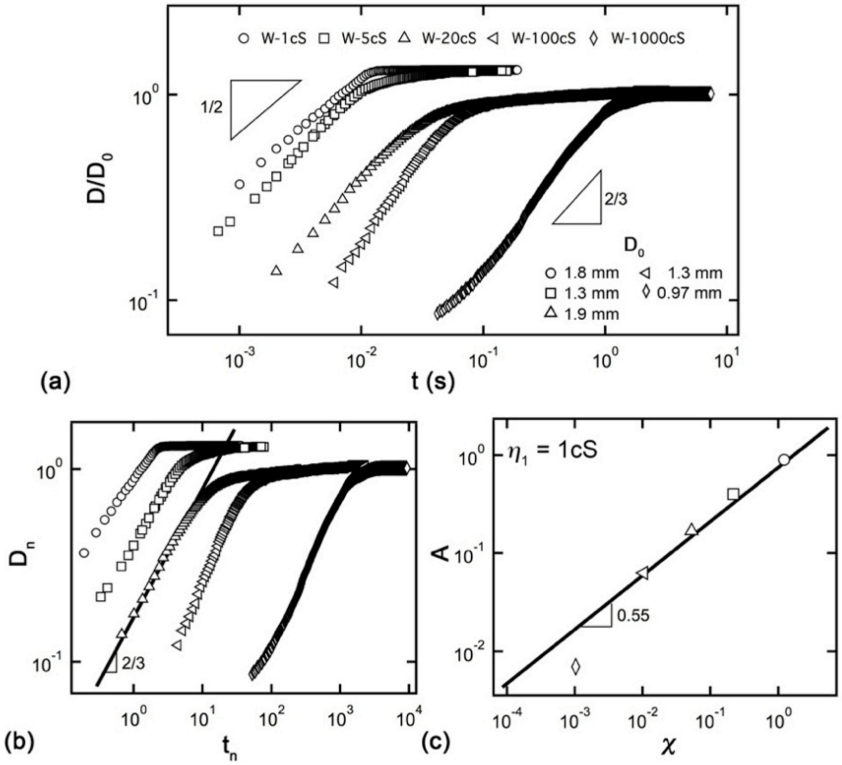

Figure 2.9 Evolution of normalized spreading diameter for droplet phase η_1 = 1cS in varying viscosities of external phase η_2. (a) Normalized spreading diameter $D_n = D/D_0$ with time t and (b) with non-dimensionalized time $t_n = t/\tau$ with $\tau = (\Delta\rho D_0^3/\gamma_{12})^{1/2}$. Solid line: $D_n = At_n$ with $A = 0.17$. (c) Coefficient A is plotted with viscosity ratio χ. Solid Line: $A = 0.75\chi^{0.55}$.

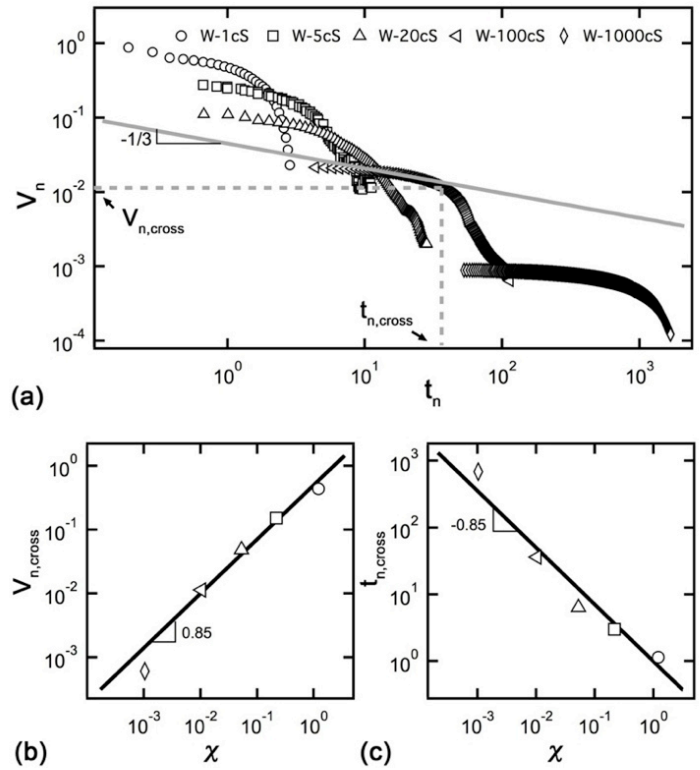

Figure 2.10 (a) Evolution of rate of change of normalized spreading diameter V_n with t_n for droplet phase η_1 = 1cS in varying viscosities of external phase η_2. Solid Line: $V_n = 0.0058 t_n^{-1/3}$ (b) Cross over velocity $V_{n,cross}$ with viscosity ratio χ. Solid Line: $V_{n,cross} = 0.4\chi^{0.85}$ (c) Cross over time $t_{n,cross}$ with viscosity ratio χ. Solid Line: $t_{n,cross} = \chi^{-0.85}$

To quantify the viscous contributions of ambient fluid in the early time dynamics, we consider the power law regime where the exponent is constant. We choose fluid pairs of similar interfacial tension to isolate viscous contributions. At first, the viscosity of the droplet phase η_1 is varied for over three decades while keeping external phase same [Figure 2.7]. The evolving diameter D is normalized by initial diameter D_0 of the droplet as $D_n = D/D_0$ and time t is normalized by the inertial time scale $\tau = (\Delta\rho D_0^3/\gamma_{12})^{1/2}$ to give the normalized time as $t_n = t/\tau$. Here $\Delta\rho$ represents difference in density and γ_{12} is the interfacial tension. Since the early time dynamics is described by the power law regime, we curve fit this regime with a coefficient A as $D_\mathrm{n} = At_\mathrm{n}^{2/3}$. The coefficient A plotted as a function of viscosity ratio χ. The relative magnitude of A is a measure of the relative speed of spreading in the power law regime. At first we change the viscosity of the droplet phase η_1 while keeping the external phase η_2 constant. From the data we find that influence of coefficient A on the viscosity of droplet phase can be given by $A = 0.35\chi^{0.25}$ for 5cS external phase [Figure 2.7(c)]. We also noticed that exponent of time in the interval regime is 2/3, slightly larger than the values reported for experiments in air[140]. Since the curvature ζ plays a major part in determining the exponent, we keep the droplet size distribution as narrow as possible assuming the influence of curvature ζ on the exponent to be minimal. The validity of this assumption is supported by similar values of exponent for different set of experiments for various fluid pairs. To understand the influence of external phase, we keep the droplet phase as water and the external phase is varied from 1cS to 1000cS PDMS oils [Figure 2.9]. By varying the external phase, we found that the coefficient in the equation $D_\mathrm{n} = At_\mathrm{n}$ scales with the viscosity ratio as $A = 0.75\chi^{0.55}$.

Focusing on the cross over from power law regime to slow relaxation regime, we noticed that the curve is smoother as the viscosity of either phase is increased. This crossover to the slow relaxation can be easily observed when the derivative of normalized spreading diameter $V_\mathrm{n} = \mathrm{d}D_\mathrm{n}/\mathrm{d}t$ is plotted as a function of time t_n [Figure 2.8(a)]. From the scaling $D_\mathrm{n} \sim t_\mathrm{n}^{2/3}$, the derivative V_n follows a scaling $V_\mathrm{n} \sim t_\mathrm{n}^{-1/3}$. This crossover velocity $V_{\mathrm{n,cross}}$ and time $t_{\mathrm{n,cross}}$ is determined when the derivative V_n departs from the $-1/3$ scaling with time t_n. Both cross over velocity $V_{\mathrm{n,cross}}$ and time $t_{\mathrm{n,cross}}$ is found to vary with viscosity ratio and gives a quantitative estimation of the crossover to the slow relaxation regime. Similar trends are observed when the viscosity of the external phase η_2 is varied but with different exponents for the power laws involving A, $V_{\mathrm{n,cross}}$ and $t_{\mathrm{n,cross}}$. In the case of varying external phase (Fluid group: WS), there is slight difference in the final equilibrium value of D_n and we attribute this to higher relaxation time for a viscous ambient fluid (> 20cS) [Figure 2.9(a)]. Our results clearly shows that highly viscous systems are damped and take longer time to reach the final state [Figure 2.5].

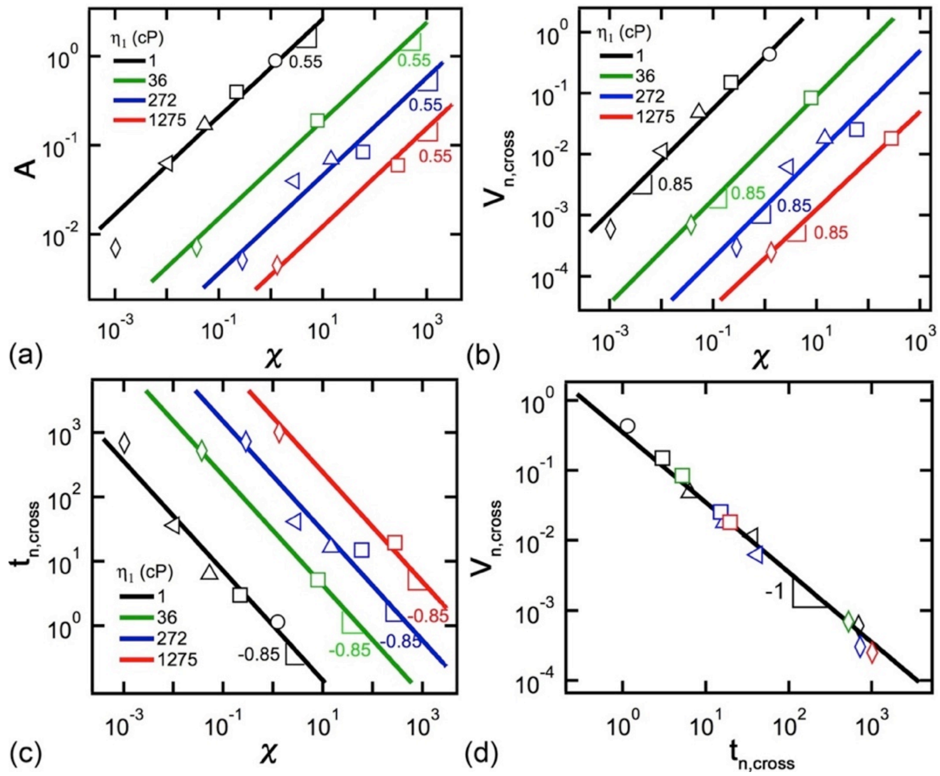

Figure 2.11 (a) Coefficient A with viscosity ratio χ. Solid Lines: $A = a\chi^{0.55}$ where a is a function of droplet phase viscosity η_1. (b) Cross over velocity $V_{n,cross}$ with viscosity ratio χ. Solid Lines: $V_{n,cross} = b\chi^{0.55}$ (c) Cross over time $t_{n,cross}$ with viscosity ratio χ. Solid Lines: $t_{n,cross} = c\chi^{0.85}$. Values of a, b and c is given in Table 2-2. (d) Crossover velocity $V_{n,cross}$ vs. Crossover time $t_{n,cross}$. Solid Line: $V_{n,cross} = 0.35t_{n,cross}^{-1}$.

Color	η_1 (cP)	a	b	c	d
Black	1	7.5×10^{-1}	4.0×10^{-1}	1.0	7.5×10^{-1}
Green	36	5.4×10^{-2}	1.3×10^{-2}	3.0×10^{1}	5×10^{-3}
Blue	272	1.3×10^{-2}	1.4×10^{-3}	2.1×10^{2}	3×10^{-4}
Red	1275	3.5×10^{-3}	2.0×10^{-4}	1.7×10^{3}	4×10^{-5}

Table 2-2 Non-dimensional curve fitting parameters for Figure 2.11(a-c) and Figure 2.14(a).

To show the combined effect of the viscosity of both phases in the fast power law regime, phase diagrams are presented in Figure 2.11. The coefficient A scales with the viscosity ratio as $A \sim \chi^{0.55}$ for a given droplet phase η_1. In general, the coefficient A can be given as $A = a\chi^{0.55}$ where a is a function of the droplet phase as $a = f(\eta_1)$ for all the fluid pairs investigated. Along each solid line in Figure 2.11(a), the viscosity of the external phase η_2 decreases with increasing χ and the viscosity of the droplet phase η_1 increases as we go from Black to Green to Blue to Red. The magnitude of coefficient A in the phase diagram [Figure 2.11(a)] signifies a relative slow down of spreading process with increasing viscosity of either phase. In the phase diagram, coefficient A varies over three decades in magnitude from 1 =to 10^{-2} when viscosity ratio equals unity $\chi = 1$. Such wide variation in magnitude for a given viscosity ratio signifies a marked influence of the absolute viscosity. The phase diagram clearly demonstrates the influence of each phase and not simply the viscosity ratio in determining evolution of spreading curve. Similarly, the relative influence of both droplet and external phase can be observed for the crossover time $t_{\mathrm{n,cross}} = c\chi^{0.85}$ and crossover velocity $V_{\mathrm{n,cross}} = b\chi^{0.55}$ with b and c varying as a function of droplet phase $f(\eta_1)$ [Figure 2.11(b-c)]. Although crossover velocity and time change with viscosity of either phase, the relation between two parameters remain constant $V_{\mathrm{n,cross}} = 0.35t_{\mathrm{n,cross}}^{-1}$ irrespective of fluid pairs [Figure 2.11(d)].

2.3. Contact angle and critical velocity

2.3.1. On the effect of viscosity of single phase

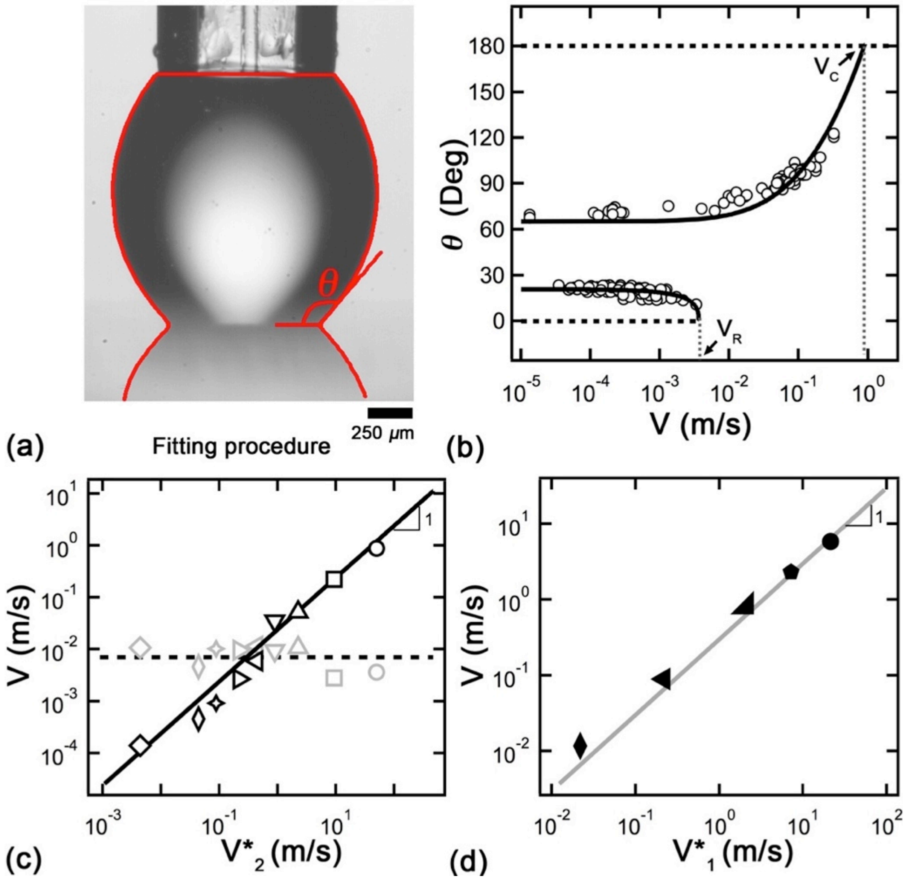

Figure 2.12 (a) Curve fitting procedure used on the experimental micrograph to locate the contact line and dynamic contact angle. (b) Contact angle θ as a function of contact line velocity V. Fluid Pair: W-1cS. Solid Line: $\theta = (\theta_0^3 \pm \omega V)^{1/3}$. (c) V_C (Black) and V_R (Gray) as a function of capillary velocity for fluid group WS. Solid line: $V_C = Ca_{c2}.V^*_2$ with $Ca_{c2} = 2.4 \times 10^{-2}$ and $V^*_2 = \gamma_{12}/\eta_2$, Dash line: $V_R = 7 \times 10^{-2}$. (d) V_C as a function of capillary velocity for fluid group A. Solid Line (Gray): $V_C = Ca_{c1}.V^*_1$ with $Ca_{c1} = 3 \times 10^{-1}$ and $V^*_1 = \gamma_{12}/\eta_1$.

For better characterizing the dynamics of contact line in relaxation regime, we plot the contact angle as a function of velocity. The contact line is located at the point joining the droplet image with its reflection. The apparent contact angle θ is defined as the angle included between the solid substrate and the tangent of the fluid-fluid interface at the contact line measured from inside the droplet phase. The contact angle θ on each image is determined by defining the liquid-liquid interface as a B-spline curve using the "*drop analysis*" plugin combined with *ImageJ* [153]. The contact angle is measured on entering the viscous relaxation regime where the contact angle can be clearly defined with least ambiguity. We focus on the plane through the center of the droplet to avoid the misinterpretation of the contact angle. As the droplet spreads on glass, contact line velocity V decreases with time and contact angle θ reduces from 180˚ to static equilibrium angle θ_E. In a viscous medium, the contact line velocity is considerably reduced and may take a few days to reach complete equilibrium and weak mass transfer can occur across the interface [154-156]. Figure 2.5 shows the slow spreading of water droplets on a glass slide. By increasing the viscosity of the external phase η_2, the relaxation time required for complete spreading of the droplet is considerably increased. At low rates of movement, multiple low energy metastable states were observed where the contact line gets pinned at topographic and energetic irregularities on the solid surface leading to contact angle hysteresis. Since these metastable states do not capture the entire dynamics of the two-phase system, the contact angle should be described as a function of velocity $\theta(V)$. A minimum velocity of 10 μm/s is used to define the contact angle θ_{Am} and reported in Table 2-1.

To correlate θ with velocity of contact line V, images are imported from camera and assigned an angle and a coordinate for the contact line. Taking two images that are Δt apart, we measure the displacement of Δx of the contact line and assign a velocity $V=\Delta x/\Delta t$. The mean contact angle is assigned as $\theta = (\theta_t + \theta_{t+\Delta t})/2$ from the same pair of images used for calculating the velocity [Figure 2.12(a)]. The velocity of the receding interface is measured as the absolute value of the velocity. Cox-Voinov [74, 75] law gives a hydrodynamic description by balancing the viscous and capillary forces near contact line. Although the static contact angle is very hard to determine in a highly damped viscous system, introducing two fitting parameters θ_0 and ω in the Cox-Voinov relation can capture the evolution of the dynamic contact angle. We plot the contact angle as a function of velocity and use the Cox-Voinov relation $\theta^3 = \theta_0^3 + \omega V$, to extrapolate the data to find a critical velocity V_C for the advancing interface when $\theta \rightarrow 180°$. Similarly a critical velocity for the receding interface V_R is calculated for $\theta \rightarrow 0°$ [Figure 2.12(b)]. Limiting values for velocities are named as advancing critical velocity V_C (V at 180˚) and receding critical velocity V_R (V at 0°). Although the relation describes the contact angle in the limit of low capillary number $Ca << 1$, the data suggest this trend for all the fluid pairs investigated. Due to the uncertainty, very low contact angles below $\theta < 7^\circ$ are discarded. The static contact angles θ_{Am} along with the critical velocities V_C and V_R summarize the θ vs. V curves for all the various fluid pairs. The critical velocities are based on the fluid properties of the system and can be considered as a natural spreading parameter.

We proceed by examining the influence of one phase, while keeping the other phase constant. The capillary velocity is based on the viscosity of the changing phase as $V^*_{\ j} = \gamma_{12}/\eta_j$. In both cases, a) water droplets spreading in oils of varying viscosities and b) PDMS oils of varying viscosities spreading in air, we observed that the advancing critical velocity V_C scales with the capillary velocity as $V_C \sim V^*$ [Figure 2.12(c-d)]. The ratio of these velocities is given by a critical capillary number $Ca_{cj} = V_C/V^*_j$. The critical capillary number values for the fluid Group WS is $Ca_{c2} = 2.4 \times 10^{-2}$ and for the fluid group A is $Ca_{c1} = 3 \times 10^{-1}$. Surprisingly, the receding critical velocity remains constant around $V_R = 7 \times 10^{-2}$ m/s in the case of the fluid group WS. We were not able to extrapolate the receding critical velocities for other fluid groups due to low advancing static angle θ_R. In conclusion, variation of viscosity of one of the phases while keeping other constant gives an expression for critical velocity as $V_C = Ca_{cj}\ V^*_j$.

2.3.2. On the effect of heat treatment on glass slide

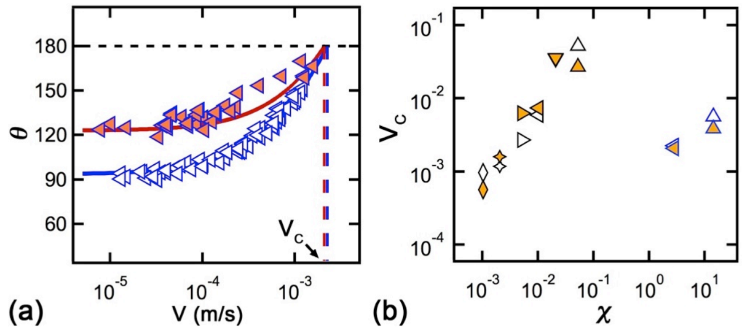

Figure 2.13 (a) Comparison of θ vs. V curves for heat-treated and untreated glass. Fluid pair: G92-100cS. Orange color filled symbols indicates untreated glass while open symbols are for heat-treated glass. (b) Comparison of maximum critical velocity V_C for treated and untreated glass.

To identify the effect of heat treatment, a direct comparison on the evolution of the contact angle with velocity is made for the heat-treated and untreated glass. Although the static contact angle θ_{Am} remained higher for various fluid pairs on the untreated glass, we only noticed minimal difference in the extrapolated advancing critical velocities [Figure 2.13(b)]. This confirms the choice of advancing critical velocity V_C as a fitting parameter to characterize the relative influence of the fluid viscosities irrespective of the contact angle θ_A.

2.3.3. On the combined effect of droplet and external phase

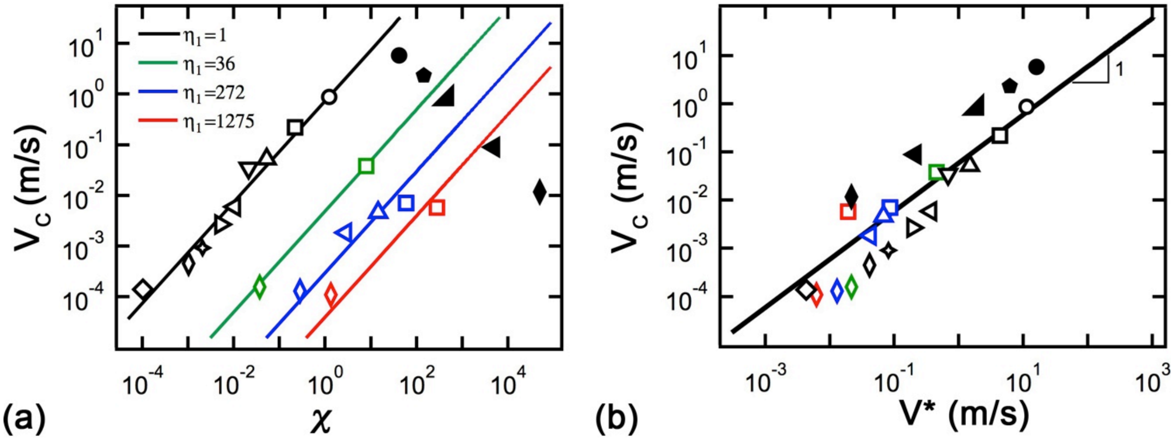

Figure 2.14 (a) Advancing critical velocity V_C as a function of viscosity ratio χ for varying viscosities of droplet and external phase. $V_C = d\chi$ with value for d give in Table 2-2. (b) Advancing critical velocity V_C vs. capillary velocity V^*. Solid line: $V_C = Ca_c.V^*$ with $Ca_c = 6.0 \times 10^{-2}$ and $V^* = \gamma_{12}/\eta_{12}$.

To determine the combined effect of both droplet and external phase on the advancing critical velocity V_C we extend our results to include all the fluid groups in Table 2-1. The combined effect is observed when plotting critical velocity V_C against viscosity ratio χ [Figure 2.14(a)]. For each droplet phase η_1 considered, we found a decreasing trend for critical velocity scaling inversely with viscosity ratio as $V_C \sim \chi^{-1}$, suggesting a reduction in V_C as external phase η_2 becomes more viscous. In general, the critical velocity for various droplet phase is given by $V_C = d\chi^{-1}$ with $d = f(\eta_1)$ and corresponding values are given in Table 2-2. The coefficient d decreases with η_1 capturing the effect of droplet phase. Irrespective of the droplet phase considered critical velocity V_C followed the same trend as $V_C \sim \chi^{-1}$. Plotting V_C vs. χ is justified, since the interfacial tension of the fluid pairs investigated are of similar in magnitude and hence follows $V_C \sim V^*$ for each droplet phase η_1. However, we noticed a marked difference in the critical velocities for experiments performed in air (Fluid group: A). We partially attribute this to the difference in wettability of the viscous oils in air, which makes almost totally wetting systems. In short, our result shows critical velocity V_C is a function of both phases since it differs highly for viscosity ratios close to unity $\chi = 1$.

We formulate an effective viscosity η_{12} for the two-phase system based on the viscosity of both phases to redefine capillary velocity as $V^* = \gamma_{12}/\eta_{12}$. The molecular kinetic theory on dynamic wetting suggests a contact line friction ratio λ, scaling linearly with liquid viscosity and exponentially with work of adhesion Wa as $\lambda \sim \eta e^{Wa}$ for an isothermal system [157-159]. For a two liquid system, Seveno *etal.* [160, 161] proposed a contact line friction factor as $\lambda_{12} = \lambda_1 + \lambda_2 + 2(\lambda_1\lambda_2)^{1/2}$ to describe contact line motion. The work of adhesion Wa depends on the interfacial tension, which is relatively constant in our case givng a scaling for the effective viscosity $\eta_{12} \sim \lambda_{12}/e^{Wa}$. We propose an effective viscosity for the two phase system as $\eta_{12} = \eta_1 + \eta_2 + 2(\eta_1\eta_2)^{1/2}$. The advancing critical velocity V_C is then plotted with capillary velocity V^* based on effective viscosity η_{12} and their ratio gives a critical capillary number as Ca_c [Figure 2.14(b)]. Although there is general agreement in the scaling $V_C \sim V^*$ for all fluid pairs, we noticed a difference with the fluid group A. This is attributed to the difference in interfacial tension values for this fluid group altering the work of adhesion. In short, a reasonable estimate on the advancing critical velocity V_C for a two fluid system can be given as

$$V_C = Ca_c V^* \qquad (2.1)$$

with $Ca_c = 6.0 \times 10^{-2}$

2.4. Droplet spreading on nanopatterned surfaces

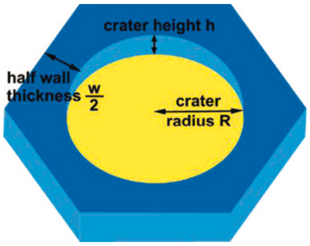

Figure 2.15 Schematic representation of one unit cell (nanocrater) of the nanopatterned layer [162].

Droplet spreading experiments were performed on nanopatterned surfaces to study the influence of nanopatterning in a viscous ambient fluid (100cS PDMS oil). In these set of experiments the water droplet is detached from the end of the capillary and slowly approach glass slide under the influence of gravity with negligible velocity through the external phase. Nanopatterned sample is prepared by dip coating an ultrathin layer of titanium tetraisopropoxide on microscope slide and curing at different temperatures inside an oven. The temperature and the rate of heat treatment determine the size of nanocraters on the glass slide. A detailed account on the preparation of the samples can be found in Refs [162] and [163]. Here, we have classified the prepared samples based on the static contact angle θ_E given in Table 2-3.

Sample	θ_E (In Air)	θ_E (In 100cS)	Color of Symbol
S1-Sm	-	110	Yellow
S1-Pt	45	75	Red
S2-Sm	31	121	Green
S2-Pt	25	60	Blue

Table 2-3 Table of properties of the patterned and smooth surfaces. Each glass slide baked in the oven has a smooth side as well as a nanopatterned side. The code for the samples is denoted by S1 – Sample 1, S2 – Sample 2, Pt – Patterned and Sm – smooth. Static contact angle θ_E is given in degrees.

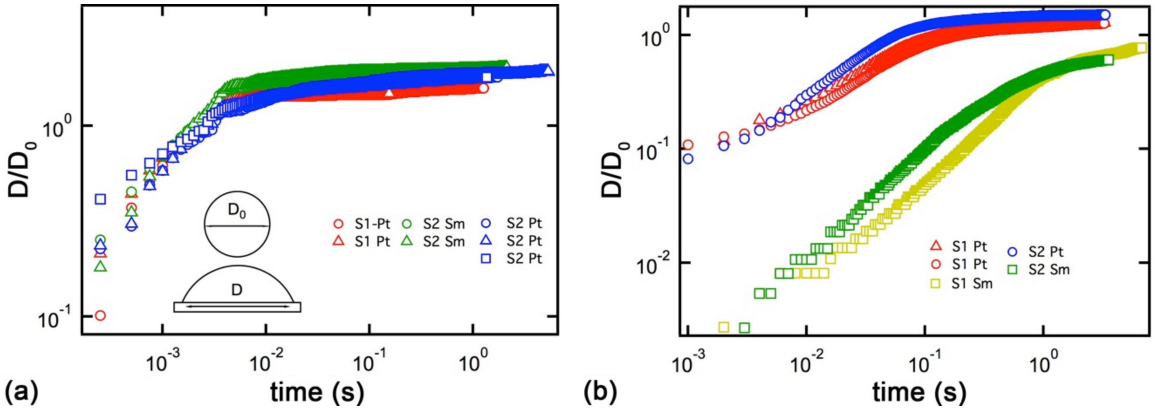

Figure 2.16 Evolution of spreading diameter in Air and 100cS PDMS oil. D_0 is the initial diameter before spreading and is kept around 1mm. Each symbol represents a different trial. (a) Fluid pair: W-Air (b) Fluid pair: Water-100cS

In air, curves of the evolution of spreading diameter are found to collapse together [Figure 2.16(a)]. On the contrary the evolution curves were found to be vastly different in a viscous medium of 100cS PDMS oil [Figure 2.16(b)]. Water droplets were found to spread faster on nanopatterned surface compared to smooth surface in an ambient fluid of 100cS PDMS oil. The unexpected change in the timescale of spreading process is attributed to the change in wettability of substrate on changing the ambient fluid, which sets the curvature ζ. Here we use nanopatterned surfaces to show the possibility of tuning the timescale of spreading process by changing the ambient fluid.

2.5. Conclusion

Using an experimental model for spreading in liquid-liquid systems, we quantified the viscous contributions of either phase. Knowledge of such prototype systems is essential for understanding wetting in microfluidic systems that often involves transport of multiple fluids where one of the phases can get attached to the walls. The spreading process showed two regimes namely, a power law regime and a slow relaxation regime. Prior literature on droplet spreading neglects the viscous contributions describing the early time dynamics of the spreading as balance of inertial and capillary forces. Our results extend to include viscous influence of both phases. We show that in the fast power law regime, spreading diameter follows the scaling law $D_n = At_n^{2/3}$ and the increase in either of the phases contributes towards slowing down of spreading process. A phase diagram based on A is presented to quantify the influence of viscosity of either phase on spreading process. We also noticed the viscous influence of external phase η_2 to be more prominent in reducing the speed of spreading process. Overall, in a two-fluid case, the influence of one fluid could not be neglected in determining rate of spreading process. Although the exponent for time t remains fairly constant the coefficient A varies with change of either phase. We show that viscosity ratio does not fully describe spreading process and the absolute viscosity of both phases is significant to entirely capture the spreading dynamics. We also examined the crossover from fast power law regime to slow relaxing regime by measuring the crossover velocity $V_{\mathrm{n,cross}}$ and crossover time $t_{\mathrm{n,cross}}$. The cross over is found to be smoother with increase of viscosity of either phase.

We observed that as the viscosity of the medium increases, the relaxation time for the contact angle θ to reach complete equilibrium θ_{E}, increases taking up to 33 days to complete the process. Due to the slow evolution of the spreading process, the definition of conventional static contact angle does not seem to be a fitting parameter to describe this process. It is more appropriate to define the contact angle as a function of velocity and we propose a static contact angle θ_{Am} based on a cut-off velocity. For all the fluid pairs tested, Cox-Voinov law fits data well to describe the motion of the contact line. Two critical values of velocity V_{C} and V_{R} are extracted from θ vs. V curves summarizing the curves for each fluid pair. The advancing critical velocity V_{C} was found to scale with the capillary velocity V^* irrespective of the fluid pairs.

We also studied the evolution of droplet spreading in nanopatterned surfaces by changing the ambient fluid. The results showed the presence of ambient fluid alters the wettability of substrate changing the timescale for spreading process.

Increase of viscosity of either phase showed a decrease trend in the advancing critical velocity V_{C}. Again, we show this variation follows the scaling $V_{\mathrm{C}} \sim \chi^{-1}$ by fixing the droplet phase. We also propose an effective viscosity η_{12} for the two-phase system to obtain the critical velocity V_{C}. To summarize, in this chapter, we showed the relative influence of the viscosity of both phases on the spreading process.

3. Droplet formation and stability of thin film

Microfluidic devices provide a useful platform for generation of monodisperse droplets by controlling the flow rates. The formation of high viscosity droplets in less viscous external phase has been experimentally studied for a range of viscosity ratios and interfacial tensions [58]. In this chapter, we focus on the influence of the carrier fluid viscosity on the formation of the less viscous droplets. The droplet phase is chosen to be water while the viscosity of the external phase (PDMS oil) is varied over four decades. Combination of water and silicone oil makes a partially wetting system and the dynamics of contact line plays an important role in droplet generation. The hysteretic system shows two modes of formation namely dripping and rivulet. A scaling for droplet size *d* for each regime is developed based on the injection flow rates. We also discuss the stability and thickness of the thin film and how it affects the size of the droplet.

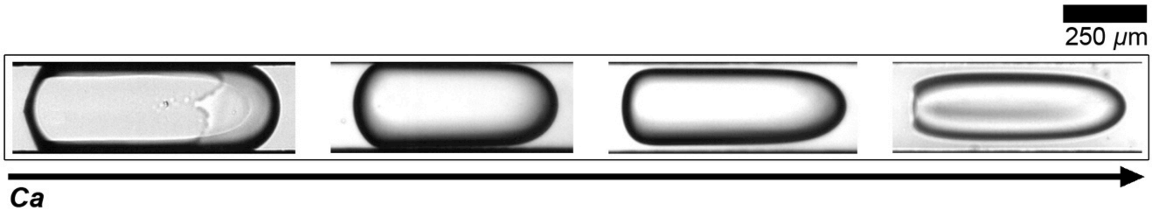

Figure 3.1 Different droplet configurations with increasing capillary number

3.1. Scaling law for film thickness in a circular capillary

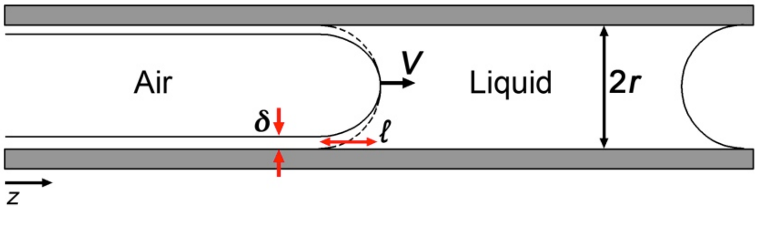

Figure 3.2 Schematic of bubble motion through a circular capillary of radius r initially filled with a liquid. A liquid film of thickness δ is formed on the capillary walls. Dotted line indicates static meniscus [164].

Here we briefly revisit the classical problem proposed by Bretherton [165] in which a circular capillary of radius r initially filled with a wetting liquid of viscosity η is displaced by a bubble of velocity V. The static meniscus indicated by dotted line in Figure 3.2 is hemispherical and it is deformed during motion opposed by surface tension γ. In the limit of low Reynolds number inertia is negligible and parameter to be considered is the capillary number Ca. The passing air bubble forms a thin film of thickness $\delta \ll r$. and lubrication approximation can be used to calculate the viscous dissipation inside the film as $\eta V/\delta^2$. Equating with capillary force given by the gradient of Laplace pressure ($\Delta p/\ell = \gamma/\ell r$) within the meniscus of length ℓ [164, 165],

$$\frac{\eta V}{\delta^2} \sim \frac{\gamma}{\ell r} \tag{3.1}$$

where ℓ is calculated by matching curvature of static and dynamic meniscus. The profile of the film where dynamic meniscus joins the static meniscus varies as $\delta(z)$ and the curvature is given by second derivative as δ/ℓ^2. The dynamic and static meniscus are matched by equating the Laplace pressures [164, 165],

$$-\frac{\gamma}{r} - \frac{\gamma\delta}{\ell^2} \sim -\frac{2\gamma}{r} \tag{3.2}$$

giving $\ell \sim (\delta r)^{1/2}$. From the above two equations the Bretherton's law can be deduced as [164, 165],

$$\frac{\delta}{r} \sim Ca^{2/3} \tag{3.3}$$

With increasing capillary number Ca film thickness δ plateaus and r is replaced with $(r - \delta)$ in equations (3.1) and (3.2) to get the modified law as [164],

$$\frac{\delta}{r} \sim \frac{Ca^{2/3}}{1 + Ca^{2/3}} \tag{3.4}$$

3.2. Numerical investigation of droplet formation.

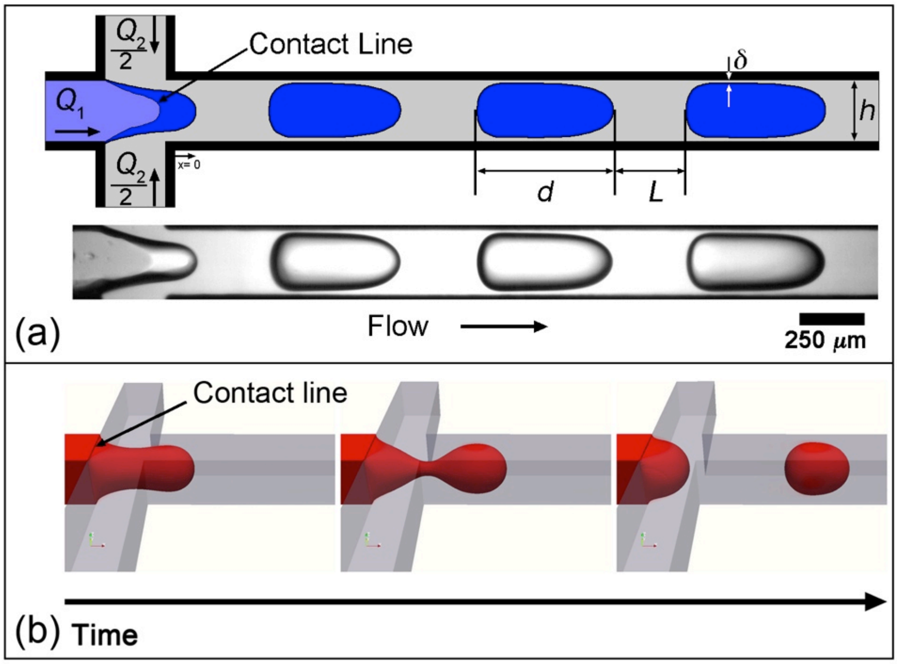

Figure 3.3 (a) Schematic of the microfluidic platform with droplet formation in dripping regime. The experimental micrograph is shown below. α_2 = 0.48. Fluid Pair: W-500cS. Droplet phase: $L1$ (Blue), External phase: $L2$ (Gray). Film thickness is given by δ and the droplet diameter by d. (b) Numerical simulation of droplet break-up at the hydrodynamic focusing section.

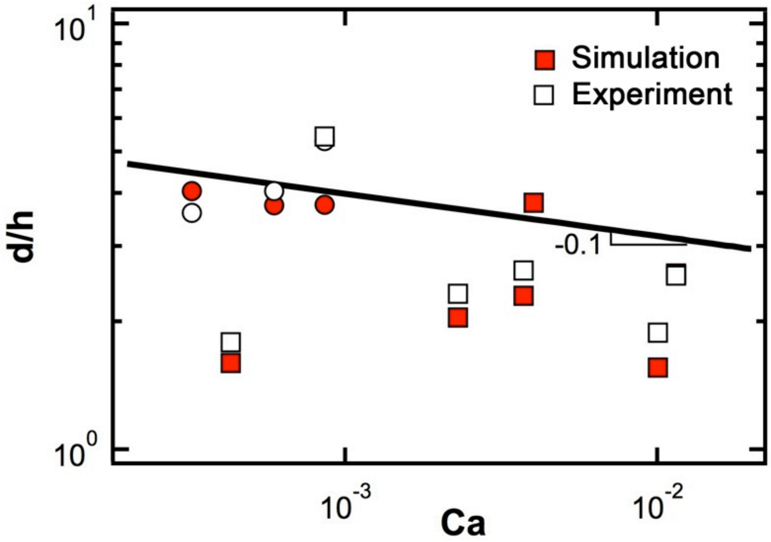

Figure 3.4 Comparison of experiment with numerical simulation. Droplet size d/h is plotted with capillary number Ca.

A preliminary study is conducted on the formation of droplet at hydrodynamic focusing section with *OpenFOAM*[166], an open source CFD package using an incompressible isothermal model. Continuity and momentum equations are solved along with a species transport equation and interface of the two immiscible fluids is captured using volume of fluid (VOF) method [167]. In the VOF method, the relative phase fraction is computed by solving the species transport equation and the movement of the interface is tracked based on the distribution of the relative phase fraction.

We noticed a difference in the droplet size when experiments were compared with simulation. In the numerical simulation, the droplet phase is set to fully wet the central inlet channel while the external phase wets the rest of the channel. Droplet and external phase meet at the focusing section where the droplet is pinched-off. In the simulation, contact line is aligned parallel to the side inlets while in experiments, the contact line extends past the inlet into the focusing section. Since the evolution of the contact line follows the history of the system in an experimental system, it cannot be predicted beforehand. However, it is not clear that prior knowledge about the contact line and its lack of inclusion in the simulation is the reason for this difference. Overall, the preliminary study supports our conclusion on the relevance of contact line and its influence on the droplet formation.

3.3. Experimental setup and the microfluidic platform

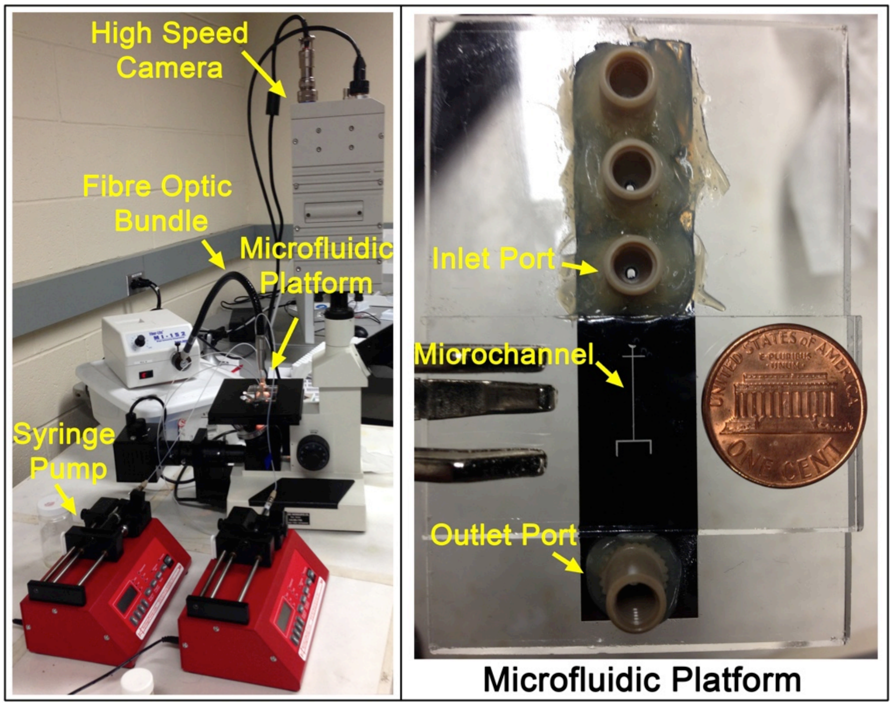

Figure 3.5 Photograph of the experimental setup and the microfluidic platform.

The microfluidic platform consists of a hard non-deformable microchannel used to continuously generate water droplets in silicone oil at externally imposed velocities. The microchannels are fabricated using double-side-polished silicon pieces that are etched through their entire thickness $h = 250\ \mu\text{m}$ using deep reactive ion etching and then sandwiched between two borosilicate glass slides using anodic bonding. The microfluidic platform comprises a fluid focusing section made of two channels intersecting at right angles to generate droplets and an outlet observation channel to examine multiphase flows morphology and dynamics [Figure 3.3]. To visualize the microflows, the microfluidic module is placed on top of an inverted microscope equipped with high-speed camera (*Redlake, HG-100K*) and a fiber optic bundle connected to a 150 W halogen bulb is located about 10 cm above the microchannel to provide illumination [Figure 3.5]. Fluids are injected into the device using gas-tight syringes mounted into high-pressure syringe pumps to manipulate the flow rates of both phases.

The channel cross-section is chosen to be square with a width h, to reduce the influence of many length scales on droplet formation. The droplet phase $L1$, having viscosity η_1, is introduced through the central inlet channel at flow rate Q_1 and the continuous phase $L2$ of viscosity η_2 is symmetrically injected from the side-channels with a total flow rate Q_2. Flow rates for Q_1 typically span between 1 and 200 μL/min and from 1 to 400 μL/min for Q_2. The flow rate ratio $\varphi = Q_1/Q_2$ ranges between 10^{-2} and 10^{1}. For each fluid pair, this method allows us to produce droplets with a wide range of sizes d and velocities V. The film thickness δ around the droplet is measured at the point of minimum thickness. The length of the droplet is measured as d and the spacing between two successive droplets as L.

3.4. Fluid properties

Fluid Pair	γ_{12} (mN m^{-1})	χ	θ_{Am} (Degrees)	Symbol
W-1cS	40.7	1.2	65	○
W-5cS	42.7	2.2×10^{-1}	66	□
W-20cS	42.7	5.3×10^{-2}	89	△
W-50cS	42.7	2.1×10^{-2}	91	▽
W-100cS	42.7	1.0×10^{-2}	105	◁
W-200cS	42.7	5.2×10^{-3}	113	▷
W-500cS	42.7	2.1×10^{-3}	137	✧
W-1000cS	42.7	1.0×10^{-3}	158	◊
W-10000cS	42.7	1.0×10^{-4}	180	◇

Table 3-1 Properties of the fluid pairs water and silicone oils, where γ_{12} (±1 mN/m) is the interfacial tension, $\chi = \eta_1/\eta_2$ is the viscosity ratio, and $\theta_{Am} = \theta(V)$ is the measured dynamic advancing contact angle for the velocity $V = 250$ μm/s.

The properties of the fluid pairs investigated in this study are displayed in Table 3-1. The droplet phase $L1$ is composed of pure water (*Sigma-Aldrich*) and the external phase $L2$ is made of conventional polydimethylsiloxane oils, *i.e.*, PDMS or silicone oil (*Gelest*), of different viscosities. Parameters of interest include the dynamic viscosity ratio $\chi = \eta_1/\eta_2$ and the fluid pair interfacial tension γ_{12}. Typical values of interfacial tension γ_{12} are found to plateau around 42 mN/m. The kinematic viscosity of $L2$ is varied over four decades (from 1 to 10^4 cS) and the viscosity of the droplet phase $L1$ remains constant. From low to high viscosity, the specific gravity of silicone oils slightly varies from 0.812 to 0.974. Typical values of the minimum advancing contact angle θ_{Am} based on the slowest injection velocity of $L1$ into the microchannel $V = Q_1/h^2 \sim 250$ μm/s are measured using the goniometer apparatus and are reported in Table 3-1. Data show that θ_{Am} depends on the viscosity of the external phase with an effective dynamic transition from partially wetting droplets to partially non-wetting droplets that occurs for fluid pairs W-20cS and W-50cS.

3.5. Evolution and stability of thin film

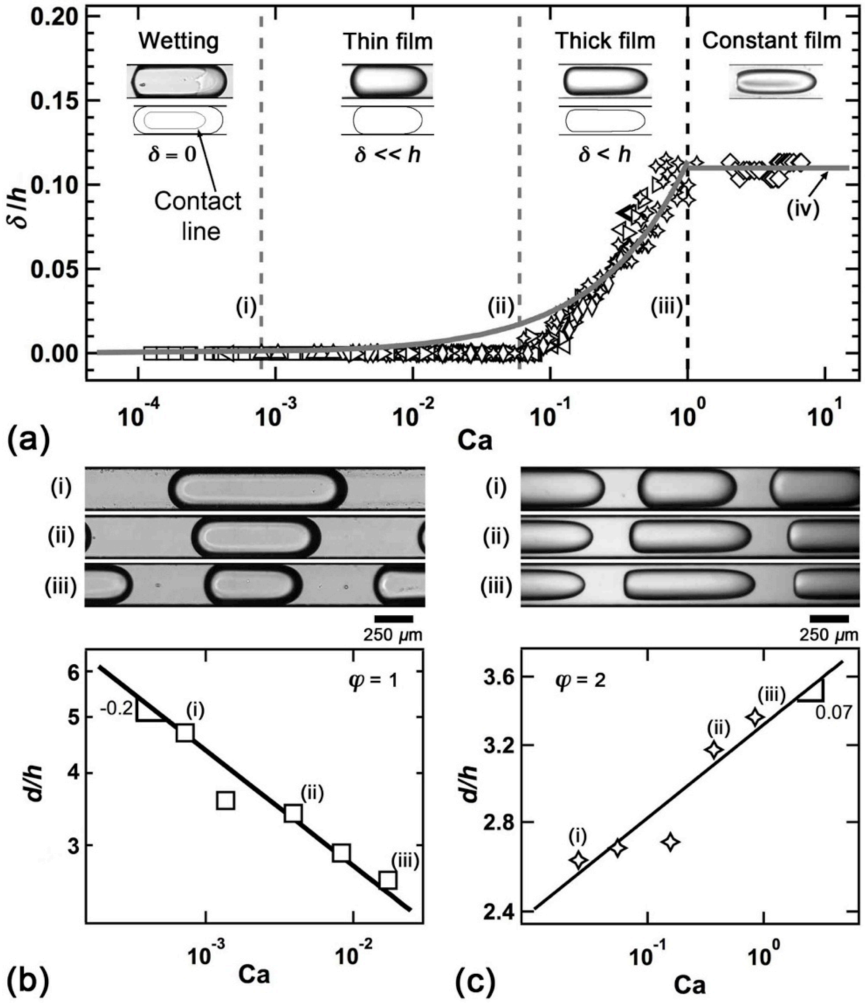

Figure 3.6 Evolution of film thickness with capillary number. (a) Film thickness normalized with the channel width δ/h as a function of capillary number Ca. Solid line: $\delta/h = \Omega Ca^{2/3}$, with a cut-off at $\delta/h = 0.11$ and $\Omega = 0.11$. (b) Droplet size decreases with capillary number in the wetting and thin film region where the film thickness is negligible, solid line: $d/h = 1.1Ca^{-0.2}$. (c) Droplet length increases due to the increase of film thickness in the thick film region, solid line: $d/h = 3.3Ca^{0.07}$. $\varphi = Q_1/Q_2$.

A variety of multiphase flow regimes are observed as the capillary number $Ca = \eta_2 V/\gamma_{12}$, where V is the droplet velocity, ranges from 10^{-4} to 10^{1} due to the stability and shape of the lubricating film between droplets and the walls. The evolution of the thickness of the wetting layer is denoted with δ and plotted as a function of the capillary number Ca. Film thickness permits the classification of the different regimes as (*i*) Wetting (*ii*) Thin Film (*iii*) Thick Film and (*iv*) Constant Film [Figure 3.6(a)]. For very low

Ca, hydrodynamic forces are negligible compared to surface tension forces and the system adopts a wetting state where droplets make direct contact with the confining walls, which is experimentally visible due to the presence of contact lines. When the capillary number $Ca > 10^{-3}$, the film becomes thicker and dynamically more stable to the formation of dewetting patches. As a result, lubricated droplets are more steadily produced. In the thin film regime, the droplet size exhibits a relatively weak dependency on the capillary number *Ca*. This effect can be seen when fixing a constant flow rate ratio $\varphi \sim Q_1/Q_2$ while increasing the absolute flow velocity $J \sim (Q_1+Q_2)$. In this regime, measurements suggest that for fixed flow rate ratio φ, the droplet size d varies with the capillary number *Ca* according to $d/h \sim Ca^a$, with $a = -0.2$ [Figure 3.6(b)]. As viscous effects become more prominent when *Ca* increases, smaller droplets are produced in the thin film regime. We define the thick film regime when $Ca > 10^{-1}$ as optical measurements of δ allow for directly examining its evolution [Figure 3.6(a)*iii*]. Although the film thickness is not uniform in a square microchannel, the minimum film thickness scales as $\delta/h \sim Ca^{2/3}$ until *Ca* reaches unity and a constant film thickness $\delta/h \sim 0.11$ is observed [Figure 3.6(a)*iv*] beyond $Ca \sim 1$. In contrast to the thin film regime, in thick film regime, the film thickness δ is significant and the droplet size d slightly increases with *Ca*. Indeed, at fixed φ, the droplet size grows with the capillary number as $d/h \sim Ca^{0.07}$ [Figure 3.6(c)]. This very minor variation in the droplet size can be attributed to the additional confinement of the droplets due to the lubricating continuous phase at the walls. The evolution of the thin film plays a significant role in controlling the droplet length in microchannels.

3.6. Modes of droplet formation

Droplet size is determined at the focusing section where the droplet phase is pinched off by the external phase. An important feature of the partially wetting systems is their hysteretic nature and the existence of two modes of droplet production for similar injection conditions. In the first mode, droplets are produced at the fluid junction which is referred to as dripping regime [Figure 3.3]. The second mode of droplet generation is called rivulet regime, where droplets are emitted from the tip of a wetting tongue that is aligned parallel to the flow direction [Figure 3.8].

3.6.1. Dripping regime

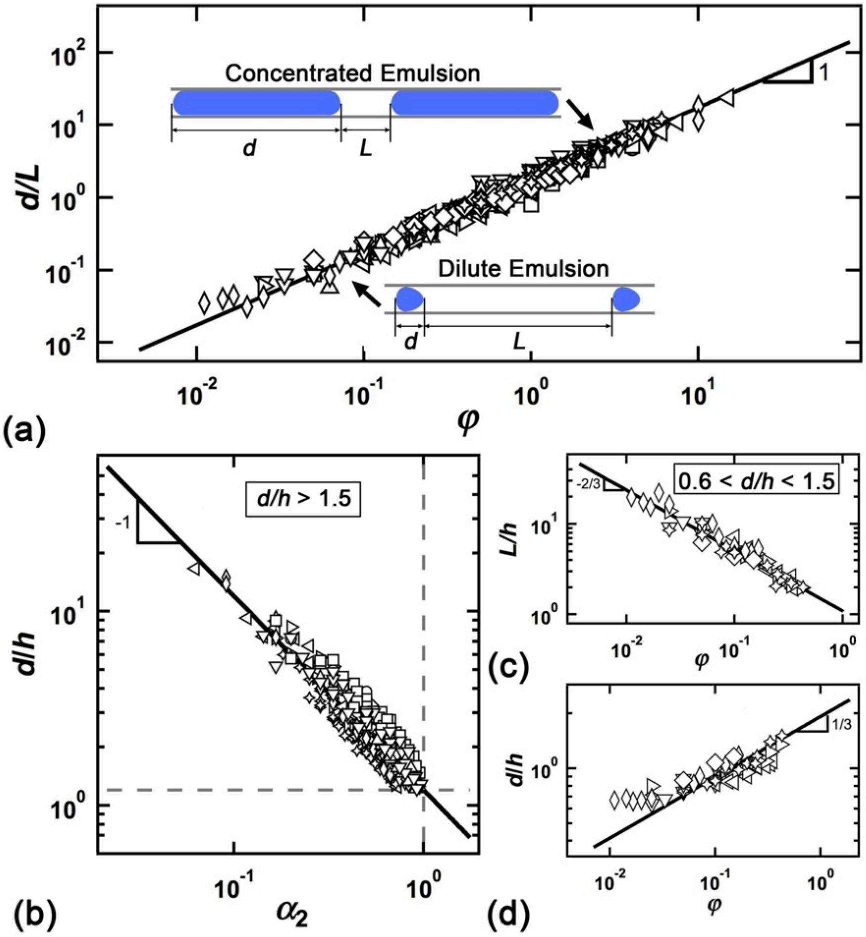

Figure 3.7 Dripping regime. (a) Evolution of the multiphase flow linear aspect ratio d/L as a function of flow rate ratio φ, solid line: $d/L = 1.75\varphi$. (b) Concentrated regime ($d/h > 1.5$), droplet length d/h vs. liquid fraction α_2. Solid line: $d/h = 1.2\alpha_2^{-1}$ (c) Droplet spacing L/h as a function of flow rate ratio φ in the dilute regime ($d/h < 1.5$), solid line: $d/h = 1.1\varphi^{-2/3}$. (d) Droplet length d/h plotted with the flow ratio φ for small droplets. Solid line: $d/h = 1.9\varphi^{1/3}$.

An important feature of segmented microflows in dripping regime, is the conservation of the linear aspect ratio d/L of the multiphase flow, which is found to be directly proportional to the flow rate ratio according to $d/L = c\varphi$, with $c = 1.75$ for capillary numbers Ca ranging between 10^{-4} and 10^{1} [Figure 3.7(a)]. This property results from mass conservation applied to a linear unit cell of the flow over a period of droplet emission since the scalings $d \sim Q_1/h^2$ and $L \sim Q_2/h^2$ suggest direct proportionality of d/L with φ in the limit of elongated droplets $d/h > 1.5$. Data show that this relationship can also be extended to the small droplets when $d/h < 1.5$. The influence of droplet size d with Ca does not significantly alter the value of the aspect ratio d/L since in the thin film regime, L decreases with d [Figure 3.6(b)], and in the thick film regime, L increases with d [Figure 3.6(c)].

In the elongated droplet regime, the normalized droplet size d/h can also be relatively well predicted independently of Ca. Indeed, similar to previous work on the generation of microbubbles [168], the droplet length can be approximated with $d \sim J \times T_2$ where $J = (Q_1+Q_2)/h^2$ is the superficial flow velocity and $T_2 = (h^3/Q_2)$ is the flow rate-controlled pinching time for breakup. Hence, neglecting the apparent slip velocity between droplet and external phase as well as the weak influence of Ca, the droplet length is expected to be inversely proportional to the continuous phase liquid fraction $\alpha_2 = Q_2/(Q_1+Q_2)$, such as $d/h \sim 1/\alpha_2$. The volumetric fraction α_2 is also a useful parameter for quantifying the droplet concentration in segmented flows. Here, the concentrated regime corresponds to a low external phase liquid fraction, $\alpha_2 < 0.8$, and a wide range of elongated droplet sizes can be produced while the droplet spacing remains nearly constant $L \sim h$. By contrast, in the dilute regime ($\alpha_2 > 0.8$), the droplet size remains almost constant $d \sim h$ while the spacing between droplets strongly varies.

In the concentrated regime [Figure 3.7(b)], data shows that the measured droplet size is inversely proportional to the volumetric volume fraction according to,

$$\frac{d}{h} = 1.2\alpha_2^{-1} \qquad \text{for} \quad \frac{d}{h} > 1.5 \qquad (3.5)$$

The relative scatter in the data is attributed to the influence of the capillary number Ca on d. In particular, for viscosity ratio $\chi \sim 1$, the previous scaling yields good agreement with experiments when $Ca > 1.2 \times 10^{-3}$, *i.e.*, in the non-wetting regime. In the wetting regime at very low capillary number, Eq. 1. underestimates the droplet size d/h and previous arguments based on a flow rate-controlled pinching time with no apparent slip between phases do not apply due to the presence of wetting contact lines which alter droplet's velocity. Besides data scatter, the previous scaling appears consistent given the very wide range of external phase viscosity η_2 explored and the large span of Ca between 10^{-3} and 10^{1}.

The dilute droplet regime is characterized with the emission of small droplets with a fairly narrow size distribution ($0.6 < d/h < 1.5$) while the droplet spacing L varies over a decade. Experimentally, most of our data are produced in the thick film regime. As the droplet spacing L shows a large variation, we measure the size of the liquid plugs of $L2$ between droplets and empirically find a simple scaling such as $L/h \sim \varphi^{-2/3}$ [Figure 3.7(c)]. Since the linear aspect ratio in the dripping regime is conserved and follows $d/L \sim \varphi$, we obtain the following scaling

$$\frac{d}{h} = 1.9\varphi^{1/3} \qquad \text{for} \quad \frac{d}{h} < 1.5 \qquad (3.6)$$

for the droplet size in the dilute dripping regime, which is associated with small droplets sizes [Figure 3.7(d)].

3.6.2. Rivulet regime

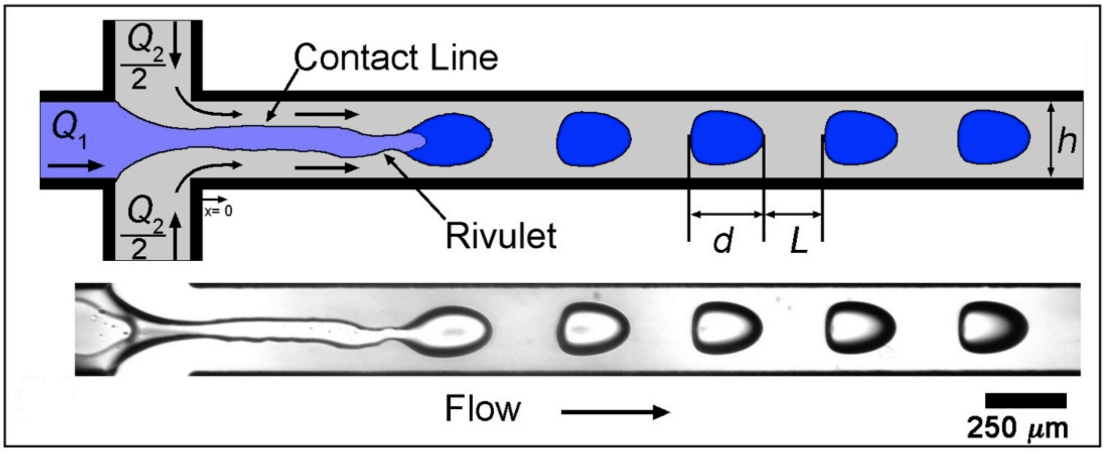

Figure 3.8 Schematic of droplet formation in the rivulet regime. Droplets are emitted from the tip of a wetting tongue extending past the focusing section. $\alpha_2 = 0.77$. Fluid Pair: W-500cS.

The wetting condition of the droplets can lead to hysteretic behavior and, depending on the history of the system a second mode of droplet generation is observed namely rivulet. In the rivulet regime, a wetting tongue of liquid $L1$ can spread on the glass wall past the focusing section and form a rivulet that regularly emits droplets in the outlet channel [Figure 3.8]. Once established, the rivulet displays pinned contact lines that are aligned parallel to the flow direction with a static contact angle $\theta < \pi/2$. In this interfacial arrangement, the flow velocity component normal to the contact line is null and the contact angle θ along the rivulet is set independent of flow capillary number *Ca*. Progressively increasing the side flow rate Q_2 typically causes the wetting tongue to grow further into the microchannel while imposing a sharp variation in Q_2 can revert the system back to the dripping regime.

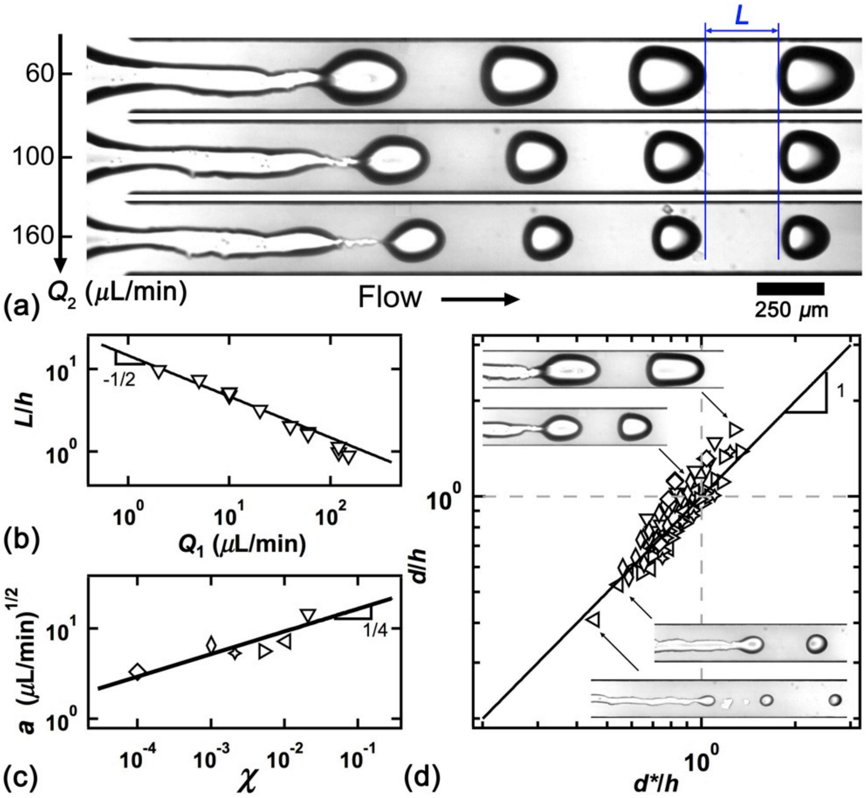

Figure 3.9 Rivulet regime. (a) Micrograph showing droplet generation from a rivulet for fixed $Q_1 = 30$ μL/min, fluid pair: W-200cS. The spacing between the droplets L remains constant while Q_2 increases. (b) Evolution of droplet spacing L/h as a function of Q_1 for fluid pair: W-50cS. Solid line: $L/h = aQ_1^{-1/2}$. (c) Evolution of coefficient a with the viscosity ratio χ, solid line: $a = b\chi^{1/4}$. (d) Experimental droplet size d/h as a function of calculated droplet size d^*/h, solid line: $d/h = d^*/h$. Inset: example of rivulet-generated droplets

In the rivulet regime, the relationships for *d* and *L* significantly differ from the dripping regime. In particular, we experimentally find that the average distance between droplets *L* is directly set with the dispersed phase flow rate Q_1. Figure 3.9a shows the examples of flows where Q_1 is fixed and Q_2 varies. Monodisperse droplets of various sizes *d* can be produced at a constant interval *L*. To better understand this phenomenon, the spacing L/h is measured from micrographs and found to scale with the flow rate of the droplet phase Q_1 according to $L/h = aQ_1^{-1/2}$, where the coefficient *a* depends on the particular fluid pair used [Figure 3.9(b)]. We apply this method to all fluid pairs and empirically deduce the scaling for the coefficient *a* as a function of the viscosity ratio χ such as $a = b\chi^{1/4}$, with the constant $b = 29.3$ (μL/min)$^{-1/2}$ [Figure 3.9(c)].

We make use of the constant droplet spacing *L* to express the scaling for the droplet size *d* in the rivulet regime. As the droplet size is smaller than the channel height *h*, it adopts a nearly spherical shape at low *Ca* and a bullet shape at high *Ca*. Modeling droplets as spheres during a period of emission gives $(\pi/6)d^3 \sim Q_1$ and using $L \sim Q_2/h^2$ in conjunction with a mass conservation argument leads to $\pi d^3/(6Lh^2) \sim \varphi$. Substituting *L* with our previous scaling yields a semi-empirical expression for the droplet size d^* in the rivulet regime,

$$\frac{d^*}{h} = \left(b \frac{6}{\pi} \chi^{1/4} Q_1^{1/2} Q_2^{-1} \right)^{1/3} . \qquad (3.7)$$

The measured droplet size d/h is found to be in good agreement with the proposed scaling d^*/h [Figure 3.9(d)]. The bistability observed between the dripping and rivulet production regime is strongly related to local wetting properties of the channel and regime transitions can be triggered with random sessile wetting patches of *L*1 left at the channel walls.

3.7. Conclusion

The evolution of the thin film in square capillaries can be seen as a function of the capillary number as $Ca \sim \delta^{2/3}$ for a wide range of Ca from 10^{-4} and 10^{-2}. The film thickness allows the classification of different regimes as (*i*) Wetting (*ii*) Thin film (*iii*) Thick Film and (*iv*) Constant film. The film thickness plateaus around $\delta/h \approx 0.11$ for elongated droplets when $Ca > 1$ in the constant film region. We show that there is a contrasting dependence on the droplet size d in different film thickness regimes. For a fixed flow ratio φ in the thin film region, the droplet size d decreases with the Ca while the droplet size increases in the thick film region due the additional confinement of the evolving film thickness. In spite of the change in the droplet size, the linear aspect ratio d/L of the multiphase flow remained constant and scales with the flow ratio $d/L \sim \varphi$. In the dripping regime, neglecting the contrasting trend of Ca, the droplet length d/h is inversely proportional to the liquid fraction as $d/h \sim 1/\alpha_2$. For small droplets ($0.6 < d/h < 1.5$) in the dilute regime, the spacing varies as $L/h \sim \varphi^{-2/3}$ while the droplet size scales as $d/h \sim \varphi^{1/3}$. We report a second mode of droplet production called Rivulet in which monodisperse droplets periodically ejected from the tip of a pinned rivulet. Experiments show that spacing between droplets is set by the flow rate of the droplet phase Q_1 and a semi-empirical relation for the droplet size is given in equation (3.7).

4. Partially wetting droplets in square microchannel

In this chapter we discuss the evolution of the partially wetting droplets in the square channel based on the natural spreading properties of the fluids. Downstream from the focusing section, the droplets translating in the square channel shows a variety of wetting transitions. These wetting transitions are essentially controlled by the size of the droplet *d*, the velocity of the droplet *V* and natural spreading property of the fluid pair V_C. Typical forced wetting transitions in the microchannel are characterized with phase diagrams and the influence of wetting/non-wetting regimes on the relative droplet velocity is examined as a function of a wetting parameter *d*/(*hCa*). We also discuss the formation of corner droplets where the droplet morphology adapts to minimize the dewetting velocity.

4.1. Dynamic wetting transition

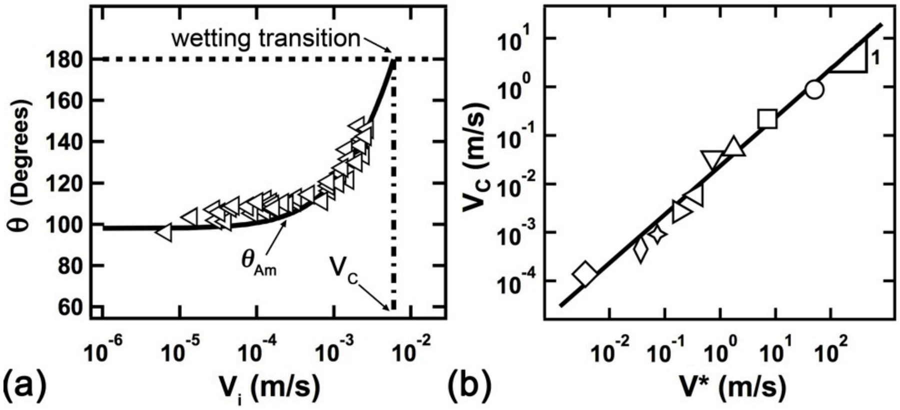

Figure 4.1 (a) Evolution of advancing contact angle as a function of velocity for fluid pair: W-100cS. Solid Line: $\theta = (\theta_0^3 + \omega V_i)^{1/3}$ with $\omega = 8.2 \times 10^8$ and $\theta_0 = 98^\circ$. Dashed Line: $\theta = 180^\circ$. Dash-dot line: Advancing critical velocity $V_i = V_C$ at which contact angle is expected to reach 180˚. (b) Advancing critical velocity V_C as a function of capillary velocity $V^* = \gamma_{12}/\eta_2$ for the fluids in Table 3-1. Solid line: $V_C = Ca_c V^*$, with $Ca_c = 2.4 \times 10^{-2}$.

A short recap on the dynamic wetting properties mentioned in Chapter 2 shows that, dynamic contact angle θ for a two-fluid system increases with contact line velocity V_i to reach a limiting value at 180˚. This velocity is named the advancing critical velocity V_C representing a wetting transition beyond this point [Figure 4.1(a)]. Advancing critical velocity V_C is calculated for all the fluid pairs mentioned in Table 3-1 and compared with the capillary velocity $V^* = \gamma_{12}/\eta_2$. Since all droplets are made of pure water, the capillary velocity is calculated based on the viscosity of the external phase η_2. For over four decades of varying the viscosity for the external phase, data suggest a simple relationship $V_C = Ca_c.V^*$ with the critical capillary number $Ca_c = 2.4 \times 10^{-2}$ [Figure 4.1(b)]. The constant is labeled as the critical capillary number $Ca_c = V_C/V^*$. Since the interfacial tension for the fluid pairs are of similar magnitude, the critical velocity V_C scales with the viscosity of the external phase as $V_C \sim 1/\eta_2$. Using the critical velocity V_C and capillary number Ca_c we classify the forced wetting transitions of droplet inside microchannel.

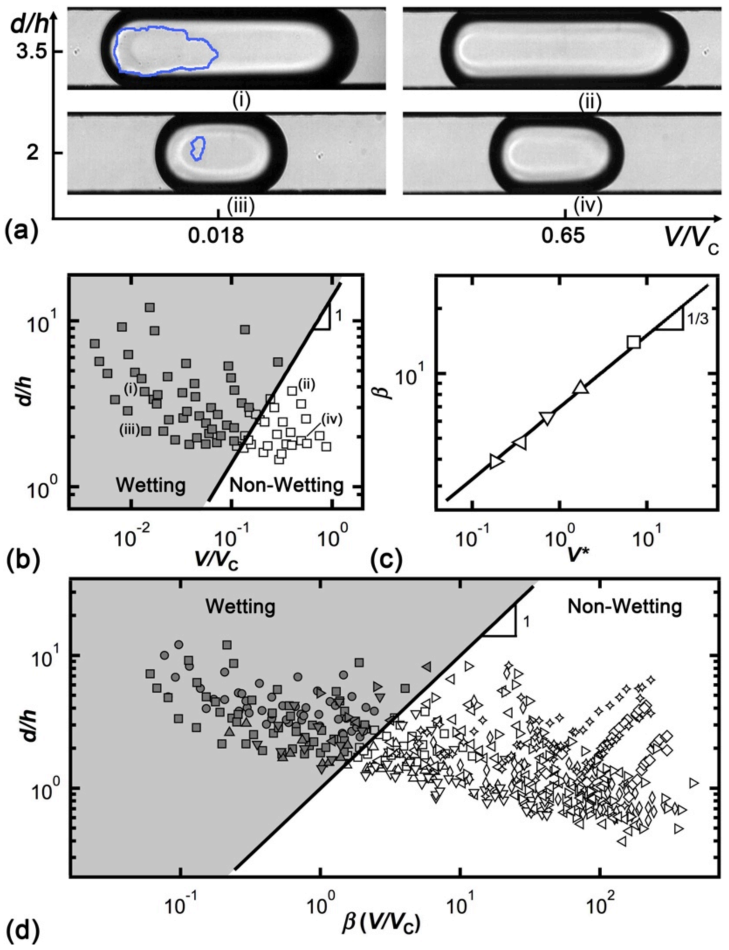

Figure 4.2 (a) Experimental micrographs depicting the transition from the wetting to the non-wetting flow regime, contact lines accented (in blue) for visibility, fluid pair: W-5cS. (b) Normalized droplet length d/h vs. rescaled droplet velocity V/V_C, solid line: $d/h = \beta(V/V_C)$ with $\beta = 14$, fluid pair: W-5cS. (d) Evolution of coefficient β with capillary velocity V^*, solid line: $\beta = \zeta\, V^{*1/3}$. (d) Combined wetting phase diagram showing normalized droplet length d/h as a function of $\beta(V/V_C)$ for all fluid pairs in Table 3-1. Filled symbols: wetting droplets, open symbols: non-wetting droplets.

Inside the microchannel, the dynamic wetting characteristics of multiphase flow depend on the droplet velocity V and size d of droplets for a given fluid pair [Figure 4.2(a)]. The criterion for the wetting transition of translating droplets can be determined by comparing the droplet convective timescale $\tau \sim d/V$ with the typical dewetting timescale of the local film based on fluid properties and channel geometry $\tau_D \sim h/V_D$, where V_D is the dewetting velocity. Incidentally, the droplet convective timescale also corresponds to the lifetime of the quasi-static thin film produced by the passage of the droplet at a specific location in the channel. A simple hypothesis for the stability of the thin film associated with a fast lubricated droplet is $\tau \ll \tau_D$. By contrast, unstable thin films are obtained for slow moving droplets with large convective timescales such as $\tau \gg \tau_D$. Balancing timescales and rearranging terms yield an estimate for the wetting transition of microfluidic droplets such as $d/h \sim V/V_D$. For liquid-air system, Redon *et al* [169] showed that the dewetting velocity V_D of a metastable thin film deposited on a substrate is independent of the film thickness δ and scales as $V_D = V^*k\theta_E^3$, where k depends on the nature and on the molecular weight of the liquid.

To test our hypothesis for the droplet wetting transition in microchannels, we inspect flow morphology and map regions of wetting and lubricated droplets on a phase-diagram where d/h is plotted against $V/V_C = Ca/Ca_c$, for a given fluid pair [Figure 4.2(b)]. The previous argument yields good agreement with experimental observations as the function $d/h = \beta(V/V_C)$, where the coefficient $\beta = 14$ (for W-5cS), delineates the two regimes. Given the range of fluid properties and flow parameters investigated, the wetting/non-wetting transition is observed for the five fluid pairs ranging between W-5cS and W-200cS. Since the coefficient $\beta \sim (Ca_c/k\theta_E^3)$ is expected to depend on fluid properties, we plot β as a function of the capillary velocity V^* which is the only variable across the different fluid pairs in Table 3-1. From the experimental data obtained for the different fluid pairs with wetting/non-wetting transition, we found that $\beta = \zeta V^{*1/3}$ with $\zeta = 6.98\ (\mathrm{m/s})^{-1/3}$ [Figure 4.2(c)]. This functional relationship is used to extrapolate the values of β for other fluid pairs and produce a master phase-diagram [Figure 4.2(d)] where the line $d/h = \beta(V/V_C)$ clearly separates wetting and non-wetting regimes for all fluid pairs given in Table 3-1. Hence, the functional relationship

$$\frac{d}{h} = \zeta V^{*1/3}\left(\frac{V}{V_C}\right) \tag{4.1}$$

describes the transition between wetting and non-wetting regimes for all cases examined. This equation suggests a critical value for the ratio $d/(hCa)$ based on the fluid properties of each fluid pair according to $d_{\mathrm{critical}}/(hCa) = (\zeta V^{*1/3})/Ca_c$. In the diagram, a droplet with the ratio $d/(hCa) > (\zeta V^{*1/3})/Ca_c$ belongs to wetting regime. This shows in particular that, similar to the detachment of wetting bubbles between two parallel plates [170], the droplet wetting transition inside the square capillary can be adjusted with the parameter $d/(hCa)$.

4.2. Droplet velocity in square microchannel

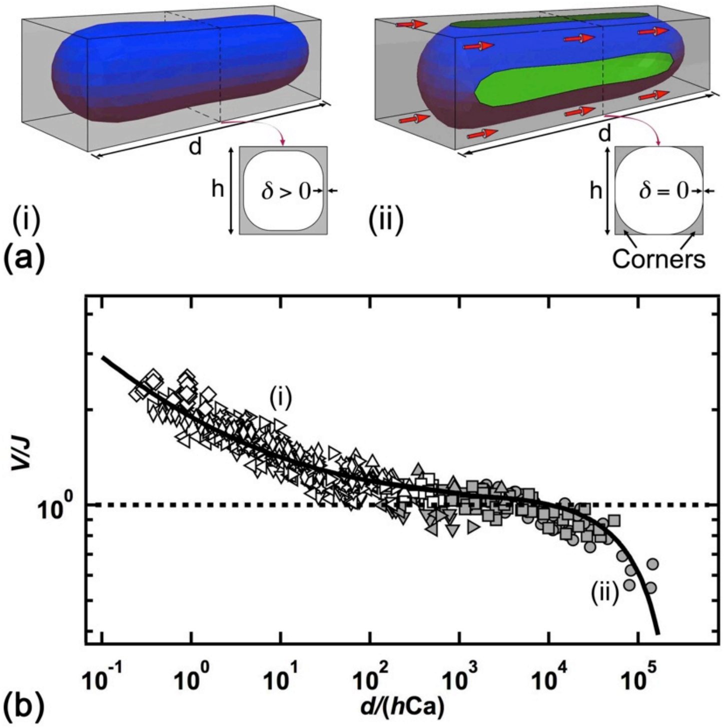

Figure 4.3 Droplet velocity. (a) Schematic of elongated droplet in a square channel. (*i*) Fitted piston. (*ii*) Leaky piston with contact line. Green shading shows the droplet wetted area. (b) Normalized droplet length d/h and capillary number Ca. Open symbols: Non-wetting droplets. Filled Symbols: Wetting droplets. Solid line: $V/J = 1 + (d/(hCa))^c$. Dotted line: $V/J = 1$.

The microfluidic system allows the examination of the droplet velocity V as function of size d and capillary number Ca in wetting and lubricating flow regimes. The lubricating thin film has different effects on velocity in circular and square microchannels. In circular capillaries, an elongated droplet typically behaves as a tight-fitted piston and move at about the same speed as the superficial velocity J and is referred to as ‘*plug flow*’. A major difference in a square channel is the presence of sharp corners and non-uniform film thickness [171]. In square channel, a typical droplet does not fill the whole channel cross-section and the droplet behaves as a leaky piston with the presence of a '*corner flow*'[172, 173]. The extent of the flow of the continuous phase through the corners determines the relative droplet velocity V/J [174, 175]. As the capillary number Ca increases, the droplet behavior changes from a leaky piston in the wetting regime to a tight fitted piston in the large film thickness δ regimes [Figure 4.3(a)].

As the wetting transition is essentially controlled with $d/(hCa)$, this parameter is used to rescale the droplet velocity ratio V/J for all regimes [Figure 4.3(b)]. The relative velocity V/J depends on the flux of the continuous phase $L20$ through the four corners in the square channel. The corner flux Q_C is proportional to the difference between droplet velocity V and the superficial velocity J as $Q_C \sim (V - J)S$, where S is the cross-sectional area of the corners excluding the droplet. In the analysis of long bubbles in polygonal capillaries, Wong *et al*. [176, 177] calculated the bubble profile with negligible viscosity and developed an expression for the dependency of corner flux on the capillary number and the bubble length as $Q_C \sim (hCa^{-1/3}/d)$. In our case with droplets of non-negligible viscosity, we find that expressing the corner flux as $Q_C \sim (d/hCa)^c$ would allow the rescaling of all data points to a single curve for the range of capillary numbers explored [Figure 4.3(b)]. Equating the expressions for Q_C, the ratio of droplet velocity to the superficial velocity can be written as,

$$\frac{V}{J} = 1 + \xi \left(\frac{d}{hCa} \right)^c \tag{4.2}$$

where the coefficients ξ and c depend on the droplet wetting condition and are given in Table 4-1.

Regime	ξ	c
Non-wetting Droplet	$+9.0\times10^{-1}$	$-1/3$
Wetting Droplet	-8.5×10^{-5}	$+3/4$

Table 4-1 Fitting parameters for equation (4.2)

For a given capillary number *Ca*, Equation (4.2) suggests that, the relative velocity V/J is inversely correlated with the droplet length d, *i.e.* long droplets move slower. Similarly, when the droplet length d is fixed, the relative velocity increases with the capillary number *Ca*. For wetting droplets, the direct contact between droplets and the channel walls introduces viscous friction and translating droplets adopt a stick-and-slip behavior and appear as 'reluctant' to move while amounts of the continuous phase bypasses them through corner flows. This behavior is more pronounced in the limit of large $d/(hCa) \gg 1$, where the relative droplet velocity $V/J < 1$. There is a transition region for $d/(hCa)$ in the range of $10^2 \sim 10^3$ where wetting and non-wetting droplets co-exist and the relative velocity is close to unity, $V/J \approx 1$. The coexistence of these two regimes is due to the difference in the wetting criterion given by critical ratio $d_{\mathrm{critical}}/(hCa)$ for different fluid pairs.

4.3. Wetting effects in square microchannels

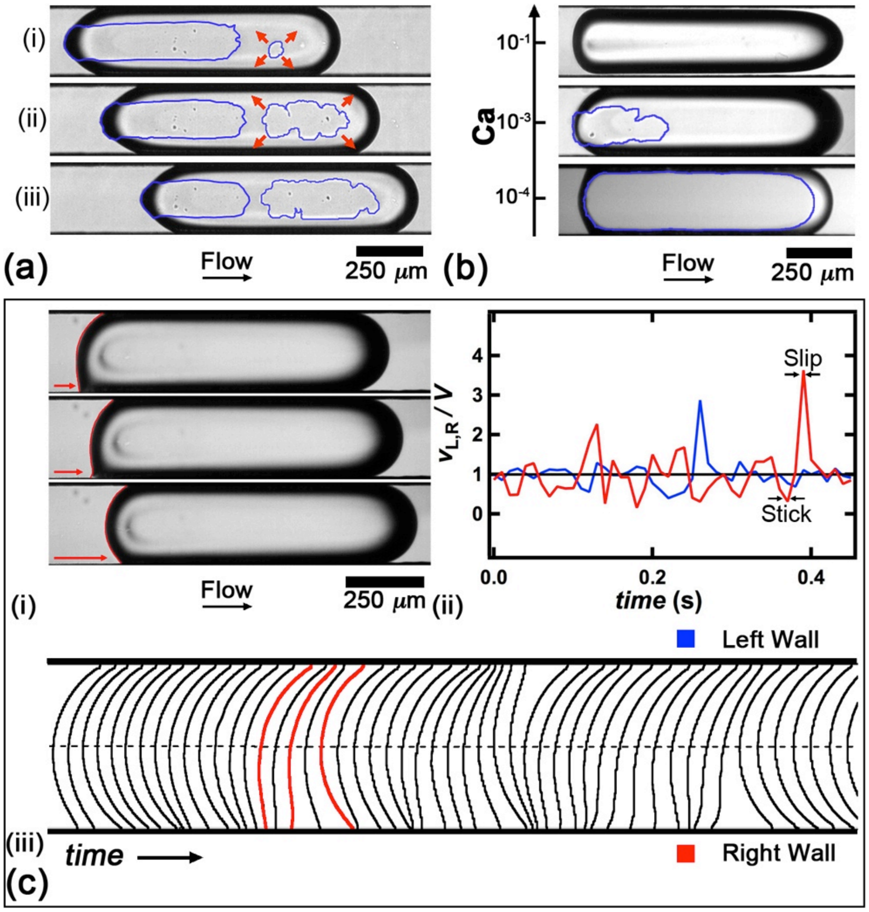

Figure 4.4 Examples of wetting dynamics. (a) Time-series of growth of dewetting patch during droplet motion, $\Delta t = 4\times10^{-3}$ s. (b) Micrographs showing influence of Ca for fixed d, contact line accented for visibility. (c) Stick and slip motion for $V/J = 0.84$. (*i*) Time series of wetting-influenced droplet motion, arrows show pinned and relaxing contact line, $\Delta t = 4\times10^{-3}$, fluid pair W-100cS, (*ii*) Temporal evolution of normalized contact line velocity for left V_L/V and right wall V_R/V and, (*iii*) superimposed contours of droplet back illustrating stick-slip motion, contours corresponding to (*i*) are accented in red.

Dynamical wetting effects are closely connected to the evolution of the metastable thin film between droplets and channel walls. In our experimental data sets, wetting droplets are observed for a capillary number Ca ranging between 10^{-4} and 10^{-2} [Figure 3.6(a)]. At such low Ca, wetting/dewetting patches of $L1$ have a tendency to adhere to surfaces and can provide nucleation site for film breakage and growth of a dewetting patch. The temporal evolution of a dewetting patch is shown in Figure 4.4(a). The relative growth of patches with respect to droplet size and velocity is given in equation (4.1).

For very low capillary numbers, a droplet can completely wet the walls, while for moderate *Ca* near the wetting/thin film transition, partially grown patches are observed at the rear of droplets [Figure 4.4(b)].

Given the droplet production method where laminar side flows of the continuous phase are injected near the sidewalls, wetting effects are more likely to occur at the top and bottom glass surface. At very low *Ca*, however, wetting effects can be important at the sidewalls. As the silicon surface of the side microchannel is produced during various etching cycles, it is less smooth than the top and bottom glass walls and stick-and-slip motion can result from surface heterogeneities. An example of such motion is shown in Figure 4.4(c)*i*. Although the average droplet velocity V measured at the centerline remains fairly constant, contact line velocities on the left V_L and right V_R sidewalls (with respect to the flow direction) show irregular jumps and dips as a moving contact line that encounters a strong surface heterogeneity can pin and relax. This movement consists in intermittent spikes in the normalized velocity of the contact line at both walls [Figure 4.4(c)*ii*]. Extraction and superimposition of the contours of a droplet back from high-speed imaging reveal the influence of stick-slip motion on droplet position at fixed time intervals [Figure 4.4(c)*iii*].

4.4. Corner droplets

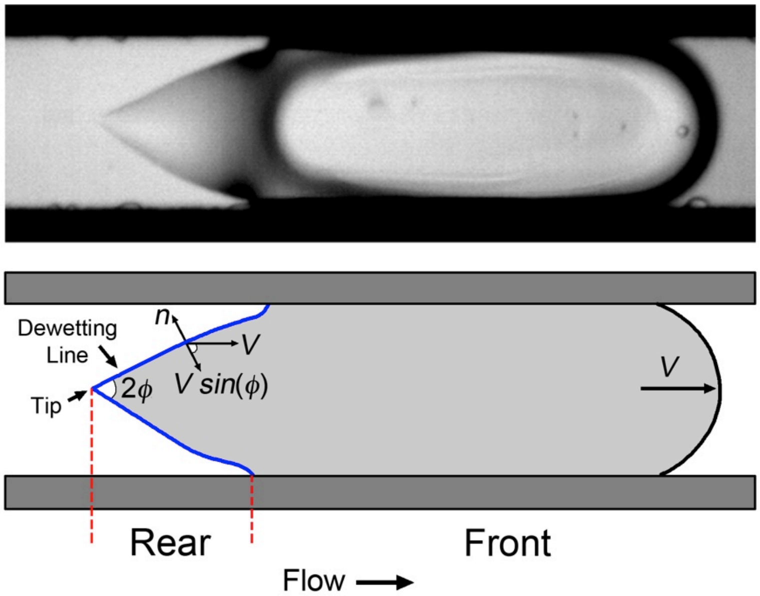

Figure 4.5 Schematic of the corner droplet with an inclined contact line on the rear. The dewetting line is shown in blue. Fluid pair: GW92-5cS.

In contrast to water droplets in PDMS oils, a different type of wetting transition was observed when high viscosity droplets made of water/glycerol mixtures are used. Particularly, we discuss the wetting effects shown by the fluid pair GW92-5cS. Due to the asymmetry between the advancing and receding branch of the dynamic contact angle[81], the droplet phase stretches and adopts different configurations such as, oval, corner, cusp and pearling at various velocities. As the wetting-droplets translate in the microchannel, the rear of the droplet constantly dewets the microchannel walls. The maximum dewetting velocity for the contact line is given by the receding critical velocity V_R. When a velocity $V > V_R$ is imposed, the dewetting line has a tendency to align with the flow direction minimizing the normal component of the velocity [89]. The dewetting line inclines at an angle ϕ to reduce the effective velocity normal to contact line to $V.\tilde{n} = V \sin(\phi)$ [Figure 4.5].

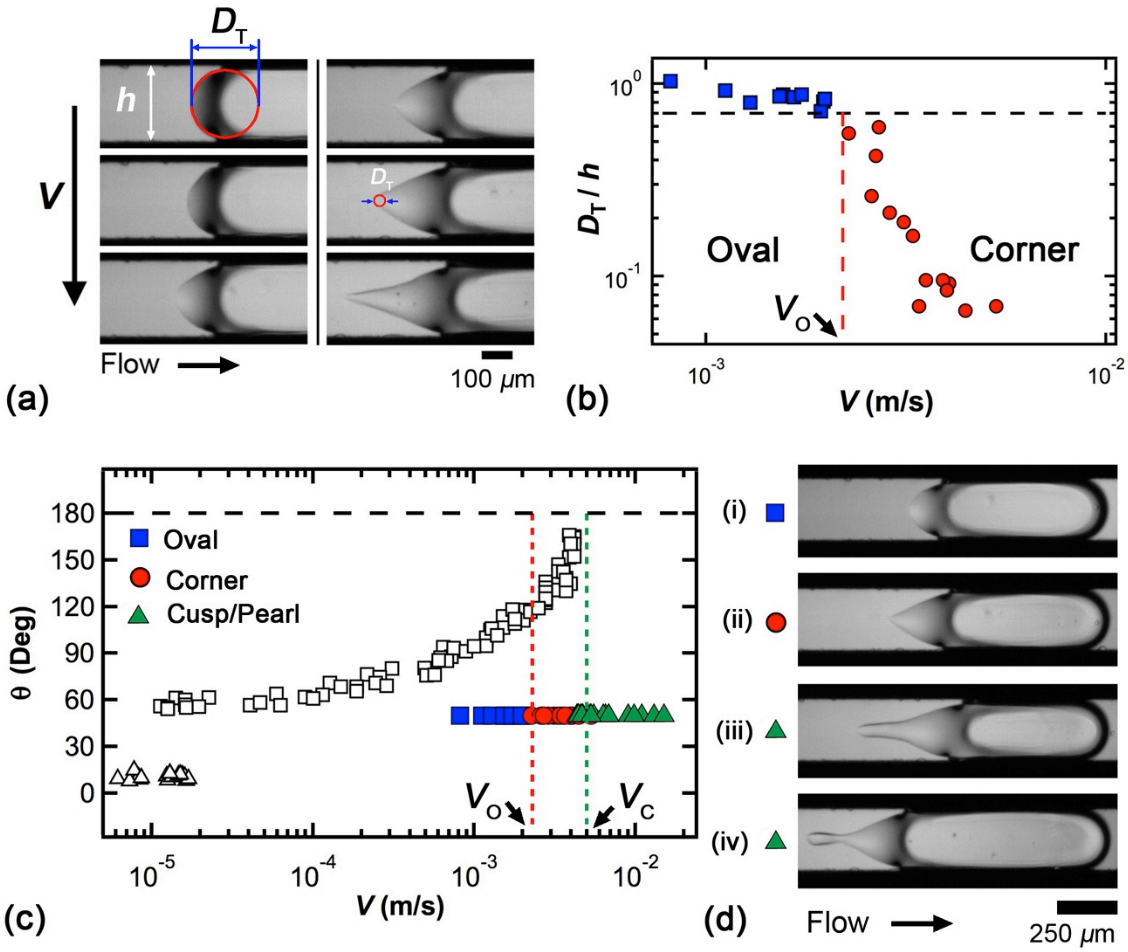

Figure 4.6 Oval, corner, cusp/pearl transition for fluid pair: G92-5cS (a) Changing morphology of the dewetting line with increasing velocity. (b) Oval to corner transition. Black line: $D_T/h = 0.7$, Red line: $V = 2.2 \times 10^{-3}$ m/s. (c) Phase diagram for the droplet transitions. Advancing contact angle (□) and receding contact angle (△) as a function of contact line velocity. Red line: Oval to corner transition. Green line: Conner to cusp transition at the advancing critical velocity V_C.

At very low velocities ($V < V_O$), the dewetting contact line assumes an oval shape with a diameter of curvature D_T [Figure 4.6(a)]. On increasing the velocity, D_T reduces to form a corner with an opening angle of 2ϕ at the tip. Corner droplets are characterized by the sudden decrease of the diameter of curvature (D_T) at the rear of droplet. The transition from oval to corner is defined at $D_T/h = 0.7$ [Figure 4.6(b)]. Although very small, the diameter of curvature of the tip D_T remains finite in the corner regime. On further increasing the velocity, the shape of the dewetting line changes to form an inflection point at the rear and this regime is named as ‘cusp’ [Figure 4.6(d)*iii*]. In cusp regime, the dewetting line at the tip is almost perpendicular to the direction of velocity ($\phi \rightarrow 90$) there by decreasing the normal component of the velocity $V \sin(\phi) \rightarrow 0$. The transition velocity for corner to cusp is found to be around the advancing critical velocity V_C. For even higher velocities Pearl regime is observed when the droplet leaves behind small sessile droplet patches on the microchannel walls [Figure 4.6(d)*iv*]. The transition velocity from cusp to pearl is not clearly defined as the droplet velocity fluctuates in the pearl regime.

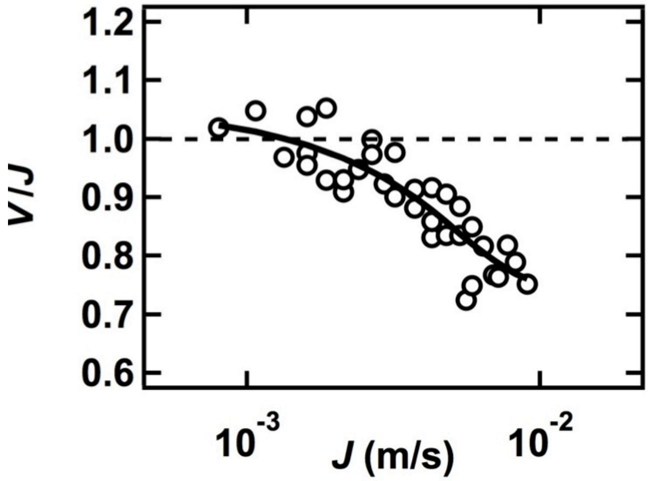

Figure 4.7 Ratio of droplet velocity and the superficial velocity (V/J) as a function of superficial velocity J. Solid line: Trend line to guide the eye.

To measure the droplet velocity V we track the front of the droplet and the superficial velocity J is calculated from the injection rates of the fluids $J = (Q_1+Q_2)/h^2$. Contrary to the less viscous droplets mentioned in section 4.2, the droplet velocity reduces with increasing superficial velocity. With increasing superficial velocity, the relaxation time for the dewetting line is reduced and sessile droplets are deposited on the microchannel walls inhibiting the droplet velocity. This shows that the changing contact line morphologies can affect the overall dynamics of the multiphase flow.

4.5. Conclusion

A classification of forced dynamic wetting transitions inside a square microchannel is made in conjunction with information gained on the natural spreading properties of each fluid pair measured using high-speed goniometry. The extrapolated critical wetting velocity V_C for each fluid pair is found proportional to the capillary velocity based on external phase viscosity η_2 and interfacial tension γ_{12} according to $V_C = Ca_c V^*$. Comparing droplet dewetting and convective timescales permit categorization of dynamic wetting phenomena in microchannels based on the parameter $d/(hCa)$. The relative droplet velocity V/J is measured and shown to depend also on the parameter $d/(hCa)$. Simple model fits are developed to predict droplet velocity in both wetting and non-wetting regimes. A variety of wetting phenomena inside square microchannels, including growth of dewetting patch, droplet morphology, and ‘stick-slip’ movement of the contact line are also reported. For the fluid pair GW92-5cS, the rear of the droplet showed an inclined dewetting line. The dewetting lines incline with respect to the droplet velocity to keep the normal velocity component below the maximum receding velocity to avoid the dewetting transition. Overall, the study shows the relevance of the dynamic advancing angle as a useful parameter to predict and control wetting transitions of segmented flows in microfluidic platforms.

5. Arrangement and coalescence of droplets in slit microchannel

5.1. Introduction

Liquid/liquid dispersions have a broad range of applications in material synthesis and petroleum engineering [101, 178, 179]. In the context of immiscible two-fluid flows in porous media, recombination processes between droplets can significantly alter flow behavior. Although droplet coalescence in air is relatively well understood [180-182], less is known about droplet merging in flowing emulsions [183]. For instance, two droplets in air coalesce upon contact but this process is delayed in viscous environments due to the presence of a thin liquid film between droplets [184, 185]. As a result, two droplets, which appear to make contact with one another in an external liquid phase, do not necessarily coalesce even in the absence of surfactant. In confined systems, variations and irregularities in the flow geometry introduce additional complexities for predicting and modeling droplet interactions and coalescence phenomena during multiphase transport at the small-scale.

Microfluidic devices are useful for generating and manipulating arrays of monodisperse droplets. The flow combination of two immiscible fluids in microgeometries produces many flow patterns [45, 66, 186-188]. Microfluidic droplets facilitate a variety of controlled operations and can be used as microreactors for encapsulating cells and chemicals [31, 189-191]. Numerous methods based on channel designs have been developed to produce, transport, break, merge, and store droplets in microsystems [34, 192-195]. An important microfluidic component consists of a chamber made of a planar microchannel connected to multiple ports. A recent theoretical study has shown the possibility to assemble complex structures in a chamber using elaborated time-dependent flows [196, 197]. The formation of compact three-dimensional droplet arrays was achieved by controlling the ratio of the chamber height to the droplet diameters in conjunction with several small inlet channels [198]. At the transition between a single inlet channel and a wide two-dimensional cell, droplets having a very low interfacial tension with the continuous phase can stretch normal to the main flow direction and breakup into complex arrays [187]. Overall, chambers are useful for manipulating microfluidic droplets and provide insights for displacing immiscible fluids in porous media.

In this chapter, we study the flow behavior of droplets as they traverse a microfluidic chamber designed as a diverging/converging slit microchannel. The flow geometry represents a simplified model system of a two-dimensional pore with practically ‘‘stagnant pockets’’. This type of interconnected pore is often encountered in natural porous matrices [199]. The extensional geometry also offers new functionalities for probing multiphase flows. For instance, dispersed flows of droplets can form an effective jet or ‘‘spray’’ of droplets [12]. The hydrodynamic coupling and the relationship between dispersed and separated flows with high-viscosity fluids are also examined.

The chapter is organized as follows. First, we characterize the microfluidic design, apparatus, and physical properties of fluids used in the study. Continuously focusing immiscible fluid streams into a square channel generates regular trains of monodisperse droplets upstream from the chamber. As this method sets the initial flow conditions prior to the pore, we determine the relationships between droplet size, distance, and velocity in the square channel as a function of flow rates of injection and fluid properties. Downstream, droplets enter the chamber and form a variety of compact lattices. The central part of this chapter is devoted to examining the morphology and dynamics of these arrangements. The morphological study includes discussions of the evolution of the droplet distance and the spread of the effective droplet spray in the chamber. Then, we investigate the dynamics of droplet assembly by recording and comparing droplet velocities and residence times in the cell with theoretical predictions. The final part of this chapter deals with the interplay of wetting and recombination processes occurring in various droplet lattices. We measure the critical droplet concentration for the onset of coalescence as a function of the capillary number and demonstrate that the time required for the intercalating film between two nearby droplets to drain and permit coalescence is proportional to the viscous-capillary time-scale based on the viscosity of the external fluid.

5.2. Schematic of microchamber and fluid properties

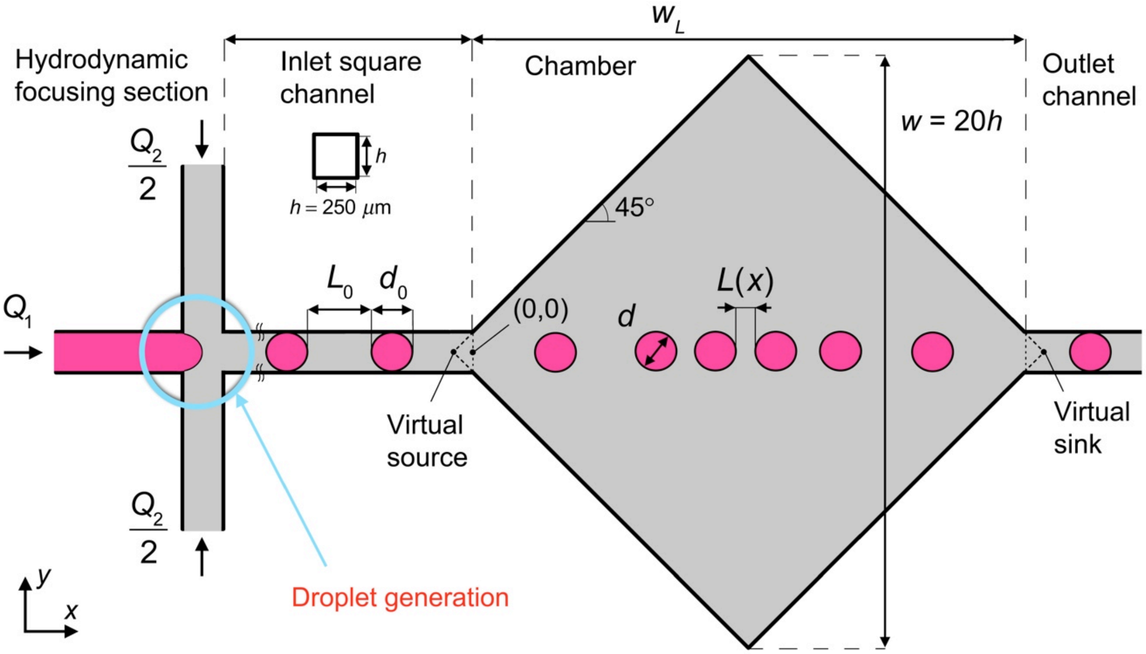

Figure 5.1 Schematic of the microfluidic module with hydrodynamic focusing section, inlet square channel, chamber and the outlet channel.

Except the change in the microfluidic platform, the experimental setup used to visualize the flow in the microchannel is described in section 3.2. The microfluidic platform is made from etched through silicon wafer (h = 250 μm) sandwiched between two borosilicate glass pieces and the glass pieces are sealed on each side of silicon using anodic bonding. The microchannel consists of four consecutive elements: (1) a right angle hydrodynamic focusing section for droplet generation (2) an inlet square channel of width h and length $20h$ (3) a diverging/converging slit microchamber of width $20h$ (4) an outlet square channel [Figure 5.1]. The depth of the microchannel along the entire length is h. The large chamber aspect ratio $w/h = 20$, gives a two-dimensional flow approximation. Droplet phase $L1$ having viscosity η_1, is injected into the central channel with a volumetric flow rate of Q_1 and the external phase $L2$ with viscosity η_2 is injected with a flow rate of Q_2 from the side channels. The flow rate for each phase is controlled independently using syringe pumps. The long square inlet channel is used to decorrelate the droplet production at the focusing section from droplet arrangement in the chamber. The reference point $(x, y) = (0, 0)$ is set at the transition between the inlet channel square channel and the microchamber. In the chamber, single phase flows at low Reynolds numbers can be described as a combination of virtual point source and sink separated by $w = 20h$. However, given the finite length of the inlet and outlet square channels of width h, the effective length of the microfluidic chamber is $w_L=19h$.

5.2.1. Fluid properties

Fluid Pair	Droplet Phase ($L1$)	External Phase ($L2$)	η_1 (cP)	η_2 (cP)	χ	Symbol
G80-1cS	Glycerol 80%	PDMS	36	0.82	44	◇
G80-5cS	-	-	36	4.59	7.8	△
G80-20cS	-	-	36	19	1.9	○
G92-20cS	Glycerol 92%	-	272	19	14.3	□

Table 5-1 Properties of fluids. γ_{12} is the interfacial tension and the viscosity ratio is given by $\chi = \eta_1/\eta_2$.

The droplet phase $L1$ is made of water/glycerol mixtures (WG) and the continuous phase $L2$ is silicone oils (PDMS) of various viscosities. Four fluid pairs with different viscosity ratios $\chi = \eta_1/\eta_2$ and similar interfacial tensions γ_{12} are examined in the absence of surfactant. The viscosity of $L1$ is chosen to be large compared to the external phase $L2$. Droplets are generated at the focusing section beyond the advancing critical velocity V_C ($\theta_D \rightarrow 180$) for all the fluid pairs and the droplets do not wet the inlet square channel walls. The inlet channel capillary number $Ca = \eta_2 J_0/\gamma_{12}$ varies between $\sim 10^{-3}$ and $\sim 10^{-1}$ where J_0 is the multiphase flow superficial velocity given by $J_0 = (Q_1+Q_2)/h^2$. The Reynolds number based on the viscosity of the external phase (η_2) varies between 8×10^{-3} and 4.

5.3. Initial droplet spacing and size.

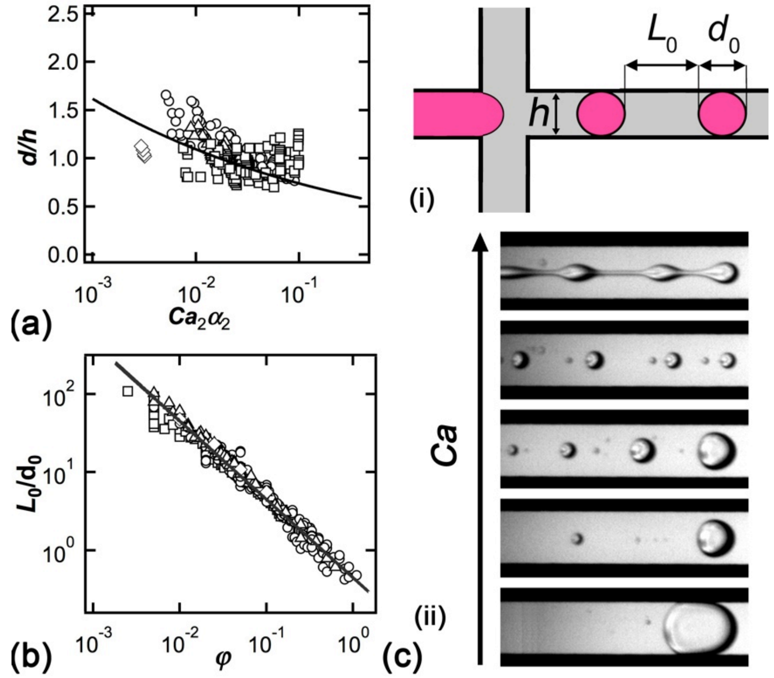

Figure 5.2 Characteristics of microfluidic emulsions in the inlet square channel. (a) d0/h as a function of $Ca_2\alpha_2$. Solid line: $d_0/h = 0.5(Ca_2\alpha_2)^{-0.17}$. (b) Initial spacing between droplets L_0 normalized with the droplet diameter d_0 as a function of flow ratio φ. Solid Line: $L_0/d_0 = 0.45\varphi^{-1}$. (c) (*i*) Schematic of the droplet generation at the focusing section. (*ii*) Formation of satellite droplets and breakage of the capillary thread as the capillary number is increased.

The morphology of the microfluidic emulsion in the chamber is set by the up-stream initial conditions in the inlet square channel. Two important parameters deciding the different arrangements in the chamber is the spacing between two droplets L_0 and the droplet length d_0 in the inlet channel. Both parameters are adjusted by controlling the flow rates Q_1 and Q_2. Other important non-dimensional quantities include the flow ratio $\varphi = Q_1/Q_2$ and the droplet concentration $\alpha_1 = Q_1/(Q_1 + Q_2)$. For the dilute emulsion ($\alpha_1 \leq 0.5$) in the dripping regime droplet size is remains almost constant $d_0 \sim h$ with large variation in the spacing L_0. In contrast, the concentrated emulsions ($\alpha_1 \geq 0.5$) show a wide variation in the droplet size d_0 with the spacing reaming almost constant $L_0 \sim h$. Previous studies on the formation of viscous droplets with $\chi \geq 22$, showed that the droplet size scales with $Ca_2\alpha_2$ where α_2 is the volume fraction of the continuous phase and the capillary number $Ca_2 = \eta_2 Q_2/(\gamma_{12}h^2)$ is associated with the superficial velocity of the continuous phase[200]. The relationship $d/h = 0.5(Ca_2\alpha_2)^{-0.17}$ shows agreement with the experimental data for dilute emulsion $\alpha_1 \leq 0.5$ [Figure 5.2(a)]. We note that there is a departure from the scaling law when $\chi \rightarrow 0$. Although the size distribution of the droplet is relatively small $0.7 < d/h < 1.8$, the change in droplet size can influence flow arrangements downstream in the chamber.

In the dilute regime ($\alpha_1 \leq 0.5$) the initial spacing between the droplets L_0 can be varied over several orders of magnitude. The ratio of the droplet spacing to the droplet diameter L_0/d_0 serves as the most important parameter in deciding the flow patterns downstream in the microchamber. Mass conservation in the segmented flow suggests a scaling for the droplet size and the droplet spacing as $d_0 \sim Q_1/h^2$ and $L_0 \sim Q_2/h^2$ resulting in a scaling for their ratio as $L_0/d_0 \sim \varphi^{-1}$. The experimental data is fitted with the scaling to get the expression $L_0/d_0 = 0.45\varphi^{-1}$ [Figure 5.2(b)].

For high capillary numbers ($Ca \sim 10^{-1}$), satellite droplets are formed during breakup. The size of the satellite droplets is negligible compared to the droplet size. On further increasing the capillary number the system switches to jetting regime. The characteristic feature of the jetting regime is the formation of a capillary thread extending into the inlet channel. The perturbations on the surface of the capillary thread grow and eventually break into droplets [Figure 5.2(c)*ii*]. Droplets produced in the jetting regime are found to be polydisperse and the spacing between two consecutive droplets varies considerably.

5.4. Phase diagram for droplet arrangements

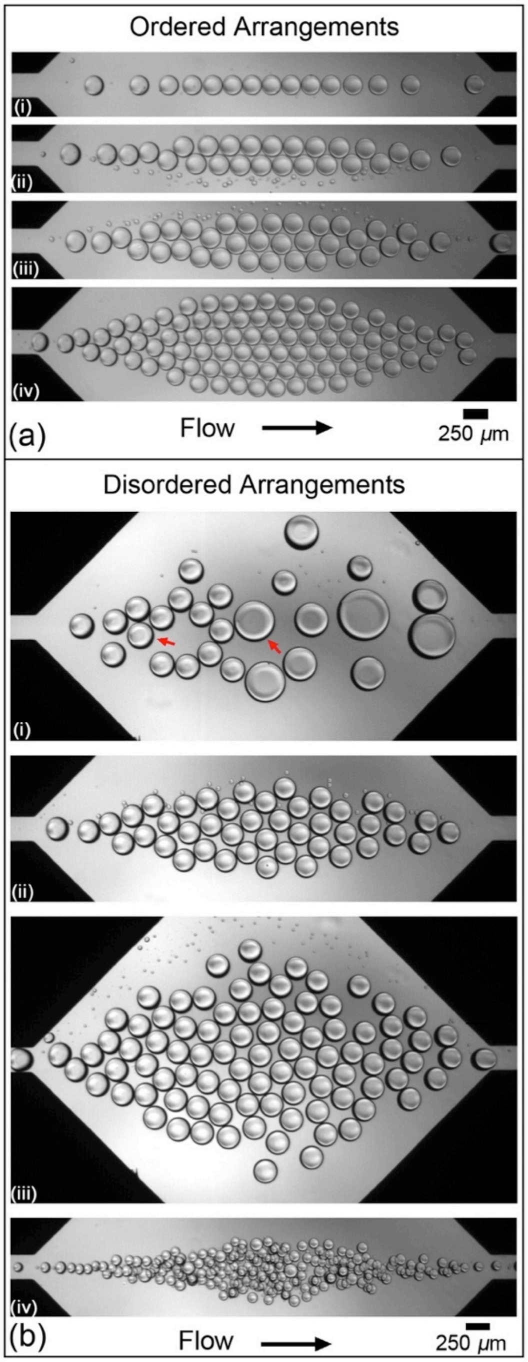

Figure 5.3 Experimental micrographs of the multiple layer droplet formation in the microfluidic chamber. (a) Ordered arrangements for the fluid pair G80-20cS. (*i*) One layer (*ii*) Two layers (*iii*) Three layers (*iv*) Six layers (b) Disordered arrangements for the fluid pair G92-20cS. (*i*) Stagnation. Red arrows show stagnant droplets attached to the walls (*ii*) Three to Six layer transition. (*iii*) Above six layers (*iv*) Jetting.

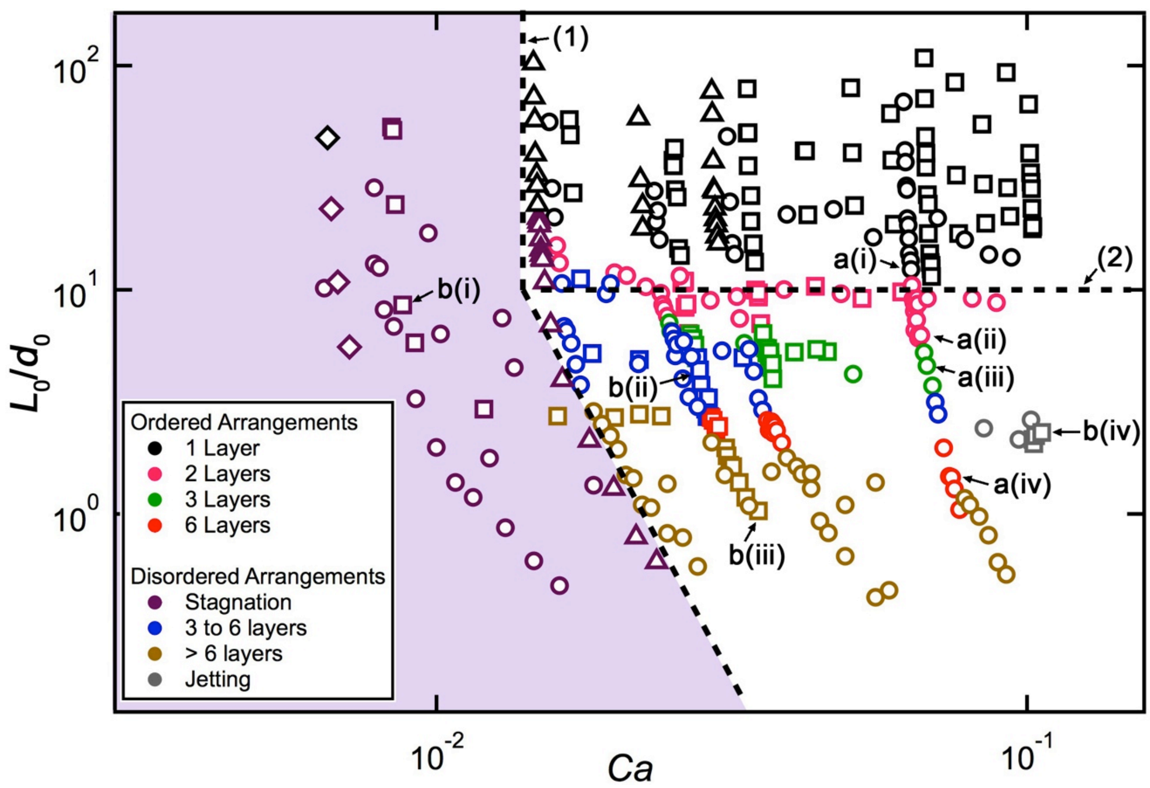

Figure 5.4 General phase diagram for all fluid pairs. The droplet arrangements shown in Figure 5.3 is indicated in the phase diagram. *Shaded region*: Stagnation of droplets at low capillary number. *Dotted Line*: (1) $Ca = 1.4 \times 10^{-2}$ (2) $L_0/d_0 = 10$.

In the diverging–converging chamber, droplets can form compact multilayer arrangements based on the injection capillary number and the initial spacing between the droplets. A summary of different ordered and disordered arrangements are illustrated in Figure 5.3 [201]. Droplets previously elongated in the square channel ($d_0 > h$) adopt a more symmetric circular shape as they enter the chamber. On average, the number of droplets in the chamber remains constant for ordered arrangements since the time average number of incoming droplets is identical to the number of droplets exiting the chamber. In contrast, disordered arrangements show fluctuation in the number of droplets due to the coalescence of droplets as well as the difference in the droplets entering and exiting the chamber. The formation of the regular and irregular packing structures depends on the initial droplet concentration in the square channel. For large initial spacing ($L_0/d_0 > 10$), droplets formed one layer [Figure 5.3(a)*i*]. As L_0/d_0 is progressively reduced, the ordered arrangements of two, three and six layers of droplets are observed [Figure 5.3(a)*ii-iv*].

Four or five layered arrangements were not observed, but a complex transition from three- to six-layered arrangements [Figure 5.3(b)*ii*]. Not more than six layers are observed, since the chamber size and the aspect ratio (w/h = 20) appear to prevent the formation of regular structures with more than six layers. On further decreasing L_0/d_0 beyond the six layered arrangement, the close packing structure disappear to form 'above six layer' transition [Figure 5.3(b)*iii*]. In this transition regime, the droplets migrate laterally to the both corners of the chamber before the beginning of the converging section ($x \sim 10h$). The lateral migration of the droplets serves to accommodate the additional incoming droplets due to the discrepancy in the number of the droplets entering and exiting the chamber. At very high capillary number ($Ca \sim 10^{-1}$), the droplets generation switch to jetting regime where polydisperse droplets considerably smaller than the channel depth ($d_0 < h$) are produced. On entering the chamber, the smaller size of the droplets permits the formation of a complex three-dimensional arrangement [Figure 5.3(b)*iv*].

A combined phase diagram for all the fluid pairs is displayed in Figure 5.4 summarizing the occurrence of the arrangements as a function of the control parameters L_0/d_0 and Ca. For low inlet capillary number ($Ca < 1.4 \times 10^{-2}$), we observed a stagnation regime, when a few droplets attach to the top and bottom walls in the diverging channel [Figure 5.3(b)*i*]. A detailed analysis of this regime is given in section 5.9. The viscosity of the external phase η_2 plays a major role in the formation of droplet assemblies. Over the range of parameters investigated ordered layered arrangements are observed for fluid pairs G80-20cS and G80-20cS with a relatively viscous continuous phase. In contrast, other fluid pairs G80-1cS and G80-5cS yielded only one layer arrangements since the droplets at close proximity are found to rapidly coalesce, significantly altering the flow morphologies.

5.5. Distance between droplets

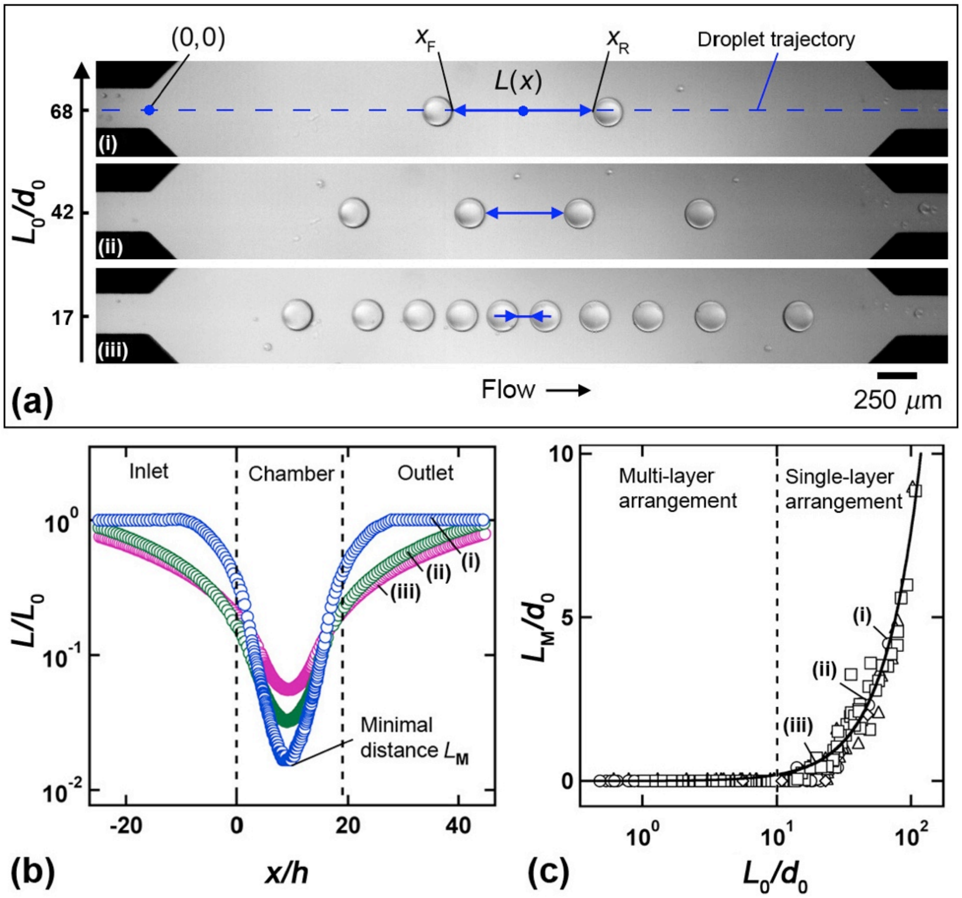

Figure 5.5 (a) Evolution of the distance between two consecutive droplets $L(x)$ in the chamber as a function of the x-coordinate for one layer arrangement (very dilute emulsion). Fluid pair: G80-20cS. Q_2 = 400, Q_1 = 2, 4, 10 (*top to bottom*). (b) Droplet spacing L normalized by the initial spacing L_0 as a function of dimensionless position x/h. (c) Evolution of the normalized minimum distance L_M/d_0 between the droplets as a function of the droplet train aspect ratio L_0/d_0 in the inlet channel for all the fluid pairs. $L_M/d_0 = \omega(L_0/d_0)^{1.6}$ with $\omega = 5 \times 10^{-3}$.

The distance between to successive droplets L is an important factor governing the droplet assembly. In the chamber, L is a function of the spatial coordinate x. One-row arrangement (n = 1) is characterized by a droplet trajectory following a straight line through the center of the chamber with y = 0. The spatiotemporal diagrams extracted from high-speed movies are used for the continuous measurement of $L(x)$ and plotted as a function of position x. Custom made *MATLAB* and *FORTRAN* codes along with the "reslice" function in *ImageJ* is used to generate the curve in Figure 5.5(b). For two successive droplets at an instant t, the rear position of the first droplet $x_R(t)$ and the front position of the second droplet are used to compute $L(t) = [x_R(t) - x_F(t)]/2$. The x–coordinate associated with L corresponds to $x = [x_R(t) + x_F(t)]/2$. The evolution of the distance normalized by the initial distance in the square channel L/L_0 is shown as a function of the non-dimensionalized x-coordinate x/h [Figure 5.5b]. The spacing decrease as the droplets enters the diverging section of the chamber to a minimum of L_M and increases on entering the converging section. The minimal distance occurs at center of the channel corresponding to the transition between the diverging and converging section at $L_M = L$ ($x = w_L/2$). In very dilute regime, the normalized distance decrease in the inlet channel since the first droplet decelerates in the chamber, while the succeeding droplet has a constant velocity in the inlet channel. The constant velocity property in the inlet channel is used to calculate very large initial distance L_0 by extrapolating spatiotemporal diagrams for dilute case. For all the fluid pairs listed in Table 5-1 the minimal distance L_M/L_0 is between the droplets is measured as a function of the initial droplet train morphology factor L_0/d_0 and data fits well to the curve $L_M/d_0 = \omega(L_0/d_0)^{1.6}$ with $\omega = 5 \times 10^{-3}$ [Figure 5.5(c)]. The minimum distance is negligible for $L_0/d_0 < 10$. In this case, the droplets are in apparen t contact with one another to form multilayer arrangements. Above this critical value, $L_0/d_0 > 10$, L_M increases monotonically and the droplets behave independent of one another. The critical behavior of the droplets at $L_0/d_0 \sim 10$ is imposed by the aspect ratio of the chamber $w/h = 20$ since $d_0 \sim h$ and $x_M = w_L/2$.

5.6. Envelope of droplet stream

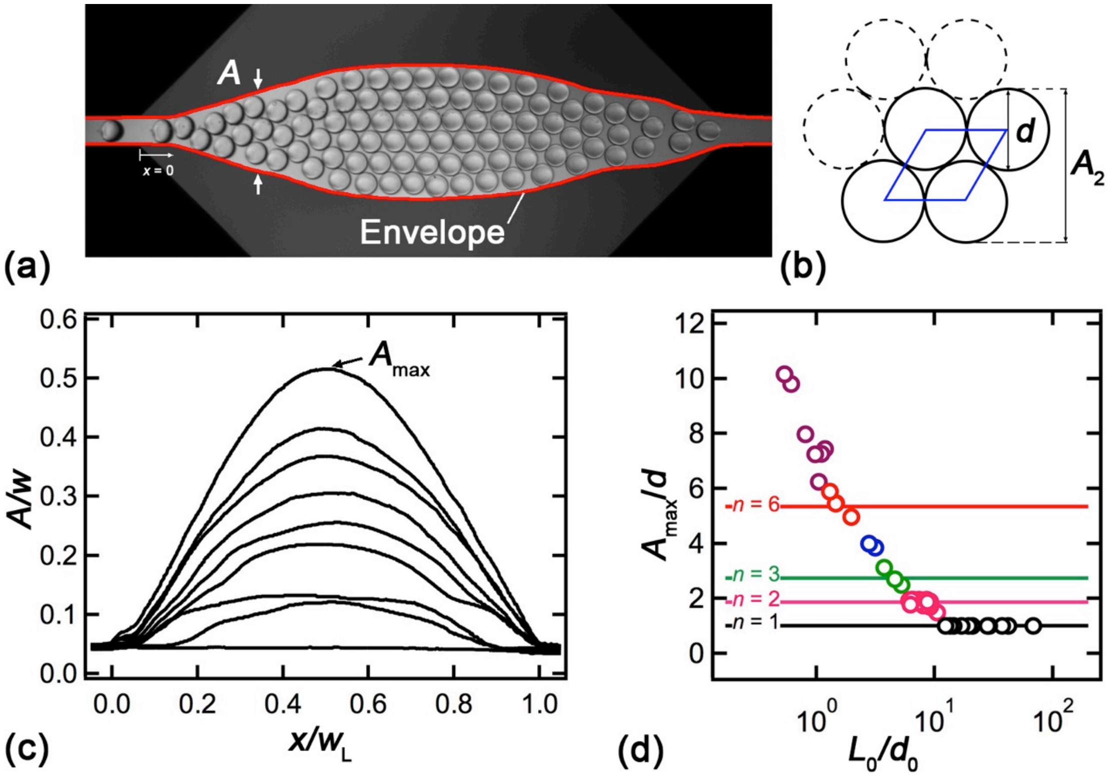

Figure 5.6 (a) Experimental micrograph is superimposed with the contour of the droplet envelope generated from the composite image. (b) Shows the calculation of amplitude A_2 associated with 2 rows of hexagonal close packing of spheres between two plates. (c) Spatial evolution of the envelope amplitude A/w for fluid pair G80-20cS and fixed Q_2 = 400 µL/min with Q_1 = 180, 160, 140, 120, 100, 80, 40, 30, 13 µL/min (*from top to bottom*) (d) Maximum amplitude normalized with the diameter in the chamber $A_{\max}/d$ as a function of normalized initial spacing in the inlet L_0/d_0. Fluid Pair: G80-20cS. Q_2 = 200 µL/min with varying Q_1.

The microfluidic chamber allows us to study the formation of compact arrays of droplets confined by the flow of external phase $L2$. The dense stream of droplets is confined within an envelope of amplitude A towards the center of the chamber that typically increases with the dispersed phase concentration α_1. The evolution of the amplitude $A(x)$ along the chamber is calculated by generating a composite image by superimposing the micrographs from the high-speed movie [Figure 5.6(a)]. The amplitude from the composite image captures the average flow field of droplets along the chamber. The droplet amplitude is widest in the center of the channel $A_{\max} = A(x = w_L/2)$ [Figure 5.6(c)], similar to the a stream made of continuous fluid [202]. This property is a result of mass conservation since the minimal distance L_M is also found at this location. The shape of amplitude is determined by the shape of the chamber geometry. Typically for a fixed flow rate of the external phase Q_2, the maximum amplitude A_{max} of the envelope increase with Q_1 as the droplet concentration inside the chamber increases. A_{max} is almost constant for the one layer arrangement since $A_{max} \sim d$ where d is the diameter of the droplet in the chamber. A_{max} increases in steps corresponding to different layered patterns. Different two-dimensional lattices are observed in the chamber namely, hexagonal close packing, centered regular packing, hexagonal dilute packing and random close packing. For hexagonal close packing, the most compact lattice, a maximum amplitude A_n can be calculated based on the diameter of the droplet as $A_n = d\,[1+ (n - 1)(3/4)^{1/2}]$ where n is the number of droplet layers [Figure 5.6(b)]. The calculated amplitude A_n shows good agreement with the experimental values of maximum amplitude A_{max} associated with the corresponding rows. [Figure 5.6(d)].

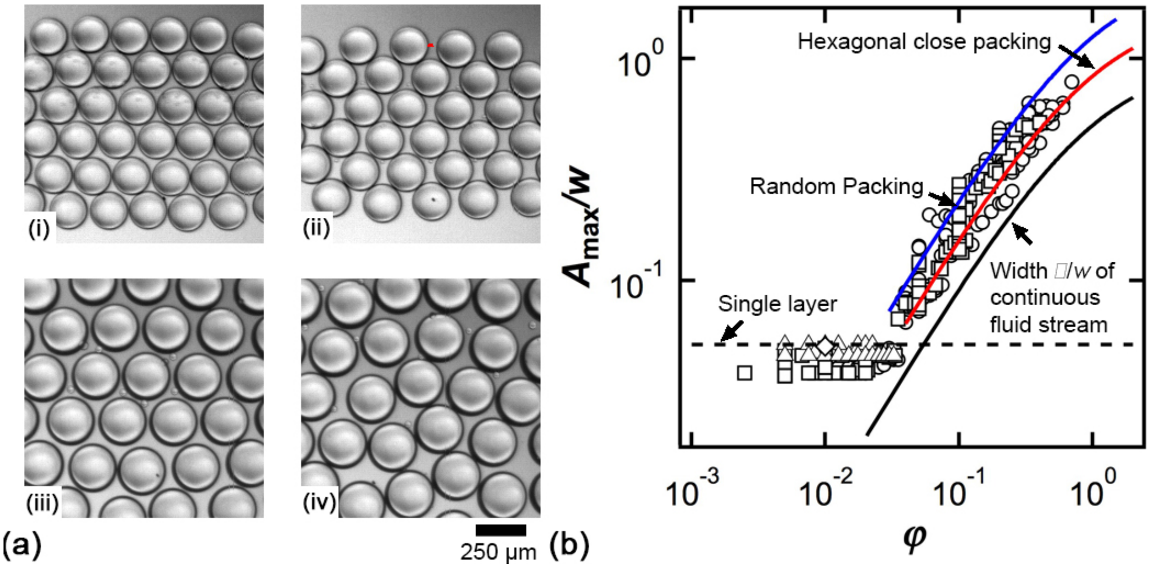

Figure 5.7 (a) Examples of droplet arrangements: (*i*) hexagonal close packing (*ii*) centered rectangular packing (*iii*) hexagonal dilute packing (*iv*) random close packing (b) Evolution of normalized maximum amplitude A_{max}/w as a function of flow ratio φ with equivalent width ε of a continuous stream in the chamber for all the fluid pairs. Dotted line: $A_{max}/w = 0.05$.

Using the maximum amplitude a comparative study is made between the closely packed discrete droplet stream and a continuous fluid. For two miscible fluids of similar viscosity in a plane channel of width w, the thickness ε of the hydrodynamically focused streams is given by $\varepsilon/w=(1+\varphi^{-1})^{-1}$. This relationship is plotted along with the maximum amplitude of the droplet stream A_{max}/w as a function of the flow ratio φ to show the increase in the maximum amplitude due to the external phase in the spacing between the droplets [Figure 5.7(b)]. One of the key differences between the two cases occurs at low flow ratio φ when the A_{max} remains constant for one layered arrangement and is equal to $d \sim h = w/20$ given by the chamber aspect ratio. For higher flow ratios, a direct comparison can be drawn between the A_{max} and ε by using the packing factor a. The packing factor a is defined as the volume of droplet phase occupied in a unit lattice structure. For a two dimensional hexagonal close packing arrangement of spheres, $a = (\pi d^3/12)/[\sqrt{3}d^3/4] \approx 0.6$. Balancing the volume flow rate of a continuous stream $Q = Vh\varepsilon$ with the effective flow rate of a droplet stream $Q_{\mathrm{d}} = VhA_{\mathrm{max}}$ as $Q = aQ_{\mathrm{d}}$, yields $A_{\mathrm{max}} = \varepsilon/a \approx (w/0.6)(1 + \varphi^{-1})^{-1}$. This relationship is plotted in Figure 5.7(b) shows good agreement with the smallest measures values of the maximum amplitude A_{max}/w. The upper value for the A_{max}/w appears to correspond to a lower packing factor $a = 0.4$ and is associated with random close packing.

5.7. Velocity and residence time of droplets

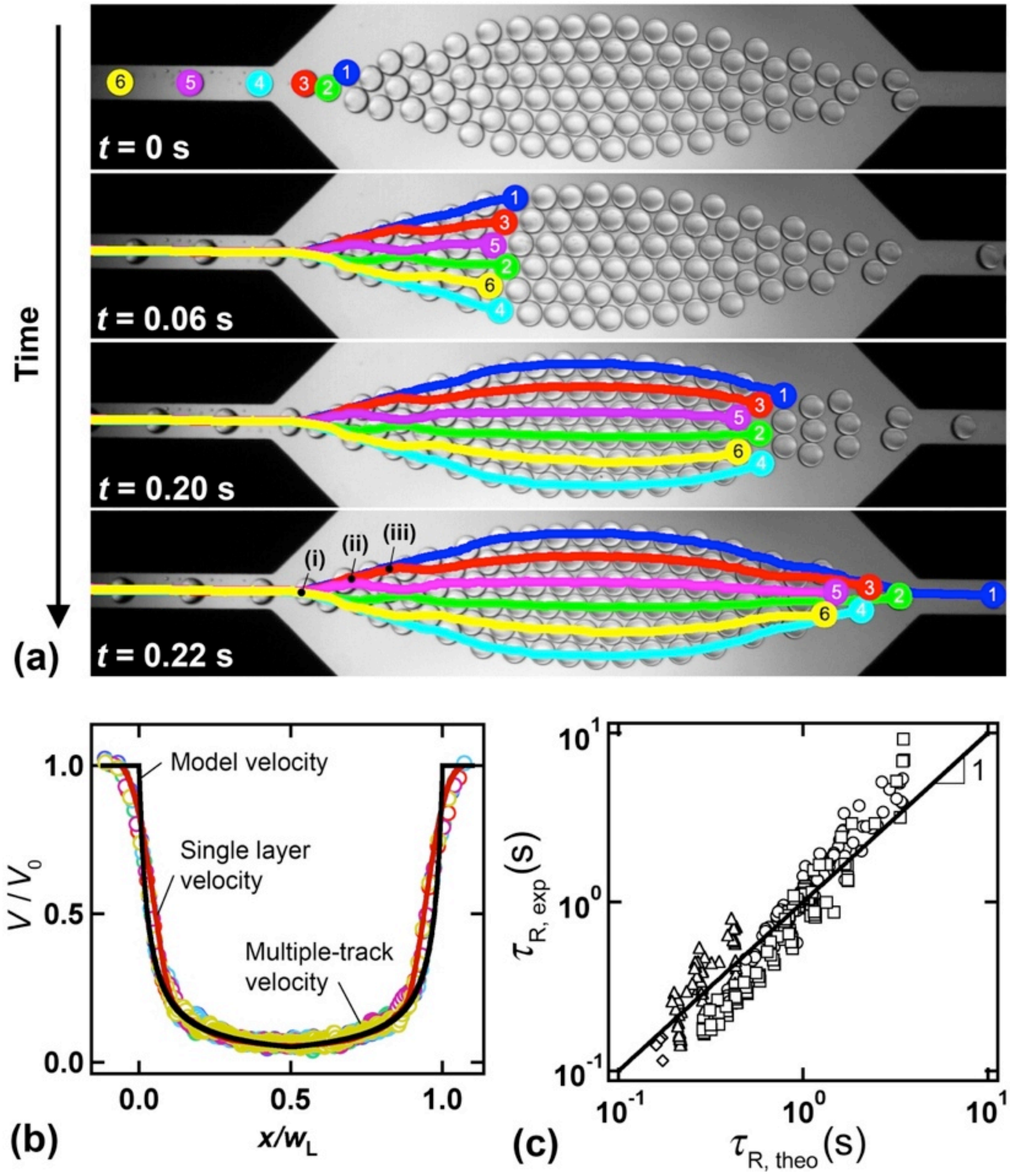

Figure 5.8 (a) Temporal evolution of trajectories of six successive droplets in a six-layer arrangement. Fluid Pair: G80-20cS. (*i*) Separation point for trajectories between upper and lower branch, (*ii*) Separation point for three droplets in upper branch, (*iii*) Separation point for two droplets at the edge of the upper branch. (b) Evolution of droplet velocity V normalized by inlet velocity V_0 as a function of normalized spatial coordinate in the x–direction x/w_L with model velocity, single layer velocity (Fluid pair: G80-20cS, flow rates Q_1 = 6, Q_2 = 200 μL/min) and multilayer velocities corresponding to each colored trajectories in (a). (c) Measured residence time $\tau_{R,exp}$ versus theoretical residence time $\tau_{R,theo}$. Solid Line: $\tau_{R,exp} = \tau_{R,theo}$.

The multiphase superficial velocity J is modified in the microfluidic chamber. The creeping flow situation with low Reynolds number Re permits a simple expression for the velocity $J(x)$ using a source and sink flow approximation. In the diverging channel ($x \leq w_L/2$), the velocity decreases as $J = J_0/(2x/h)$ until reaching $J = J_0/20$ for $x = w_L/2 = 10h$ at the transition between diverging and the converging channel. In the converging section ($x \geq w_L/2$), the flow experiences a similar convective acceleration until $J = J_0$ for $x = w_L$. To examine the temporal evolution, of droplet velocity in the chamber $V(x)$ is normalized by the initial droplet velocity V_0 in the square channel. For one row arrangement, the droplet velocity is calculated by processing the spatiotemporal diagrams as $V(x,t) = \mathrm{d}x/\mathrm{d}t$ where $x = (x_F+x_R)/2$ with x_F as the front and x_R as the back of the droplet. In multilayer formation, the velocity and trajectory of each droplet is calculated using the "Manual Tracking" plug-in for *ImageJ*. Droplets are periodically deposited into upper and lower branch similar to thread folding[203, 204]. The trajectories resemble the continuous phase streamlines and can be roughly modeled as circular arcs between source and sink located inside the chamber at $x \approx h$ (*i*) and $x = w_L - h$, respectively. In the example shown in Figure 5.8a, the separation point for trajectories of the three droplets in the upper branch (*ii*) is located further downstream. A similar behavior is observed for the two droplets near the edge (*iii*). In the ordered arrangements as shown in Figure 5.8a, the trajectories of the droplets repeat in cyclic manner. The normalized velocity of each droplet V/V_0 computed from the experimental movies show good agreement with the model velocity J and the velocity extracted for $n = 1$ [Figure 5.8(b)]. In the region where J changes significantly, the droplets tend to adopt a smother velocity than our simple prediction. An interesting aspect of the droplet assembly is that the velocity of droplets near envelope edge is similar to the one associated with droplets in the center of the envelope with $V/V_0 \approx J/J_0$. The distance traveled by droplets near edge only slightly surpasses the distance in the center of the chamber at $y = 0$. As a result of this property the droplet lattices flow as a solid crystal of droplets having a velocity equivalent to one row arrangement. Droplets exit the channel in the same order of entry.

Using the symmetry between the diverging and converging channels, the residence time $\tau_{R,\mathrm{theo}}$ is calculated by integrating $\mathrm{d}\tau_R = [2/J(x)]\mathrm{d}x$ for varying x from 0 to $w_L/2$

and yields $\tau_{R,theo} = w_L wh/(Q_1+Q_2)$. For a variety of droplet arrangements, the residence time $\tau_{R,exp}$ is experimentally measured from the movies and found to be in good agreement with $\tau_{R,theo}$. Small residence time is typically associated with large capillary number Ca and $\tau_{R,exp}$ are lower than the calculated values indicating that lubricated droplet travel faster than J. In general this system allows for controlling the residence time in the chamber with flow rates of injection regardless of the flow morphology.

5.8. Droplet coalescence

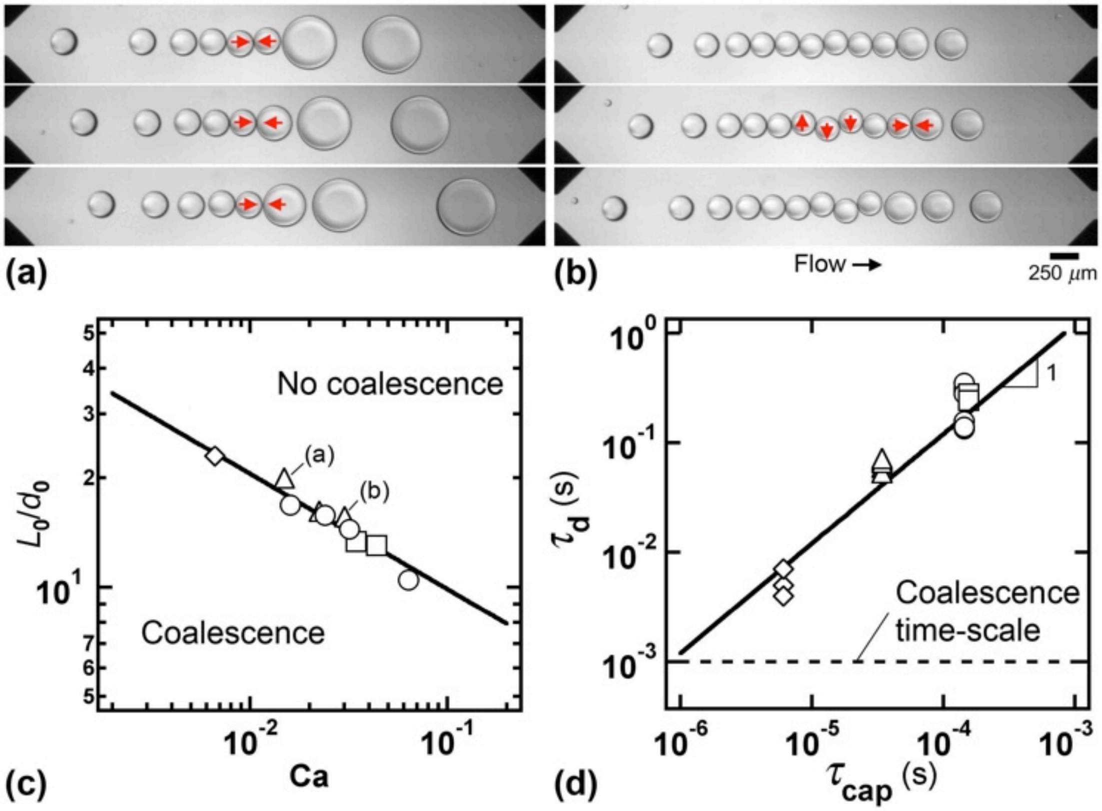

Figure 5.9 Onset of coalescence in the microfluidic chamber. *From top to bottom*: Time series of successive droplet coalescences for one row arrangement (n = 1). Fluid Pair: G80-5cS. (a) Low capillary number $Ca \approx 1.5 \times 10^{-2}$, Δt = 48 ms. (b) Moderate capillary number $Ca \approx 3 \times 10^{-2}$, Δt = 9 ms. Arrow shows next droplet coalescence and buckling of droplet chain. (c) Diagram of first coalescence observed as L_0/d_0 is progressively decreased for all fluid pairs. Solid Line: $L_0/d_0 = 4.8Ca^{-0.32}$. (d) Comparison between measured draining time τ_D and calculated viscous capillary time scale τ_{cap}. Solid Line: $\tau_D = 10^3\tau_{cap}$.

Microfluidic chambers are used in many applications and provide a convenient platform for merging two consecutive droplets [205, 206]. When two droplets come together, the capillary forces join them over a short period of time defining a coalescence time scale as $\tau_c < 10^{-3}$ s. Although this mechanism is spontaneous in air, the droplets in apparent contact need not coalesce in a viscous environment, even in the absence of surfactant. In an external phase, coalescing of two droplets require the draining of the thin film between the two droplets in apparent contact. Confinement by the microchannel walls might also play a role in determining the draining time. Measurement of the draining time is relatively scarce due to the difficulty in manipulating individual droplets in a viscous matrix. Here, we conduct experiments by fixing Q_2 and progressively increasing Q_1 for each fluid pair. For large initial spacing $L_0/d_0 > 30$, the minimum distance between droplets is always $L_M > 0$ and no coalescence is observed. As L_0/d_0 is decreased, various coalescence regimes are observed. The fusion of droplets produces a larger droplet, which reduces the speed due to its increased drag. For low capillary numbers and $n = 1$, incoming droplets merge with larger front droplets and steady regimes where fused droplets made of three or four initial droplets are observed [Figure 5.9(a)]. Over the range of parameters investigated, droplets made of more than five initial droplets become stagnant and produce the ‘‘stagnation regime’’ for very low Ca. For moderate capillary numbers, steady binary droplet coalescence regimes characterized by leading droplets made of two initial droplets are also observed [Figure 5.9(b)]. The slow motion of a leading droplet in one-row arrangement can lead to the buckling of the droplet chain, as indicated by the arrows in Figure 5.9b. For large capillary numbers, although coalescence events do occur, they remain relatively rare. Using our experimental protocol, we progressively decrease L_0/d_0 and note the critical value where the first droplet coalescence is observed as a function of the capillary number $Ca = \eta_2 J_0/\gamma_{12}$ [Figure 5.9c]. Experimental data show that the critical L_0/d_0 decreases with Ca according to $L_0/d_0 = 4.8Ca^{-0.32}$. This gives a critical concentration for the onset of droplet coalescence as $\alpha_{1C} \approx (1 + 10.7Ca^{-0.32})^{-1}$. In other words, the stability of the emulsions in microgeometries improves with speed of injection. The draining time τ_D required for two droplets to coalesce is measured by counting the number of frames in a movie between the first contact and coalescence [Figure 5.9d]. The data suggest draining time τ_D is proportional to the capillary time scale $\tau_{cap} = \eta_2 h/\gamma_{12}$ as τ_d

~ $10^3\tau_{\mathrm{cap}}$. This shows the importance of the absolute viscosity of the external phase η_2 in triggering coalescence. In short, the coalescence processes can be predicted by comparing the draining time τ_d with the residence time τ_R : $\tau_\mathrm{d} > \tau_\mathrm{R}$ for coalescence and $\tau_\mathrm{d} > \tau_\mathrm{R}$ for the absence of coalescence.

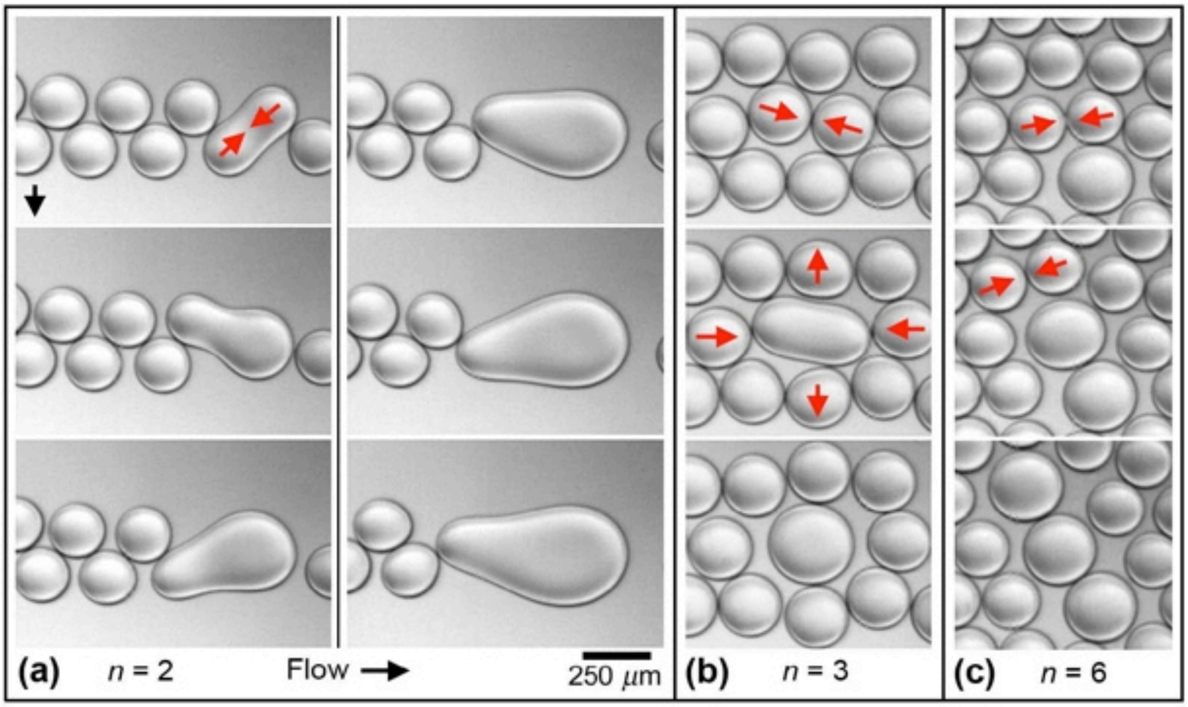

Figure 5.10 Examples of droplet rearrangement processes due to coalescence. Fluid pair: G80-20cS. (a) Coalescence cascade in a two row arrangement (n = 2), Q_1 = 25, Q_2 = 400 μL/min. (b) Droplet merging in a three-row arrangement (n = 3), Q_1 = 50, Q_2 = 400 μL/min. (c) Coalescence avalanche in a six row arrangement (n = 6) Q_1 = 41, Q_2 = 200 μL/min.

Coalescence process can introduce significant rearrangements in the layered arrangements. In the one layer arrangement, coalesced droplet can form larger droplets in the converging section and exit the chamber. For multilayer arrangements, various situations are observed as a result of coalescence. The actual merging of two droplets introduces local transient flows around the droplets that alter interstitial spaces between the neighboring droplets, which may trigger their fusion similar to a chain reaction. Figure 5.10a shows the time series of a coalescence cascade in two row arrangements. Two droplets in close proximity fuse and create a larger, slow moving droplet that collects new incoming droplets. For larger *n*, the position of surrounding droplets is directly affected by single coalescence event. For *n* = 3, the merging of two droplets in the center can produce a larger droplet with eight neighboring droplets circularly arranged [Figure 5.10(b)]. Coalescence avalanches are more likely to occur in compact arrangements with *n* = 6. As shown in Figure 5.10(c), the fusing of two droplets induces the coalescence of two other droplets in the vicinity of the first coalescence. The second coalescence, event displaces nearby droplets and generates a third coalescence. Overall, the coalescence event may appear as random but can be controlled by the convective time scale, (*i.e*. the residence time τ_d) in micro geometries.

5.9. Wetting droplets in stagnation regime.

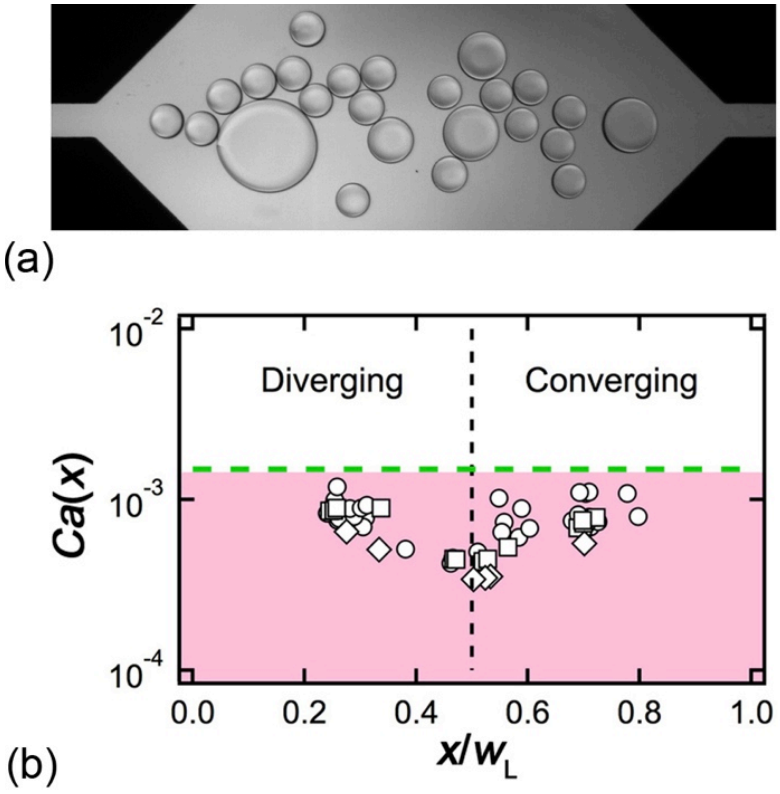

Figure 5.11 (a) Experimental micrograph of wetting droplet in stagnation regime, Q_1 = 3, Q_2 = 60 µL/min. (b) Local capillary number *Ca*(*x*) as a function of the *x*-coordinate. Dotted Green line: *Ca*(*x*) = 1.5 × 10^{-3}. Shaded Region represents wetting droplets in the stagnation regime.

Droplet wetting in the microchamber significantly affect the formation of layered arrangements. In the stagnation regime, partially wetting droplets remain attached to the channel walls in microchamber at very low capillary number [Figure 5.11(a)]. Although non-wetting droplets are produced in the inlet channel, the superficial velocity is reduced by a factor $w/h = 20$ compared to the inlet square channel velocity J_0. The modified superficial velocity $J(x)$ at a given cross-section of the chamber is used to calculate the local capillary number as $Ca(x) = \eta_2 J(x)/\gamma_{12}$. The local capillary number $Ca(x)$ is plotted with the x-position in the chamber shows the high relative occurrence of droplet wetting towards the middle of the chamber ($0.2 < x/w_L < 0.8$). The droplets partially wet the microchannel walls in the chamber below a local capillary number value of $Ca(x) \approx 1.5 \times 10^{-3}$ [Figure 5.11(b)] compares well with the previous work on bubble adhesion [170] and the wetting transition in Figure 3.6(a).

For a wetting droplet, the contact angle hysteresis yields a droplet adhesion force on the solid that is larger than the drag force exerted by the external phase $L2$. The attached droplet obstructs the continuous path of the succeeding droplets resulting in coalescence on a few occasions. Coalescing augments the droplet size, increasing the drag imparted by the continuous phase and detach from the walls. A coalesced droplet in the chamber adopts a pancake-like shape, sandwiched between the microchannel walls. As the coalesced droplet moves towards the center of the chamber, the velocity of the coalesced droplet is further reduced. The reduction in the velocity of the coalesced droplet can lead to re-attachment to the walls and additional coalescence with the succeeding droplets. Hence the stagnation regime is characterized by the complex interaction of droplet coalescence and wetting. At the end of converging flow field ($x/w_L > 0.8$), the droplets are swept by the external phase into the outlet channel without any occurrence of coalescence.

5.10. Conclusion

In this chapter the flow of a stream of droplets in a microfluidic chamber is discussed quantitatively using four different fluid pairs of varying viscosities and similar interfacial tensions. Controlling the droplet train aspect ratio L_0/d_0 along with the injection flow rates permits the manipulation of the flow patterns downstream in a microfluidic chamber. The initial droplet train aspect ratio L_0/d_0 is inversely proportional to the flow ratio φ. One-row arrangements are formed for a droplet spacing above $L_0/d_0 > 10$. On decreasing the initial distance between droplets, compact droplet lattices with different rows n are observed. For dilute emulsions the minimal distance between the droplets L_M is observed at the middle of the chamber and can be given by $L_M/d_0 = 5 \times 10^{-3}(L_0/d_0)^{1.6}$. The spatial evolution of the amplitude of the droplet stream is studied and found that the maximum amplitude A_{max} occurs at the center of the chamber. An expression for the amplitude A_n is calculated with the hexagonal close packing arrangement and compared with the experimental amplitude A_{max}. The maximal amplitude A_{max} is also compared with a continuous fluid focused by a sheath fluid taking into account the packing factor a according to $A_{max} \approx (1/a)(1 + \varphi^{-1})^{-1}$. The maximal amplitude A_{max} varies between a packing factor $a = 0.6$ corresponding to two dimensional hexagonal close packing and $a = 0.4$ for random close packing. The evolution of the droplet velocity in the chamber is compared to the local multiphase velocity. All the droplets in the droplet stream is displaced at the same velocity as the superficial velocity. The measured droplet residence times in the cell are found to follow the theoretical relationship $\tau_{R,theo} = w_L wh/(Q_1+Q_2)$. Finally an expression for droplet concentration and capillary number for the onset of coalescence in a pore is established. The relevant factor for the onset of droplet coalescence is found to be the viscosity of the external phase η_2 and the data suggest a maximal droplet concentration of $\alpha_{1C} \approx (1+10.7Ca^{-0.32})^{-1}$ before the onset of coalescence. The film draining time τ_D between the droplets in apparent contact is proportional with the capillary time scale, $\tau_D \sim 10^3\ \tau_{cap}$. Stagnation regime is observed below an injection capillary number of $Ca < 1.4 \times 10^{-2}$. Stagnation regime is the result of complex interaction between droplet wetting and coalescence. This regime is further examined using a local capillary number to find a critical value $Ca(x) > 1.5 \times 10^{-3}$ for the smooth passage of lubricated droplets without wetting the microchannel walls.

We show the possibility to control the coalescence process in the absence of surfactant. In the absence of coalescence droplets can be modeled as spheres and transported with the same velocity as the local multiphase flow velocity. The study highlights the interplay between hydrodynamic coupling and the coalescence phenomena. In the absence of surfactants, coalescence can be controlled in a dynamic system by increasing the viscosity of the external phase in conjunction with large injection flow rates.

5.11. Future development

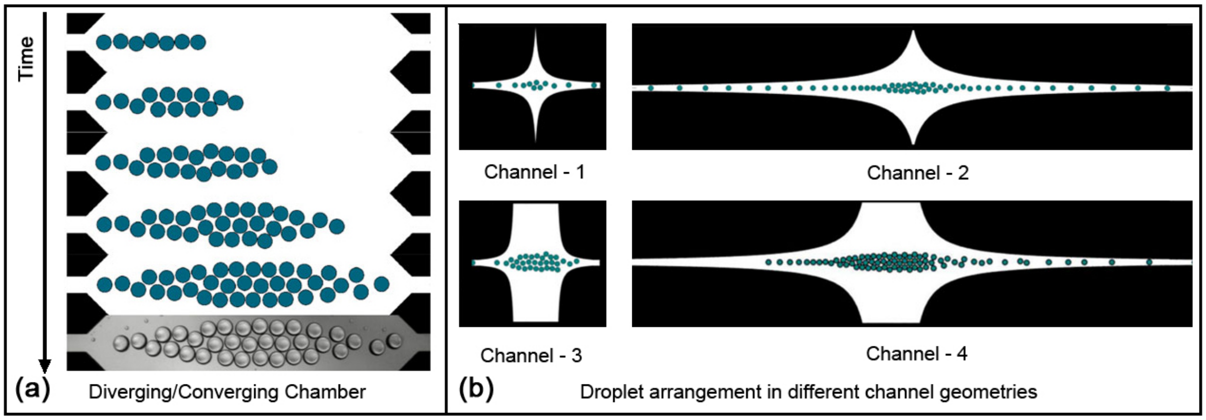

Figure 5.12 Numerical simulation of droplet arrangement for $L_0/d_0 = 6$ (a) Numerical model predicting the three layered arrangement in diverging-converging chamber (b) Droplet arrangement for different channel geometries. Image courtesy: Danny Raj and Raghunathan Rengaswamy, IIT Madras, India [207].

Our paper published in 2012 [208], motivated a research group to conduct numerical simulations [207] and proposed a modeling strategy to predict the dynamic pattern formation. The proposed model uses the forces experienced by the drops inside the microchannel through interacting drop-traffic model. Incorporating these models into a multi-agent simulation, the dynamic two-dimensional arrangements in the diverging/converging channel are simulated. The droplet arrangement is explored in four different geometries and they found that the low flat velocity at the midsection is an essential feature that aids the pattern formation.

6. Coalescence of droplets in a viscous medium

Understanding droplet coalescence is essential to describe the stability of emulsions and the dynamics of multiphase flow. This chapter focuses on the coalescence process at the individual level when two droplets merge in an external phase in the absence of surfactants. We experimentally examine the effect of viscosity of both droplet and external phases on the coalescence of droplets.

6.1. Experimental setup and fluid properties

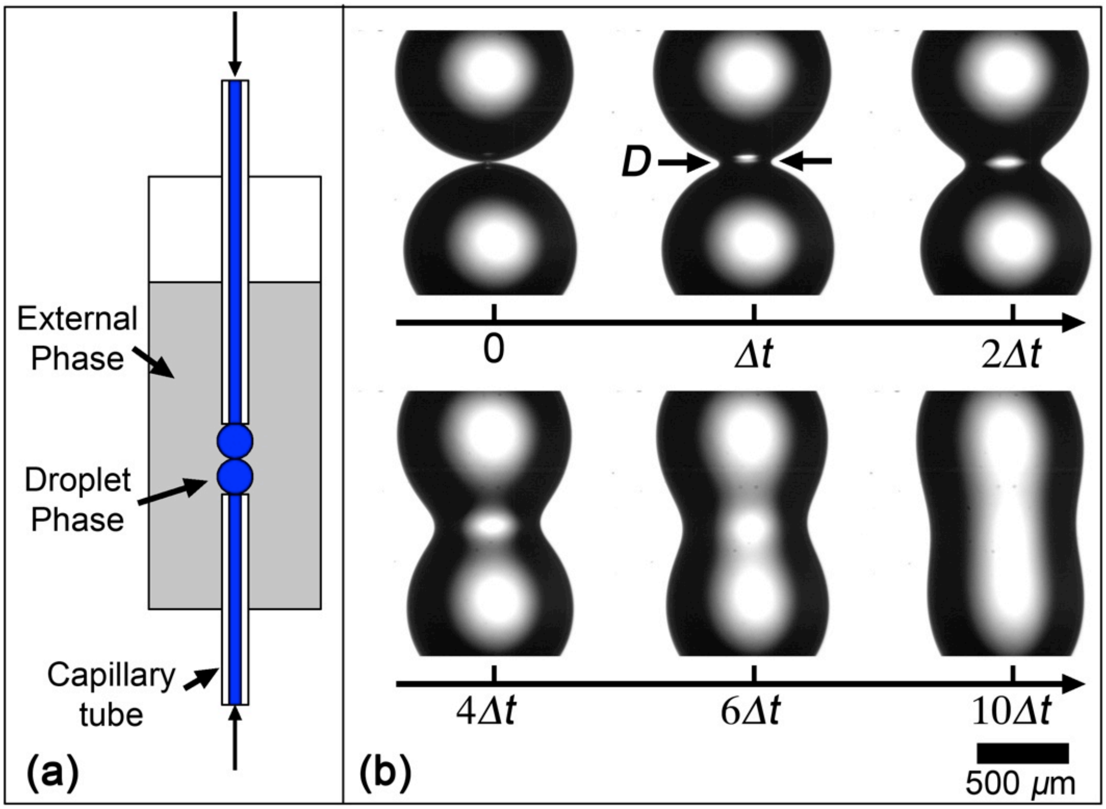

Figure 6.1 (a) Schematic of the cuvette where droplets coalesce. Droplet phase: Blue; External phase: Gray. (b) Time series of experimental micrographs of two droplets coalescing. $\Delta t = 2 \times 10^{-2}$s. Fluid Pair: W-10000cS

The experimental setup to visualize the droplet coalescence is given in Figure 2.2. The plastic cell in the experimental setup is replaced with a cuvette filled with external phase. Droplet phase is introduced into the external phase through two capillaries. By controlling the flow rates in small increments, a small droplet is suspended from the end of both capillaries. Droplets are then aligned to the same axis by adjusting the translating stage until the droplets starts to coalesce. As the droplets coalesce, a trigger is switched on to acquire the movie. The initial droplet diameter is kept between 0.8 and 2 mm, well below the capillary length.

Fluid Pair	Droplet Phase	η_1 (cP)	External Phase	η_2 (cP)	γ_{12} (mN/m)	B	Symbol
W-100cS	Water	1	PDMS	96.6	42.7	5.0×10^{-1}	◀
W-1000cS	-	-	-	971	42.7	6.5×10^{-2}	♦
W-10000cS	-	-	-	9740	42.7	2.0×10^{-2}	◆
G80-100cS	Glycerol-80%	36	-	96.6	29.7	1.2×10^{0}	◀
G80-1000cS	-	-	-	971	29.7	2.0×10^{-1}	♦
G80-10000cS	-	-	-	9740	29.7	1.8×10^{-2}	◆
G80-30000cS	-	-	-	29280	29.7	1.0×10^{-2}	◢
G92-100cS	Glycerol-92%	272	-	96.6	29.3	3.5×10^{-1}	◀
G92-1000cS	-	-	-	971	29.3	1.2×10^{-1}	♦
G92-10000cS	-	-	-	9740	29.3	1.8×10^{-2}	◆
G92-30000cS	-	-	-	29280	29.3	1.2×10^{-2}	◢
G99-100cS	Glycerol-99%	1275	-	96.6	27.7	2.5×10^{-1}	◀
G99-1000cS	-	-	-	971	27.7	9.0×10^{-2}	♦
G99-10000cS	-	-	-	9740	27.7	3.5×10^{-2}	◆
G99-30000cS	-	-	-	29280	27.7	6.5×10^{-3}	◢

Table 6-1 Properties of fluids used in the experiment and their symbols. G80 denotes 80% Glycerol by volume and W denotes Water. For example the fluid pair G80-1000cS indicates droplet phase is G80 and the external phase is ν_2 = 1000cS PDMS oil. Symbols are color-coded based on the droplet phase, Black: Water, Green: G80, Blue: G92, Red: G99.

6.2. Coalescence of droplets

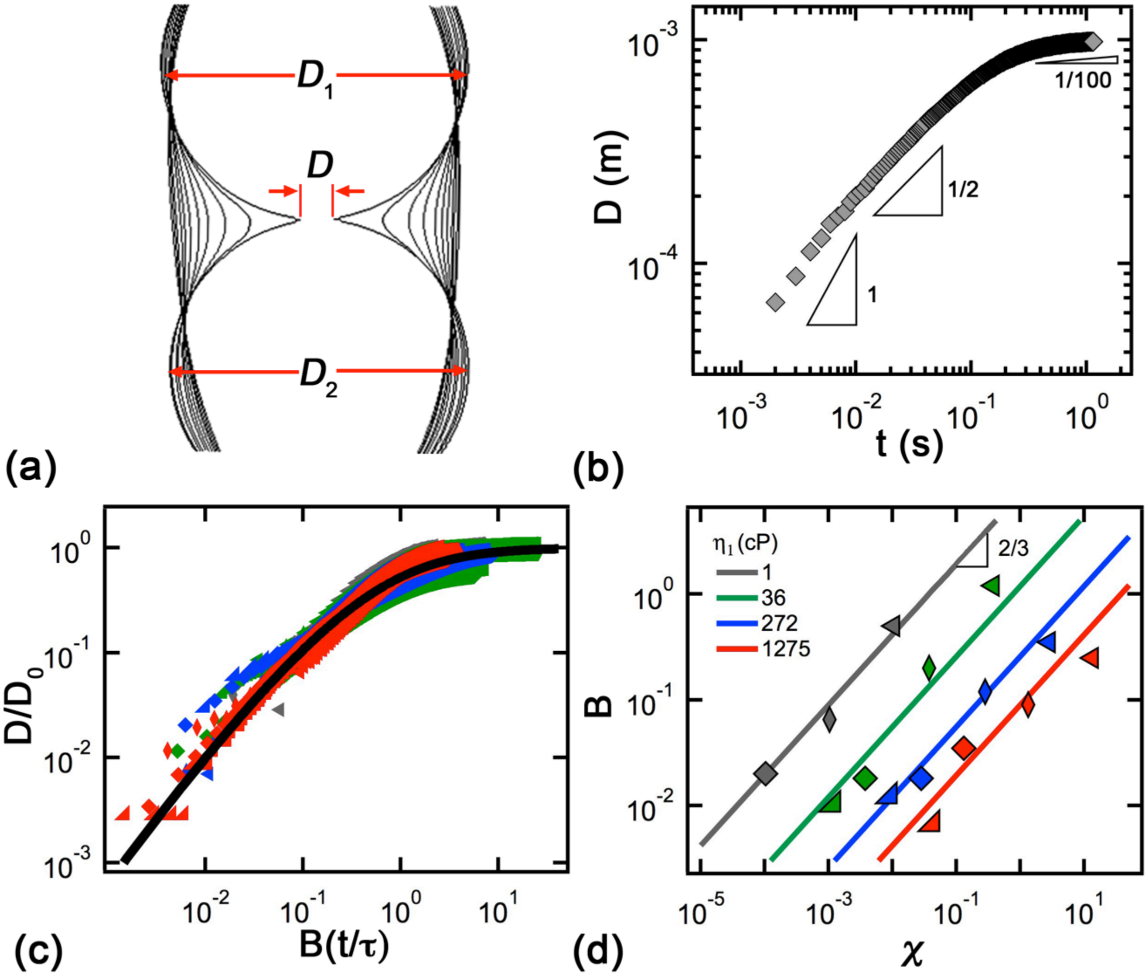

Figure 6.2 (a) Superimposed contours of the droplets to show the evolution of the liquid bridge D in time. Fluid pair: W-10000cS. (b) Diameter of the liquid bridge D vs. time t. (c) Diameter D/D_0 vs. time t/τ on a master curve after rescaling with the coefficient B. Solid Line: $(D/D_0)^{2/3} = (t/\tau)ln(D/D_0)$. (d) Coefficient B as a function of viscosity ratio χ for droplets of varying viscosities η_1. Solid line: $B = e\chi^{2/3}$ with $e = 9.0$ (grey), $e = 1.2$ (green), $e = 2.6 \times 10^{-1}$ (blue) and $e = 9 \times 10^{-2}$ (red).

When the two droplets come together, the thin film between them rupture and a liquid bridge is formed. The liquid bridge between the droplets grows by displacing the external phase radially outwards [Figure 6.2(a)]. The growth of the liquid bridge is extracted from the spatiotemporal diagrams and we plot the evolution of the diameter of the liquid bridge D as a function of time t. The liquid bridge grows with time as $D \sim t^{\alpha}$ with α progressively decreasing in time [Figure 6.2(b)]. Eddi *et al*. [141] have investigated the influence of α to give a functional form for the evolution of spreading diameter in droplet spreading experiments. We found that a modified version of this function can describe evolution of liquid bridge of the coalescing droplets and is given in equation (6.1). The diameter D is normalized by initial mean diameter of the droplet as $D_0 = (D_1+D_2)/2$ and time t by inertial timescale $\tau = (\Delta\rho D_0^3/\gamma_{12})^{1/2}$. All the evolution curves can be collapsed on a master curve after rescaling with a coefficient B and can be described by [Figure 6.2(c)],

$$\left(\frac{D}{D_0}\right)^{2/3} = -B\frac{t}{\tau}\boldsymbol{ln}\left(\frac{D}{D_0}\right) \qquad (6.1)$$

The coefficient B in the equation (6.1) carries the dependency on the viscosity and scales with viscosity ratio as $B = e\chi^{2/3}$ [Figure 6.2(d)] with $e = f(\eta_1)$. The magnitude of the coefficient B is a relative measure of the time scale of coalescence. A higher value for B represents faster coalescence and a smaller timescale.

6.3. Comparison of coalescence with spreading.

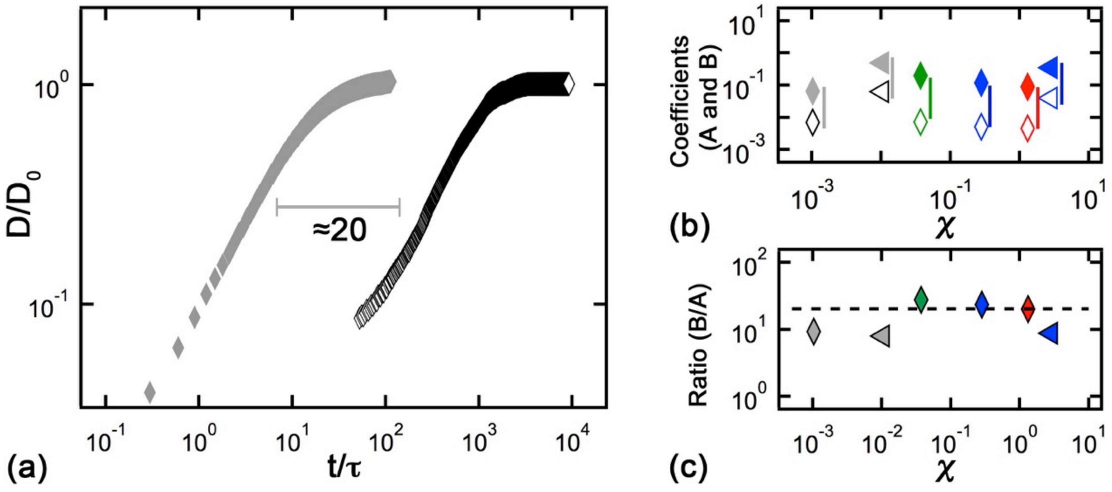

Figure 6.3 (a) Comparison of coalescence and spreading Fluid Pair: W-1000cS. (b) Coefficient for spreading A (open symbols) and coalescence B (filled symbols) is plotted together as a function of viscosity ratio χ. The bar represents a magnitude of 20. (c) Ratio of coefficients B/A vs. viscosity ratio χ. Dotted Line: $B/A = 20$.

The spreading process can be seen as the coalescence of a droplet on solid wall and a direct comparison can be drawn with droplet coalescence. As expected the droplets coalesce at shorter timescales with the absence of contact line. To draw a direct comparison, evolution of liquid bridge is plotted alongside the evolution of spreading diameter as a function of time [Figure 6.3(a)]. The two curves have similar shape showed fast power law regime followed by a slow relaxation regime. The relaxation regime of the drop coalescence is shortened by the distance between the end of capillaries from where droplets are suspended. By plotting together the coefficient for spreading A and coalescence B, we can draw a direct comparison of two processes. Since both coefficients indicate the magnitude of speed of coalescence, their ratio B/A will give a comparison of spreading and coalescence. Our data suggest the coalescence coefficient B is 20 times larger than spreading coefficient A with $B/A \approx 20$. For all the combinations of fluid pairs with different viscosities investigated, coalescence is found to be around 20 times faster than spreading process [Figure 6.3(c)]. We attribute the difference to the absence of a contact line in coalescence process.

6.4. Conclusion

We found that the evolution of the liquid bridge followed a similar trend across different fluid pairs similar to droplet spreading and can be described by a functional form. All the evolution curves are collapsed to a single master curve using a coefficient B. The viscous effects of both droplet and external phase are captured in this coefficient B. A direct comparison between droplet spreading and coalescence is drawn by taking the ratio of two coefficient A and B. Our results suggest that droplets coalesce on a shorter timescale in the absence of contact line and is almost 20 times faster than the spreading process.

7. Conclusion

The principal contribution of this thesis is the identification of control parameters for various flow regimes and classification of the rich dynamics of droplets in microgeometries. We have shown that the dynamic and physical properties of fluids can be used as useful parameter to characterize flows in microchannels. To determine these properties we designed an immersed droplet spreading experiment. The spreading process showed two regimes: fast power law regime and a slow relaxation regime. In a highly damped viscous medium, we showed that the time to reach complete equilibrium can be quite long (up to 33 days) with very large relaxation times. Although inertia capillary balance describes the short-term dynamics of spreading process, we noticed an additional dependency on the viscosity of the droplet and external phase. Defining a coefficient *A*, which is essentially a magnitude of the speed of spreading process, captures this dependency. A key observation is that viscosity ratio alone cannot fully describe the spreading process as the absolute viscosity significantly influence the spreading curves. We also found that the crossover from fast exponential to slow relaxation regimes depends on the viscosity of the droplet and external phase. Again, this crossover is much smoother with increasing viscosity of either phase. For slow relaxation regimes the evolution of the contact angle should be seen as a function of contact line velocity. Advancing critical velocities scale with capillary velocity and summarize all the evolution of the curves for contact angle. We also propose an effective viscosity for the two-phase system based on MKT theory. Overall in a two-fluid case, we showed that the influence of either fluid could not be neglected in determining rate of spreading process. We also compared the spreading process with droplet coalescence and found that the droplets coalesce at much shorter timescale in the absence of a contact line.

Dynamic spreading properties of fluids can be used to classify the different regimes of forced wetting transitions in microchannels. Especially we show that the dynamic advancing angle is a useful parameter to predict and control wetting transitions of segmented flows. An array of different wetting transitions for a partially wetting system in microchannel has been discussed such as the dewetting of the thin film, stick-slip movement of droplets encountering the surface heterogeneities and the inclination of the dewetting line to form saw tooth–like configurations near the rear of the droplet. We identified two modes of droplet formation in the hysteretic partially wetting systems for similar injection parameters, namely dripping and rivulet. Although the droplet size in the dripping regime is given by the emulsion concentration, there is a contrasting influence of capillary number at different regimes based on thin film. Despite the variation in droplet size, the linear aspect ratio of the multiphase flow remains independent of the capillary number and is fixed by the flow rate ratio.

Viscous droplets dynamically self-assemble in a diverging/converging slit microchamber to form closely packed crystal-like structures. The collective dynamics of hydrodynamically coupled droplets is determined by the aspect ratio of the inlet droplet train and the geometry of the microchannel. We compared the close packing arrangements with a continuous fluid stream using the maximal amplitude at the middle of the chamber. The viscosity of the external phase and the droplet concentration determines the stability of the self-assembled structures. In another experiment, we show that coalescence time scales with the capillary time scale. Overall, our study of droplets highlights the interplay between hydrodynamics, coalescence and wetting and we have successfully quantified the behavior of capillary interfaces under confinement.

7.1. Future Directions

We have presented a comprehensive study on the behavior of jammed fluid interfaces in micro geometries. A large number of studies in microfluidics try to avoid contact line formation and the coalescence is studied at individual level on microfluidic platforms. Often, the hysteretic nature of micro flows is an area of concern for reliability of microfluidics platforms. We have addressed these complex problems at most fundamental level and shown how microfluidics can be used to understand wetting transitions and coalescence in emulsions. We expect our studies will open new avenues for interdisciplinary research and creation of new applications, which can leverage the knowledge generated through this study.

Bibliography

[1] Tabeling, P., *Introduction to Microfluidics*. 2005: Oxford University Press.

[2] Dittrich, P.S. and A. Manz, Lab-on-a-chip: microfluidics in drug discovery. *Nat Rev Drug Discov*,2006. 5(3): 210-8.

[3] Fair, R.B., A. Khlystov, T.D. Tailor, V. Ivanov, R.D. Evans, V. Srinivasan, V.K. Pamula, M.G. Pollack, P.B. Griffin, and J. Zhou, Chemical and Biological Applications of Digital-Microfluidic Devices. *IEEE Design & Test of Computers*,2007. 24(1): 10-24.

[4] Whitesides, G.M., The origins and the future of microfluidics. *Nature*,2006. 442(7101): 368-73.

[5] Weibel, D.B. and G.M. Whitesides, Applications of microfluidics in chemical biology. *Curr Opin Chem Biol*,2006. 10(6): 584-91.

[6] DeMello, A.J., Control and detection of chemical reactions in microfluidic systems. *Nature*,2006. 442(7101): 394-402.

[7] Erickson, D. and D. Li, Integrated microfluidic devices. *Analytica Chimica Acta*,2004. 507(1): 11-26.

[8] Easley, C.J., J.M. Karlinsey, J.M. Bienvenue, L.A. Legendre, M.G. Roper, S.H. Feldman, M.A. Hughes, E.L. Hewlett, T.J. Merkel, J.P. Ferrance, and J.P. Landers, A fully integrated microfluidic genetic analysis system with sample-in-answer-out capability. *Proc Natl Acad Sci U S A*,2006. 103(51): 19272-7.

[9] Chabinyc, M.L., D.T. Chiu, J.C. McDonald, A.D. Stroock, J.F. Christian, A.M. Karger, and G.M. Whitesides, An Integrated Fluorescence Detection System in Poly(dimethylsiloxane) for Microfluidic Applications. *Analytical Chemistry*,2001. 73(18): 4491-4498.

[10] Thorsen, T., S.J. Maerkl, and S.R. Quake, Microfluidic large-scale integration. *Science*,2002. 298(5593): 580-4.

[11] Balagadde, F.K., L. You, C.L. Hansen, F.H. Arnold, and S.R. Quake, Long-term monitoring of bacteria undergoing programmed population control in a microchemostat. *Science*,2005. 309(5731): 137-40.

[12] Cubaud, T. and T.G. Mason, A microfluidic aquarium. *Physics of Fluids*,2007. 19(9): 091108.

[13] Groisman, A. and V.V. Steinberg, Elastic turbulence in a polymer solution flow. *Nature*,2000. 405(6782): 53-5.

[14] Basova, E.Y. and F. Foret, Droplet microfluidics in (bio)chemical analysis. *Analyst*,2014. 10.1039/c4an01209g.

[15] Kim, S.H., S.Y. Lee, G.R. Yi, D.J. Pine, and S.M. Yang, Microwave-assisted self-organization of colloidal particles in confining aqueous droplets. *J Am Chem Soc*,2006. 128(33): 10897-904.

[16] Adams, L.L.A., T.E. Kodger, S.-H. Kim, H.C. Shum, T. Franke, and D.A. Weitz, Single step emulsification for the generation of multi-component double emulsions. *Soft Matter*,2012. 8(41): 10719.

[17] Khan, S.A. and K.F. Jensen, Microfluidic synthesis of titania shells on colloidal silica. *Advanced Materials*,2007. 19(18): 2556.

[18] Murray, C.B., C.R. Kagan, and M.G. Bawendi, Synthesis and characterization of monodisperse nanocrystals and close-packed nanocrystal assemblies. *Annual Review of Materials Science*,2000. 30(1): 545-610.

[19] Theberge, A.B., F. Courtois, Y. Schaerli, M. Fischlechner, C. Abell, F. Hollfelder, and W.T. Huck, Microdroplets in microfluidics: an evolving platform for discoveries in chemistry and biology. *Angew Chem Int Ed Engl*,2010. 49(34): 5846-68.

[20] Agresti, J.J., E. Antipov, A.R. Abate, K. Ahn, A.C. Rowat, J.C. Baret, M. Marquez, A.M. Klibanov, A.D. Griffiths, and D.A. Weitz, Ultrahigh-throughput screening in drop-based microfluidics for directed evolution. *Proc Natl Acad Sci U S A*,2010. 107(9): 4004-9.

[21] Edd, J.F., D. Di Carlo, K.J. Humphry, S. Koster, D. Irimia, D.A. Weitz, and M. Toner, Controlled encapsulation of single-cells into monodisperse picolitre drops. *Lab Chip*,2008. 8(8): 1262-4.

[22] McClain, M.A., C.T. Culbertson, S.C. Jacobson, N.L. Allbritton, C.E. Sims, and J.M. Ramsey, Microfluidic devices for the high-throughput chemical analysis of cells. *Anal Chem*,2003. 75(21): 5646-55.

[23] Handique, K. and M.A. Burns, Mathematical modeling of drop mixing in a slit-type microchannel. *Journal of Micromechanics and Microengineering*,2001. 11(5): 548-554.

[24] Song, H., M.R. Bringer, J.D. Tice, C.J. Gerdts, and R.F. Ismagilov, Experimental test of scaling of mixing by chaotic advection in droplets moving through microfluidic channels. *Appl Phys Lett*,2003. 83(12): 4664-4666.

[25] Tan, Y.-C., Y.L. Ho, and A.P. Lee, Droplet coalescence by geometrically mediated flow in microfluidic channels. *Microfluidics and Nanofluidics*,2006. 3(4): 495-499.

[26] Fidalgo, L.M., C. Abell, and W.T. Huck, Surface-induced droplet fusion in microfluidic devices. *Lab Chip*,2007. 7(8): 984-6.

[27] Hung, L.H., K.M. Choi, W.Y. Tseng, Y.C. Tan, K.J. Shea, and A.P. Lee, Alternating droplet generation and controlled dynamic droplet fusion in microfluidic device for CdS nanoparticle synthesis. *Lab Chip*,2006. 6(2): 174-8.

[28] Frenz, L., A. El Harrak, M. Pauly, S. Begin-Colin, A.D. Griffiths, and J.C. Baret, Droplet-based microreactors for the synthesis of magnetic iron oxide nanoparticles. *Angew Chem Int Ed Engl*,2008. 47(36): 6817-20.

[29] Zheng, B., L.S. Roach, and R.F. Ismagilov, Screening of protein crystallization conditions on a microfluidic chip using nanoliter-size droplets. *Journal of the American Chemical Society*,2003. 125(37): 11170-11171.

[30] RainDance Technologies, I., *RainDrop™ Digital PCR System*, I. RainDance Technologies, Editor. 2014, RainDance Technologies, Inc.: USA.

[31] Brouzes, E., M. Medkova, N. Savenelli, D. Marran, M. Twardowski, J.B. Hutchison, J.M. Rothberg, D.R. Link, N. Perrimon, and M.L. Samuels, Droplet microfluidic technology for single-cell high-throughput screening. *Proc Natl Acad Sci U S A*,2009. 106(34): 14195-200.

[32] Clausell-Tormos, J., D. Lieber, J.C. Baret, A. El-Harrak, O.J. Miller, L. Frenz, J. Blouwolff, K.J. Humphry, S. Koster, H. Duan, C. Holtze, D.A. Weitz, A.D. Griffiths, and C.A. Merten, Droplet-based microfluidic platforms for the encapsulation and screening of Mammalian cells and multicellular organisms. *Chem Biol*,2008. 15(5): 427-37.

[33] Ge, S., W. Liu, T. Schlappi, and R.F. Ismagilov, Digital, Ultrasensitive, End-Point Protein Measurements with Large Dynamic Range via Brownian Trapping with Drift. *J Am Chem Soc*,2014. 136(42): 14662-5.

[34] Boukellal, H., S. Selimovic, Y. Jia, G. Cristobal, and S. Fraden, Simple, robust storage of drops and fluids in a microfluidic device. *Lab Chip*,2009. 9(2): 331-8.

[35] Huebner, A., D. Bratton, G. Whyte, M. Yang, A.J. Demello, C. Abell, and F. Hollfelder, Static microdroplet arrays: a microfluidic device for droplet trapping,

incubation and release for enzymatic and cell-based assays. *Lab Chip*,2009. 9(5): 692-8.

[36] Holtze, C., A.C. Rowat, J.J. Agresti, J.B. Hutchison, F.E. Angile, C.H. Schmitz, S. Koster, H. Duan, K.J. Humphry, R.A. Scanga, J.S. Johnson, D. Pisignano, and D.A. Weitz, Biocompatible surfactants for water-in-fluorocarbon emulsions. *Lab Chip*,2008. 8(10): 1632-9.

[37] Wang, M.M., E. Tu, D.E. Raymond, J.M. Yang, H. Zhang, N. Hagen, B. Dees, E.M. Mercer, A.H. Forster, I. Kariv, P.J. Marchand, and W.F. Butler, Microfluidic sorting of mammalian cells by optical force switching. *Nat Biotechnol*,2005. 23(1): 83-7.

[38] Koster, S., F.E. Angile, H. Duan, J.J. Agresti, A. Wintner, C. Schmitz, A.C. Rowat, C.A. Merten, D. Pisignano, A.D. Griffiths, and D.A. Weitz, Drop-based microfluidic devices for encapsulation of single cells. *Lab Chip*,2008. 8(7): 1110-5.

[39] Franke, T., A.R. Abate, D.A. Weitz, and A. Wixforth, Surface acoustic wave (SAW) directed droplet flow in microfluidics for PDMS devices. *Lab Chip*,2009. 9(18): 2625-7.

[40] Ahn, K., C. Kerbage, T.P. Hunt, R.M. Westervelt, D.R. Link, and D.A. Weitz, Dielectrophoretic manipulation of drops for high-speed microfluidic sorting devices. *Applied Physics Letters*,2006. 88(2): 024104.

[41] Selva, B., V. Miralles, I. Cantat, and M.C. Jullien, Thermocapillary actuation by optimized resistor pattern: bubbles and droplets displacing, switching and trapping. *Lab Chip*,2010. 10(14): 1835-40.

[42] Baret, J.C., O.J. Miller, V. Taly, M. Ryckelynck, A. El-Harrak, L. Frenz, C. Rick, M.L. Samuels, J.B. Hutchison, J.J. Agresti, D.R. Link, D.A. Weitz, and A.D. Griffiths, Fluorescence-activated droplet sorting (FADS): Efficient microfluidic cell sorting based on enzymatic activity. *Lab Chip*,2009. 9(13): 1850-8.

[43] Mary, P., V. Studer, and P. Tabeling, Microfluidic droplet-based liquid-liquid extraction. *Analytical Chemistry*,2008. 80(8): 2680-2687.

[44] Burns, J.R. and C. Ramshaw, The intensification of rapid reactions in multiphase systems using slug flow in capillaries. *Lab Chip*,2001. 1(1): 10-5.

[45] Dreyfus, R., P. Tabeling, and H. Willaime, Ordered and disordered patterns in two-phase flows in microchannels. *Phys Rev Lett*,2003. 90(14): 144505.

[46] Piorek, B.D., S.J. Lee, M. Moskovits, and C.D. Meinhart, Free-surface microfluidics/surface-enhanced Raman spectroscopy for real-time trace vapor detection of explosives. *Anal Chem*,2012. 84(22): 9700-5.

[47] Olbricht, W.L., Pore-Scale Prototypes of Multiphase Flow in Porous Media. *Annual Review of Fluid Mechanics*,1996. 28(1): 187-213.

[48] de Haas, T.W., H. Fadaei, U. Guerrero, and D. Sinton, Steam-on-a-chip for oil recovery: the role of alkaline additives in steam assisted gravity drainage. *Lab Chip*,2013. 13(19): 3832-9.

[49] Berejnov, V., N. Djilali, and D. Sinton, Lab-on-chip methodologies for the study of transport in porous media: energy applications. *Lab Chip*,2008. 8(5): 689-93.

[50] Kim, M., A. Sell, and D. Sinton, Aquifer-on-a-chip: understanding pore-scale salt precipitation dynamics during CO2 sequestration. *Lab Chip*,2013. 13(13): 2508-18.

[51] Karadimitriou, N.K., V. Joekar-Niasar, S.M. Hassanizadeh, P.J. Kleingeld, and L.J. Pyrak-Nolte, A novel deep reactive ion etched (DRIE) glass micro-model for two-phase flow experiments. *Lab Chip*,2012. 12(18): 3413-8.

[52] Bear, J., *Dynamics of fluids in porous media*. 1972: Courier Dover Publications.

[53] Willingham, T.W., C.J. Werth, and A.J. Valocchi, Evaluation of the Effects of Porous Media Structure on Mixing-Controlled Reactions Using Pore-Scale Modeling and Micromodel Experiments. *Environmental Science & Technology*,2008. 42(9): 3185-3193.

[54] Shahidzadeh-Bonn, N., A. Tournie, S. Bichon, P. Vie, S. Rodts, P. Faure, F. Bertrand, and A. Azouni, Effect of wetting on the dynamics of drainage in porous media. *Transport in Porous Media*,2004. 56(2): 209-224.

[55] Ouali, F.F., G. McHale, H. Javed, C. Trabi, N.J. Shirtcliffe, and M.I. Newton, Wetting considerations in capillary rise and imbibition in closed square tubes and open rectangular cross-section channels. *Microfluidics and Nanofluidics*,2013. 15(3): 309-326.

[56] Jose, B.M. and T. Cubaud, Formation and dynamics of partially wetting droplets in square microchannels. *RSC Advances*,2014. 4(29): 14962.

[57] Christopher, G.F. and S.L. Anna, Microfluidic methods for generating continuous droplet streams. *Journal of Physics D-Applied Physics*,2007. 40(19): R319-R336.

[58] Cubaud, T. and T.G. Mason, Capillary threads and viscous droplets in square microchannels. *Physics of Fluids*,2008. 20(5).

[59] Herrada, M.A., A.M. Ganan-Calvo, and J.M. Montanero, Theoretical investigation of a technique to produce microbubbles by a microfluidic T junction. *Phys Rev E Stat Nonlin Soft Matter Phys*,2013. 88(3): 033027.

[60] Squires, T.M. and S.R. Quake, Microfluidics: Fluid physics at the nanoliter scale. *Reviews of Modern Physics*,2005. 77(3): 977-1026.

[61] Sugiura, S., M. Nakajima, S. Iwamoto, and M. Seki, Interfacial tension driven monodispersed droplet formation from microfabricated channel array. *Langmuir*,2001. 17(18): 5562-5566.

[62] Utada, A.S., E. Lorenceau, D.R. Link, P.D. Kaplan, H.A. Stone, and D.A. Weitz, Monodisperse double emulsions generated from a microcapillary device. *Science*,2005. 308(5721): 537-541.

[63] Castro-Hernandez, E., W. van Hoeve, D. Lohse, and J.M. Gordillo, Microbubble generation in a co-flow device operated in a new regime. *Lab Chip*,2011. 11(12): 2023-9.

[64] Ward, T., M. Faivre, and H.A. Stone, Drop production and tip-streaming phenomenon in a microfluidic flow-focusing device via an interfacial chemical reaction. *Langmuir*,2010. 26(12): 9233-9.

[65] Garstecki, P., H. Stone, and G. Whitesides, Mechanism for Flow-Rate Controlled Breakup in Confined Geometries: A Route to Monodisperse Emulsions. *Physical Review Letters*,2005. 94(16).

[66] Teh, S.Y., R. Lin, L.H. Hung, and A.P. Lee, Droplet microfluidics. *Lab Chip*,2008. 8(2): 198-220.

[67] Purcell, E.M., Life at Low Reynolds-Number. *American Journal of Physics*,1977. 45(1): 3-11.

[68] Bruus, H., *Theoretical Microfluidics*. illustrated, reprint ed. 2007: OUP Oxford.

[69] Bonn, D., J. Eggers, J. Indekeu, J. Meunier, and E. Rolley, Wetting and spreading. *Reviews of Modern Physics*,2009. 81(2): 739-805.

[70] Degennes, P.G., Wetting - Statics and Dynamics. *Reviews of Modern Physics*,1985. 57(3): 827-863.

[71] Pászli, I., I. Mohammed-Ziegler, and Z. Hórvölgyi, Obtaining surface tension from contact angle data by the individual representation approach. *Colloid and Polymer Science*,2007. 285(9): 1009-1018.

[72] Young, T., An Essay on the Cohesion of Fluids. *Philosophical Transactions of the Royal Society of London*,1805. 95: 65-87.

[73] Kavehpour, H., B. Ovryn, and G. McKinley, Microscopic and Macroscopic Structure of the Precursor Layer in Spreading Viscous Drops. *Physical Review Letters*,2003. 91(19).

[74] Cox, R.G., The Dynamics of the Spreading of Liquids on a Solid-Surface .1. Viscous-Flow. *Journal of Fluid Mechanics*,1986. 168: 169-194.

[75] Voinov, O.V., Hydrodynamics of wetting. *Fluid Dynamics*,1976. 11(7): 714-721.

[76] Adamson, A.W. and T.A. Adamson, *Physical Chemistry of Surfaces*. 4 ed. 1990: John Wiley & Sons.

[77] Le Grand-Piteira, N., *Flow with wetting effects: Drops and meanders on an inclined plane*, in *Department of Physics*. 2006, Universit Paris-Diderot - Paris VII.

[78] Cox, R.G., Inertial and viscous effects on dynamic contact angles. *Journal of Fluid Mechanics*,1998. 357: 249-278.

[79] Huh, C. and L.E. Scriven, Hydrodynamic model of steady movement of a solid/liquid/fluid contact line. *Journal of Colloid and Interface Science*,1971. 35(1): 85-101.

[80] Snoeijer, J.H. and B. Andreotti, Moving Contact Lines: Scales, Regimes, and Dynamical Transitions. *Annual Review of Fluid Mechanics*,2013. 45(1): 269-292.

[81] Eggers, J., Existence of receding and advancing contact lines. *Physics of Fluids*,2005. 17(8): 082106.

[82] Berg, J., *Wettability*. Vol. 49. 1993: Taylor & Francis.

[83] Rio, E. and L. Limat, Wetting hysteresis of a dry patch left inside a flowing film. *Physics of Fluids*,2006. 18(3): 032102.

[84] Winkels, K.G., I.R. Peters, F. Evangelista, M. Riepen, A. Daerr, L. Limat, and J.H. Snoeijer, Receding contact lines: From sliding drops to immersion lithography. *The European Physical Journal Special Topics*,2011. 192(1): 195-205.

[85] Eggers, J., Toward a description of contact line motion at higher capillary numbers. *Physics of Fluids*,2004. 16(9): 3491-3494.

[86] Hocking, L.M., A moving fluid interface on a rough surface. *Journal of Fluid Mechanics*,2006. 76(04): 801.

[87] Delon, G., *On the Landau Levich transition*. 2006, Université de Paris 7, France.

[88] Le Grand, N., A. Daerr, and L. Limat, Shape and motion of drops sliding down an inclined plane. *Journal of Fluid Mechanics*,2005. 541: 293-315.

[89] Podgorski, T., J.M. Flesselles, and L. Limat, Corners, Cusps, and Pearls in Running Drops. *Physical Review Letters*,2001. 87(3): 036102(4).

[90] Eggers, J., Hydrodynamic Theory of Forced Dewetting. *Physical Review Letters*,2004. 93(9).

[91] Snoeijer, J., G. Delon, M. Fermigier, and B. Andreotti, Avoided Critical Behavior in Dynamically Forced Wetting. *Physical Review Letters*,2006. 96(17).

[92] Chan, T.S., J.H. Snoeijer, and J. Eggers, Theory of the forced wetting transition. *Physics of Fluids*,2012. 24(7): 072104.

[93] Marchand, A., T.S. Chan, J.H. Snoeijer, and B. Andreotti, Air Entrainment by Contact Lines of a Solid Plate Plunged into a Viscous Fluid. *Physical Review Letters*,2012. 108(20).

[94] Snoeijer, J.H., E. Rio, N. Le Grand, and L. Limat, Self-similar flow and contact line geometry at the rear of cornered drops. *Physics of Fluids*,2005. 17(7): 072101.

[95] Blake, T. and K. Ruschak, A maximum speed of wetting. *Nature*,1979. 282.

[96] Abismaïl, B., J.P. Canselier, A.M. Wilhelm, H. Delmas, and C. Gourdon, Emulsification by ultrasound: drop size distribution and stability. *Ultrasonics Sonochemistry*,1999. 6(1-2): 75-83.

[97] Tcholakova, S., N.D. Denkov, I.B. Ivanov, and B. Campbell, Coalescence stability of emulsions containing globular milk proteins. *Adv Colloid Interface Sci*,2006. 123-126: 259-93.

[98] Thümmler, F. and W. Thomma, The sintering process. *Metallurgical Reviews*,1967. 12(1): 69-108.

[99] Tcholakova, S., N.D. Denkov, I.B. Ivanov, and B. Campbell, Coalescence in β-Lactoglobulin-Stabilized Emulsions: Effects of Protein Adsorption and Drop Size. *Langmuir*,2002. 18(23): 8960-8971.

[100] van Aken, G.A. and T. van Vliet, Flow-Induced Coalescence in Protein-Stabilized Highly Concentrated Emulsions: Role of Shear-Resisting Connections between the Droplets. *Langmuir*,2002. 18(20): 7364-7370.

[101] Leal-Calderon, F., V. Schmitt, and J. Bibette, *Emulsion Science: Basic Principles*. 2007: Springer.

[102] Leal, L.G., Flow induced coalescence of drops in a viscous fluid. *Physics of Fluids*,2004. 16(6): 1833.

[103] Bremond, N., H. Doméjean, and J. Bibette, Propagation of Drop Coalescence in a Two-Dimensional Emulsion: A Route towards Phase Inversion. *Physical Review Letters*,2011. 106(21).

[104] Gunes, D.Z., M. Bercy, B. Watzke, O. Breton, and A.S. Burbidge, A study of extensional flow induced coalescence in microfluidic geometries with lateral channels. *Soft Matter*,2013. 9(31): 7526.

[105] Bremond, N., A. Thiam, and J. Bibette, Decompressing Emulsion Droplets Favors Coalescence. *Physical Review Letters*,2008. 100(2).

[106] Lai, A.N.N., N. Bremond, and H.A. Stone, Separation-driven coalescence of droplets: an analytical criterion for the approach to contact. *Journal of Fluid Mechanics*,2009. 632: 97.

[107] Thoroddsen, S.T., K. Takehara, and T.G. Etoh, The coalescence speed of a pendent and a sessile drop. *Journal of Fluid Mechanics*,2005. 527: 85-114.

[108] Menchaca-Rocha, A., A. Martínez-Dávalos, R. Núñez, S. Popinet, and S. Zaleski, Coalescence of liquid drops by surface tension. *Physical Review E*,2001. 63(4).

[109] Lee, M.W., N.Y. Kim, S. Chandra, and S.S. Yoon, Coalescence of sessile droplets of varying viscosities for line printing. *International Journal of Multiphase Flow*,2013. 56: 138-148.

[110] Eggers, J., J.R. Lister, and H.A. Stone, Coalescence of liquid drops. *Journal of Fluid Mechanics*,1999. 401: 293-310.

[111] Duchemin, L., J. Eggers, and C. Josserand, Inviscid coalescence of drops. *Journal of Fluid Mechanics*,2003. 487: 167-178.

[112] Yokota, M. and K. Okumura, Dimensional crossover in the coalescence dynamics of viscous drops confined in between two plates. *Proceedings of the National Academy of Sciences*,2011. 108(16): 6395-6398.

[113] Aarts, D.G., H.N. Lekkerkerker, H. Guo, G.H. Wegdam, and D. Bonn, Hydrodynamics of droplet coalescence. *Phys Rev Lett*,2005. 95(16): 164503.

[114] Yao, W., H.J. Maris, P. Pennington, and G.M. Seidel, Coalescence of viscous liquid drops. *Physical Review E*,2005. 71(1).

[115] Paulsen, J.D., J.C. Burton, and S.R. Nagel, Viscous to Inertial Crossover in Liquid Drop Coalescence. *Physical Review Letters*,2011. 106(11).

[116] Wu, M., T. Cubaud, and C.-M. Ho, Scaling law in liquid drop coalescence driven by surface tension. *Physics of Fluids*,2004. 16(7): L51.

[117] Lu, T.X., J.W. Biggar, and D.R. Nielsen, Water-Movement in Glass Bead Porous-Media .1. Experiments of Capillary Rise and Hysteresis. *Water Resources Research*,1994. 30(12): 3275-3281.

[118] Pan, C., M. Hilpert, and C.T. Miller, Lattice-Boltzmann simulation of two-phase flow in porous media. *Water Resources Research*,2004. 40(1).

[119] Basu, S., K. Nandakumar, and J.H. Masliyah, A study of oil displacement on model surfaces. *Journal of Colloid and Interface Science*,1996. 182(1): 82-94.

[120] Morrow, N., I. Chatzis, and J. Taber, Entrapment and mobilization of residual oil in bead packs. *SPE Reservoir Engineering*,1988. 3(3): 927-934.

[121] dos Santos, R.G., R.S. Mohamed, A.C. Bannwart, and W. Loh, Contact angle measurements and wetting behavior of inner surfaces of pipelines exposed to heavy crude oil and water. *Journal of Petroleum Science and Engineering*,2006. 51(1-2): 9-16.

[122] Freer, E.M., T. Svitova, and C.J. Radke, The role of interfacial rheology in reservoir mixed wettability. *Journal of Petroleum Science and Engineering*,2003. 39(1-2): 137-158.

[123] Kocherginsky, N.M., C.L. Tan, and W.F. Lu, Demulsification of water-in-oil emulsions via filtration through a hydrophilic polymer membrane. *Journal of Membrane Science*,2003. 220(1-2): 117-128.

[124] Lee, C.H., N. Johnson, J. Drelich, and Y.K. Yap, The performance of superhydrophobic and superoleophilic carbon nanotube meshes in water-oil filtration. *Carbon*,2011. 49(2): 669-676.

[125] Shi, Z., W. Zhang, F. Zhang, X. Liu, D. Wang, J. Jin, and L. Jiang, Ultrafast separation of emulsified oil/water mixtures by ultrathin free-standing single-walled carbon nanotube network films. *Adv Mater*,2013. 25(17): 2422-7.

[126] Litster, S., D. Sinton, and N. Djilali, Ex situ visualization of liquid water transport in PEM fuel cell gas diffusion layers. *Journal of Power Sources*,2006. 154(1): 95-105.

[127] Anna, S.L., N. Bontoux, and H.A. Stone, Formation of dispersions using “flow focusing” in microchannels. *Applied Physics Letters*,2003. 82(3): 364.

[128] Garstecki, P., M.J. Fuerstman, H.A. Stone, and G.M. Whitesides, Formation of droplets and bubbles in a microfluidic T-junction-scaling and mechanism of break-up. *Lab Chip*,2006. 6(3): 437-46.

[129] Eggers, J., Drop formation - an overview. *Zamm*,2005. 85(6): 400-410.

[130] Blake, T.D., The physics of moving wetting lines. *J Colloid Interface Sci*,2006. 299(1): 1-13.

[131] Blake, T.D. and Y.D. Shikhmurzaev, Dynamic wetting by liquids of different viscosity. *J Colloid Interface Sci*,2002. 253(1): 196-202.

[132] Cubaud, T., M. Fermigier, and P. Jenffer, Spreading of large drops on patterned surfaces. *Oil & Gas Science and Technology-Revue D Ifp Energies Nouvelles*,2001. 56(1): 23-31.

[133] Bonn, D., D. Ross, E. Bertrand, K. Ragil, N. Shahidzadeh, D. Broseta, and J. Meunier, Wetting transitions. *Physica A: Statistical Mechanics and its Applications*,2002. 306: 279-286.

[134] Bertrand, E., D. Bonn, D. Broseta, H. Dobbs, J.O. Indekeu, J. Meunier, K. Ragil, and N. Shahidzadeh, Wetting of alkanes on water. *Journal of Petroleum Science and Engineering*,2002. 33(1-3): 217-222.

[135] Bergeron, V.V., D. Bonn, J.Y. Martin, and L. Vovelle, Controlling droplet deposition with polymer additives. *Nature*,2000. 405(6788): 772-5.

[136] Shahidzadeh, N., E. Bertrand, J.P. Dauplait, J.C. Borgotti, P. Vie, and D. Bonn, Effect of wetting on gravity drainage in porous media. *Transport in Porous Media*,2003. 52(2): 213-227.

[137] Park, J. and J. Moon, Control of colloidal particle deposit patterns within picoliter droplets ejected by ink-jet printing. *Langmuir*,2006. 22(8): 3506-13.

[138] Singh, M., H.M. Haverinen, P. Dhagat, and G.E. Jabbour, Inkjet printing-process and its applications. *Adv Mater*,2010. 22(6): 673-85.

[139] van Dam, D.B. and C. Le Clerc, Experimental study of the impact of an ink-jet printed droplet on a solid substrate. *Physics of Fluids*,2004. 16(9): 3403-3414.

[140] Courbin, L., J.C. Bird, M. Reyssat, and H.A. Stone, Dynamics of wetting: from inertial spreading to viscous imbibition. *J Phys Condens Matter*,2009. 21(46): 464127.

[141] Eddi, A., K.G. Winkels, and J.H. Snoeijer, Short time dynamics of viscous drop spreading. *Physics of Fluids*,2013. 25(1): 013102.

[142] Bird, J.C., S. Mandre, and H.A. Stone, Short-time dynamics of partial wetting. *Phys Rev Lett*,2008. 100(23): 234501.

[143] Biance, A.L., C. Clanet, and D. Quere, First steps in the spreading of a liquid droplet. *Phys Rev E Stat Nonlin Soft Matter Phys*,2004. 69(1 Pt 2): 016301.

[144] Winkels, K.G., J.H. Weijs, A. Eddi, and J.H. Snoeijer, Initial spreading of low-viscosity drops on partially wetting surfaces. *Physical Review E*,2012. 85(5): 055301.

[145] Drelich, J. and D. Chibowska, Spreading kinetics of water drops on self-assembled monolayers of thiols: significance of inertial effects. *Langmuir*,2005. 21(17): 7733-8.

[146] Tanner, L.H., The spreading of silicone oil drops on horizontal surfaces. *Journal of Physics D: Applied Physics*,1979. 12(9): 1473-1484.

[147] Cormier, S.L., J.D. McGraw, T. Salez, E. Raphaël, and K. Dalnoki-Veress, Beyond Tanner's Law: Crossover between Spreading Regimes of a Viscous Droplet on an Identical Film. *Physical Review Letters*,2012. 109(15).

[148] Haley, P.J. and M.J. Miksis, The Effect of the Contact Line on Droplet Spreading. *Journal of Fluid Mechanics*,1991. 223: 57-81.

[149] Carlson, A., G. Bellani, and G. Amberg, Universality in dynamic wetting dominated by contact-line friction. *Phys Rev E Stat Nonlin Soft Matter Phys*,2012. 85(4 Pt 2): 045302.

[150] Hocking, L.M. and A.D. Rivers, The spreading of a drop by capillary action. *Journal of Fluid Mechanics*,2006. 121(-1): 425.

[151] Colosqui, C.E., J.F. Morris, and J. Koplik, Colloidal Adsorption at Fluid Interfaces: Regime Crossover from Fast Relaxation to Physical Aging. *Physical Review Letters*,2013. 111(2).

[152] Kaz, D.M., R. McGorty, M. Mani, M.P. Brenner, and V.N. Manoharan, Physical ageing of the contact line on colloidal particles at liquid interfaces. *Nat Mater*,2012. 11(2): 138-42.

[153] Stalder, A.F., G. Kulik, D. Sage, L. Barbieri, and P. Hoffmann, A snake-based approach to accurate determination of both contact points and contact angles. *Colloids and Surfaces a-Physicochemical and Engineering Aspects*,2006. 286(1-3): 92-103.

[154] Voorhees, P.W., Ostwald Ripening of Two-Phase Mixtures. *Annual Review of Materials Science*,1992. 22(1): 197-215.

[155] Brailsford, A.D. and P. Wynblatt, The dependence of ostwald ripening kinetics on particle volume fraction. *Acta Metallurgica*,1979. 27(3): 489-497.

[156] Marqusee, J.A. and J. Ross, Theory of Ostwald ripening: Competitive growth and its dependence on volume fraction. *The Journal of Chemical Physics*,1984. 80(1): 536.

[157] Bertrand, E., T.D. Blake, and J.D. Coninck, Influence of solid-liquid interactions on dynamic wetting: a molecular dynamics study. *J Phys Condens Matter*,2009. 21(46): 464124.

[158] Brochard-Wyart, F. and P. De Gennes, Dynamics of partial wetting. *Advances in colloid and interface science*,1992. 39: 1-11.

[159] Duvivier, D., T.D. Blake, and J. De Coninck, Toward a predictive theory of wetting dynamics. *Langmuir*,2013. 29(32): 10132-40.

[160] Seveno, D., T.D. Blake, S. Goossens, and J. De Coninck, Predicting the wetting dynamics of a two-liquid system. *Langmuir*,2011. 27(24): 14958-67.

[161] Goossens, S., D. Seveno, R. Rioboo, A. Vaillant, J. Conti, and J. De Coninck, Can we predict the spreading of a two-liquid system from the spreading of the corresponding liquid-air systems? *Langmuir*,2011. 27(16): 9866-72.

[162] Järn, M., F.J. Brieler, M. Kuemmel, D. Grosso, and M. Lindén, Wetting of Heterogeneous Nanopatterned Inorganic Surfaces. *Chemistry of Materials*,2008. 20(4): 1476-1483.

[163] Violi, I.L., M.D. Perez, M.C. Fuertes, and G.J. Soler-Illia, Highly ordered, accessible and nanocrystalline mesoporous TiO(2) thin films on transparent conductive substrates. *ACS Appl Mater Interfaces*,2012. 4(8): 4320-30.

[164] Aussillous, P. and D. Quere, Quick deposition of a fluid on the wall of a tube. *Physics of Fluids*,2000. 12(10): 2367-2371.

[165] Bretherton, F.P., The Motion of Long Bubbles in Tubes. *Journal of Fluid Mechanics*,1961. 10(2): 166-188.

[166] *OpenFOAM: The Open Source CFD Toolbox*. 2014.

[167] Hoang, D.A., V. van Steijn, L.M. Portela, M.T. Kreutzer, and C.R. Kleijn, Benchmark numerical simulations of segmented two-phase flows in microchannels using the Volume of Fluid method. *Computers & Fluids*,2013. 86: 28-36.

[168] Cubaud, T., M. Tatineni, X.L. Zhong, and C.M. Ho, Bubble dispenser in microfluidic devices. *Physical Review E*,2005. 72(3).

[169] Redon, C., F. Brochard-Wyart, and F. Rondelez, Dynamics of dewetting. *Phys Rev Lett*,1991. 66(6): 715-718.

[170] Blackmore, B., D.Q. Li, and J. Gao, Detachment of bubbles in slit microchannels by shearing flow. *Journal of Colloid and Interface Science*,2001. 241(2): 514-520.

[171] Ransohoff, T.C. and C.J. Radke, Laminar flow of a wetting liquid along the corners of a predominantly gas-occupied noncircular pore. *Journal of Colloid and Interface Science*,1988. 121(2): 392-401.

[172] Wong, H., C. Radke, and S. Morris, The motion of long bubbles in polygonal capillaries. Part 1. Thin films. *Journal of Fluid Mechanics*,1995. 292: 71-94.

[173] Wong, H., C.J. Radke, and S. Morris, The motion of long bubbles in polygonal capillaries. Part 2. Drag, fluid pressure and fluid flow. *Journal of Fluid Mechanics*,1995. 292: 95-110.

[174] Fuerstman, M.J., A. Lai, M.E. Thurlow, S.S. Shevkoplyas, H.A. Stone, and G.M. Whitesides, The pressure drop along rectangular microchannels containing bubbles. *Lab on a Chip*,2007. 7(11): 1479-1489.

[175] Ajaev, V.S. and G.M. Homsy, Modeling shapes and dynamics of confined bubbles. *Annual Review of Fluid Mechanics*,2006. 38: 277-307.

[176] Wong, H., *The motion of a long bubble in polygonal capillaries at low capillary numbers*. 1992, University of California, Berkeley.

[177] Baroud, C.N., F. Gallaire, and R. Dangla, Dynamics of microfluidic droplets. *Lab Chip*,2010. 10(16): 2032-45.

[178] Larson, R.G., *The structure and rheology of complex fluids*. 1999: Oxford University Press, New York.

[179] van der Sman, R.G. and M.B. Meinders, Mesoscale models of dispersions stabilized by surfactants and colloids. *Adv Colloid Interface Sci*,2014. 211: 63-76.

[180] Wu, M.M., T. Cubaud, and C.M. Ho, Scaling law in liquid drop coalescence driven by surface tension. *Physics of Fluids*,2004. 16(7): L51-L54.

[181] Eggers, J., Nonlinear dynamics and breakup of free-surface flows. *Reviews of Modern Physics*,1997. 69(3): 865-929.

[182] Rabe, C., J. Malet, and F. Feuillebois, Experimental investigation of water droplet binary collisions and description of outcomes with a symmetric Weber number. *Physics of Fluids*,2010. 22(4): 047101.

[183] Yoon, Y., M. Borrell, C.C. Park, and L.G. Leal, Viscosity ratio effects on the coalescence of two equal-sized drops in a two-dimensional linear flow. *Journal of Fluid Mechanics*,2005. 525: 355-379.

[184] Aarts, D.G.A.L. and H.N.W. Lekkerkerker, Droplet coalescence: drainage, film rupture and neck growth in ultralow interfacial tension systems. *Journal of Fluid Mechanics*,2008. 606.

[185] Jones, A.F. and S.D.R. Wilson, The film drainage problem in droplet coalescence. *Journal of Fluid Mechanics*,2006. 87(02): 263.

[186] Thorsen, T., R.W. Roberts, F.H. Arnold, and S.R. Quake, Dynamic pattern formation in a vesicle-generating microfluidic device. *Phys Rev Lett*,2001. 86(18): 4163-6.

[187] Hashimoto, M., P. Garstecki, H.A. Stone, and G.M. Whitesides, Interfacial instabilities in a microfluidic Hele-Shaw cell. *Soft Matter*,2008. 4(7): 1403-1413.

[188] Cottin, C., H. Bodiguel, and A. Colin, Influence of wetting conditions on drainage in porous media: a microfluidic study. *Phys Rev E Stat Nonlin Soft Matter Phys*,2011. 84(2 Pt 2): 026311.

[189] Schultz, K.M. and E.M. Furst, High-throughput rheology in a microfluidic device. *Lab Chip*,2011. 11(22): 3802-9.

[190] Gu, H., M.H. Duits, and F. Mugele, Droplets formation and merging in two-phase flow microfluidics. *Int J Mol Sci*,2011. 12(4): 2572-97.

[191] Bhattacharjee, B. and S.A. Vanapalli, Electrocoalescence based serial dilution of microfluidic droplets. *Biomicrofluidics*,2014. 8(4): 044111.

[192] Anna, S.L., N. Bontoux, and H.A. Stone, Formation of dispersions using "flow focusing" in microchannels. *Applied Physics Letters*,2003. 82(3): 364-366.

[193] Link, D.R., S.L. Anna, D.A. Weitz, and H.A. Stone, Geometrically mediated breakup of drops in microfluidic devices. *Phys Rev Lett*,2004. 92(5): 054503.

[194] Bremond, N., A.R. Thiam, and J. Bibette, Decompressing emulsion droplets favors coalescence. *Phys Rev Lett*,2008. 100(2): 024501.

[195] Cubaud, T., Deformation and breakup of high-viscosity droplets with symmetric microfluidic cross flows. *Phys Rev E Stat Nonlin Soft Matter Phys*,2009. 80(2 Pt 2): 026307.

[196] Schneider, T.M., S. Mandre, and M.P. Brenner, Algorithm for a Microfluidic Assembly Line. *Physical Review Letters*,2011. 106(9): -.

[197] Colosqui, C.E., J.F. Morris, and H.A. Stone, Hydrodynamically Driven Colloidal Assembly in Dip Coating. *Physical Review Letters*,2013. 110(18).

[198] Hatch, A.C., J.S. Fisher, S.L. Pentoney, D.L. Yang, and A.P. Lee, Tunable 3D droplet self-assembly for ultra-high-density digital micro-reactor arrays. *Lab Chip*,2011. 11(15): 2509-17.

[199] Bear, J., *Dynamics of Fluids in Porous Media*. Dover Civil and Mechanical Engineering. 2013: Courier Dover Publications.

[200] Cubaud, T. and T.G. Mason, Capillary threads and viscous droplets in square microchannels. *Physics of Fluids*,2008. 20(5): 053302.

[201] Jose, B.M. and T. Cubaud. *Droplet assembly in a microfluidic chamber*. 2012; This experimental movie shows the formation and evolution of crystal-like structures made of droplets in a microfluidic chamber. Available from: http://www.youtube.com/watch?v=lnVB9MauOrU.

[202] Darvishi, S. and T. Cubaud, Lubrication of Highly Viscous Core-Annular Flows in Microfluidic Chambers. *Journal of Fluids Engineering-Transactions of the Asme*,2011. 133(3).

[203] Chabert, M. and J.L. Viovy, Microfluidic high-throughput encapsulation and hydrodynamic self-sorting of single cells. *Proc Natl Acad Sci U S A*,2008. 105(9): 3191-6.

[204] Cubaud, T. and T.G. Mason, Folding of viscous threads in diverging microchannels. *Physical Review Letters*,2006. 96(11): 114501.

[205] Lai, A., N. Bremond, and H.A. Stone, Separation-driven coalescence of droplets: an analytical criterion for the approach to contact. *Journal of Fluid Mechanics*,2009. 632: 97-107.

[206] Shemesh, J., A. Nir, A. Bransky, and S. Levenberg, Coalescence-assisted generation of single nanoliter droplets with predefined composition. *Lab Chip*,2011. 11(19): 3225-30.

[207] Danny Raj, M. and R. Rengaswamy, Understanding drop-pattern formation in 2-D microchannels: a multi-agent approach. *Microfluidics and Nanofluidics*,2014. 10.1007/s10404-014-1336-8.

[208] Jose, B.M. and T. Cubaud, Droplet arrangement and coalescence in diverging/converging microchannels. *Microfluidics and Nanofluidics*,2011. 12(5): 687-696.

[209] Rashidnia, N., R. Balasubramaniam, and D. Delsignore, Interfacial-Tension Measurement of Immiscible Liquids Using a Capillary-Tube. *Aiche Journal*,1992. 38(4): 615-618.

APPENDIX A: Extraction of spatiotemporal diagrams.

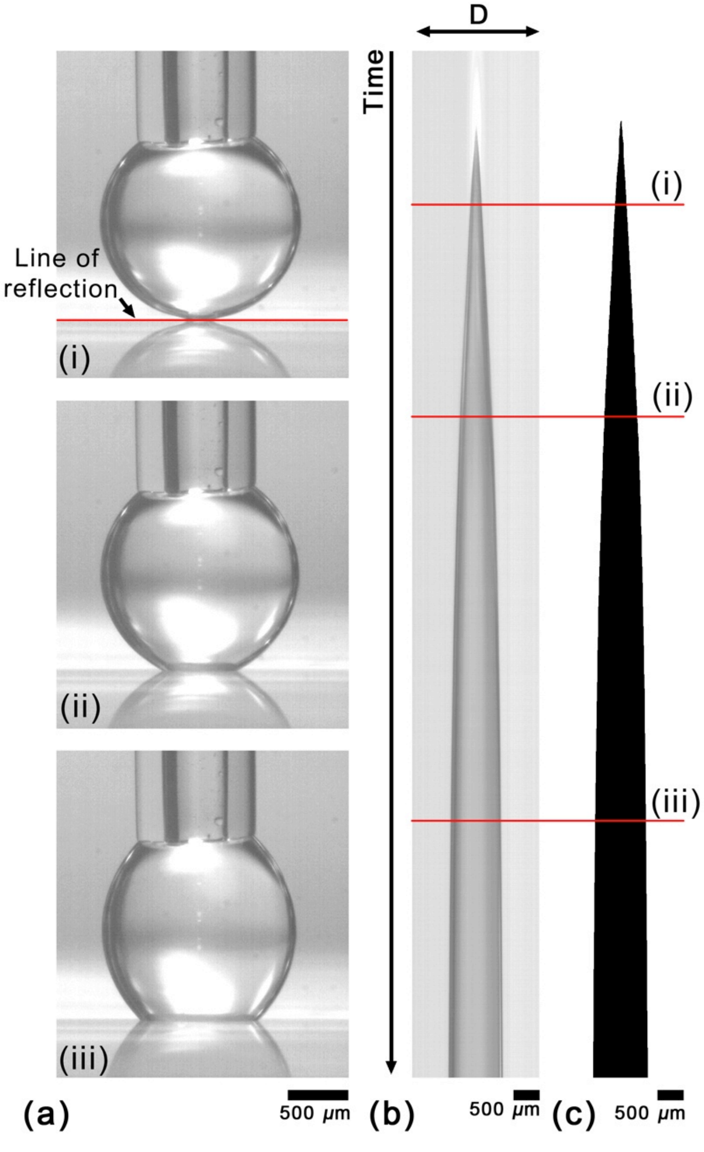

Figure A-1 Spatiotemporal diagram. (a) (*i-iii*) Experimental micrographs: Time series of droplet spreading. (b) Time-space diagram is extracted from the video (b) before processing and (c) after processing. Red line corresponds to the images in (a).

We locate the solid surface along the line of reflection. After defining a line of one-pixel width along the line of reflection, all the events which take place along this line is summarized using spatiotemporal or time-space diagram. Time space diagram in Figure A-1(b) depicts the temporal evolution of the wetting diameter. The dark grey shading in Figure A-1(b) shows the growth of the spreading diameter in time. After applying threshold, a binary image is generated [Figure A-1(b)] and used to calculate the spreading diameter as a function of time [Figure A-2].

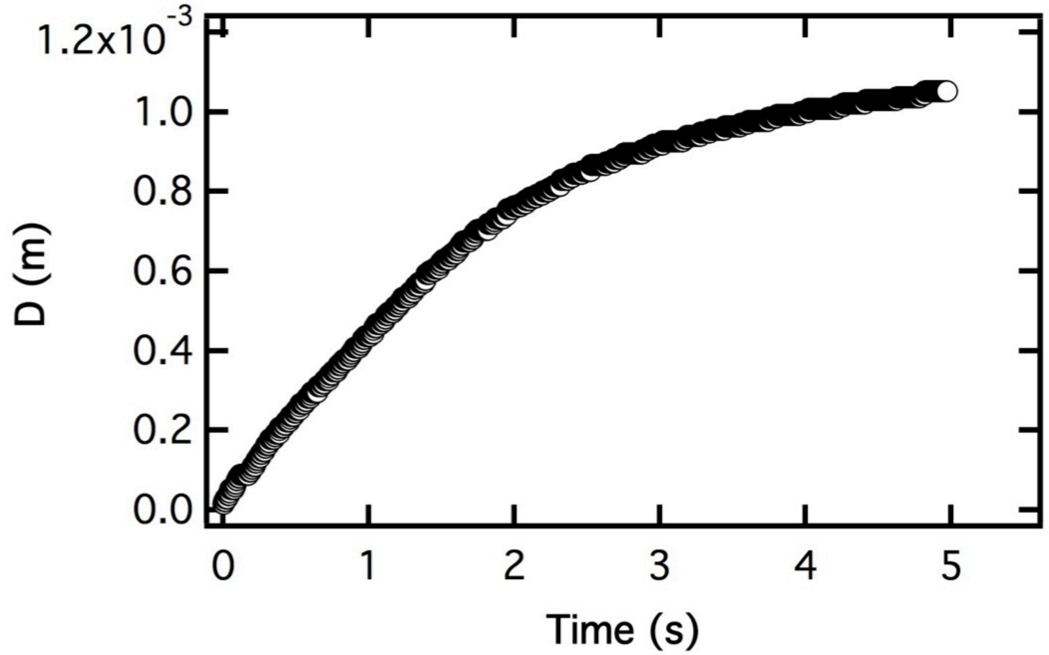

Figure A-2 Spreading diameter vs. time graph extracted from the spatiotemporal diagram

APPENDIX B: Measurement of interfacial tension

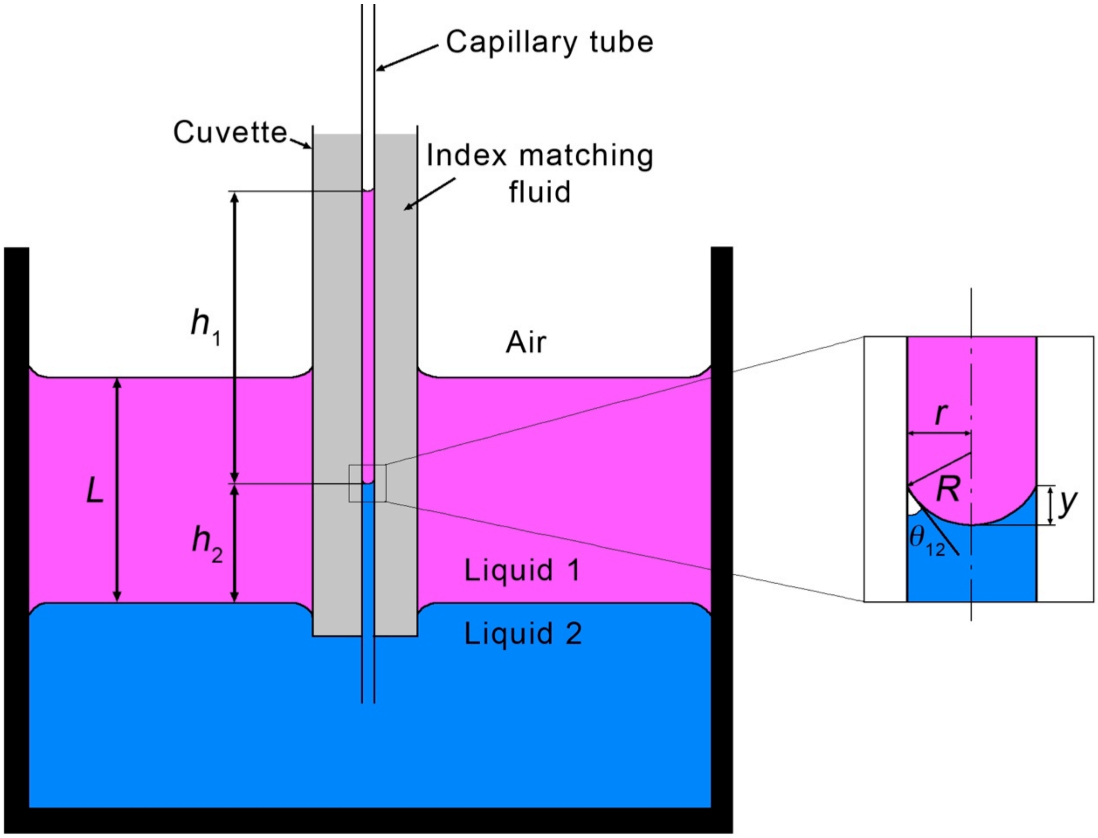

Figure B-1 Schematic of the double capillary rise method with index matching fluid to visualize the meniscus. Inset: Magnified view of meniscus.

The interfacial tension between the two immiscible fluids is measured using the double capillary rise method proposed by Rashidnia *et al*. [209]. Their experimental setup is slightly modified by the use of an index matching fluid around the capillary. The refractive index of the glass capillary and the fluid in the cuvette is matched (glycerol is used as the index matching liquid) to avoid reflection inside the capillary walls and accurately visualize the capillary meniscus. Initially, the capillary tube attached to the cuvette is plunged into liquid 1 drawing Liquid 1 into the capillary. The capillary is pushed down further to penetrate the Liquid 2 drawing Liquid 2 into the capillary. Inside the capillary, the Liquid 1– Liquid 2 interface forms a curved meniscus with a contact angle of θ_{12} on the capillary wall. Assuming the meniscus to be spherical, the following equation for interfacial tension is obtained [209],

$$\gamma_{12} = -\gamma_{1a}\frac{Cos\,\theta_{1a}}{Cos\,\theta_{12}} + \frac{gr}{2Cos\,\theta_{12}}\left(\rho_1 h_1 + \rho_2 h_2 - \rho_1 L\right) \qquad \text{(B-1)}$$

where γ_{12} – interfacial tension between Liquid 1 and Liquid 2, γ_{1a} – surface tension of Liquid 1, θ_{1a} – Contact angle at Air-Liquid 1 interface, θ_{12} – Contact angle at Liquid 1-Liquid 2 interface, g – acceleration due to gravity, ρ_1 – density of Liquid 1 and ρ_2 – density of Liquid 2. Other variables such as h_1, h_2, and L are denoted in the Figure (B-1). Both h_1 and h_2 are measured from the bottom of the meniscus. In all our systems, Liquid 1 (oil) totally wets the capillary with $\theta_{1a} \approx 0$ and the equation (B-1) can be reduced to,

$$\gamma_{12} = -\gamma_{1a}\frac{R}{r} + \frac{gR}{2}\left(\rho_1 h_1 + \rho_2 h_2 - \rho_1 L\right) \qquad \text{(B-2)}$$

where r is the radius of the capillary tube and R is the radius of curvature of the meniscus. The radius of curvature R is calculated as [209],

$$R = \frac{y^2 + r^2}{2y} \qquad \text{(B-3)}$$

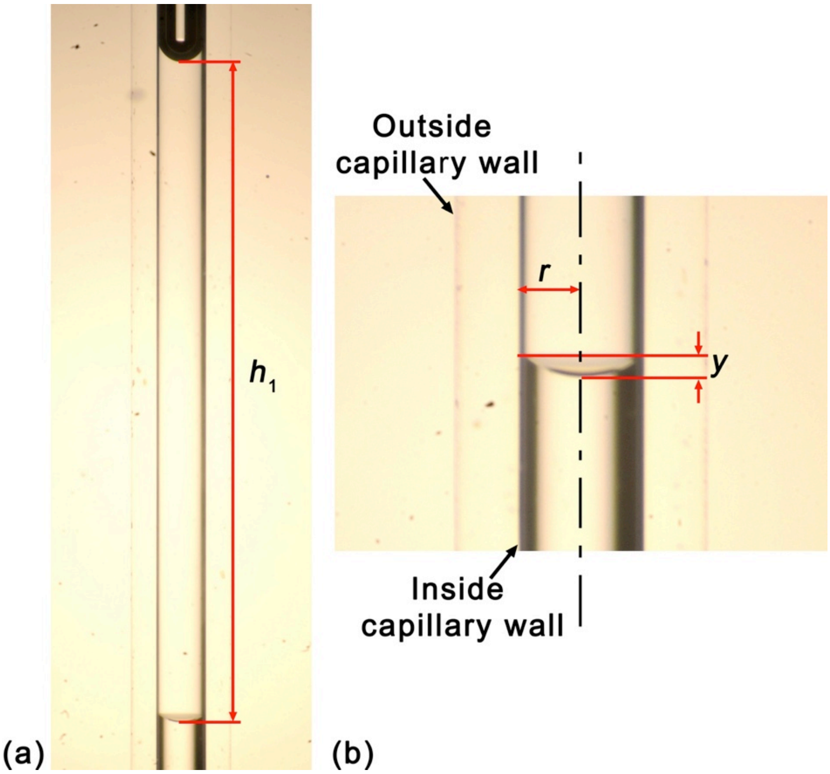

Figure B-2 Experimental micrographs showing the measurement of the curvature and the height h_1.

The interfacial tension values for water with PDMS oils plateaus as the viscosity of the oil increases above10cS and can be fitted using an exponential curve of the form $\gamma = \gamma_0 + Ae^{\upsilon^{2}/\tau}$. All the values for the parameters are reported in Table B-1.

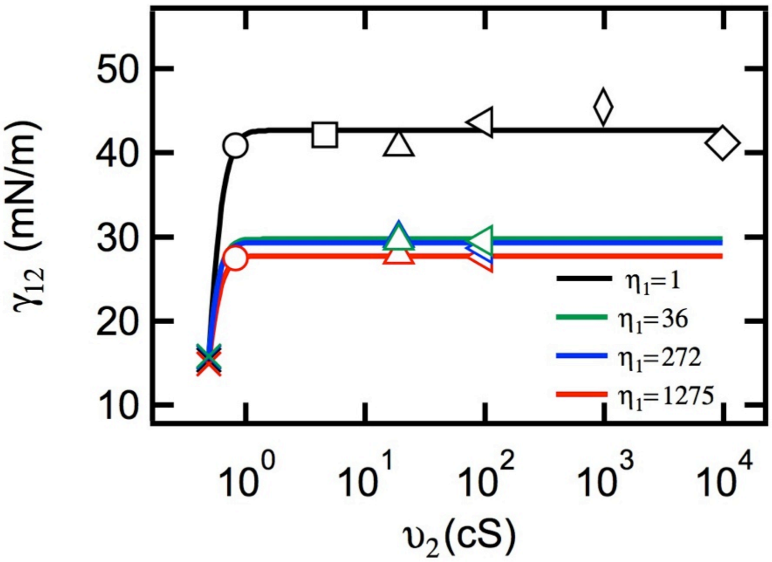

Figure B-3 Values of interfacial tension for water and water glycerol mixtures with PDMS oils of varying viscosities. Solid Line: $\gamma_{12} = \gamma_0 + Ae^{\upsilon^{2}/\tau}$ with the fit parameters given in Table B-1.

η_1 (cP)	Color	γ_0	A	τ
1	Black (Water)	42.7	-1323	7.9
36	Green (G80)	29.7	-2344	10.5
272	Blue (G92)	29.3	-3227	11.2
1275	Red (G99)	27.7	-1379	9.5

Table B-1 Fitting parameters for the curves in Figure B-3.